INTERACTION BETWEEN THE ATMOSPHERIC BOUNDARY LAYER AND WIND ENERGY: FROM CONTINENTAL-SCALE TO TURBINE-SCALE

by

CLARA MAE ST. MARTIN

B.S., the Pennsylvania State University, 2012

M.S., University of Colorado, 2015

A thesis submitted to the

Faculty of the Graduate School of the

University of Colorado in partial fulfillment

of the requirement for the degree of

Doctor of Philosophy

Department of Atmospheric and Oceanic Sciences

2017

This thesis entitled:
Interaction between the atmospheric boundary layer and wind energy:
from continental-scale to turbine-scale
written by Clara Mae St. Martin
has been approved for the Department of Atmospheric and Oceanic Sciences

_____

Prof. Julie Lundquist

_____

Prof. Jeffrey Weiss

Date_____

The final copy of this thesis has been examined by the signatories, and we find that both the content and the form meet acceptable presentation standards of scholarly work in the above mentioned discipline.

St. Martin, Clara Mae (PhD., Atmospheric and Oceanic Sciences)
Interaction between the atmospheric boundary layer and wind energy:
from continental-scale to turbine-scale
Thesis directed by Associate Professor Julie K. Lundquist

Abstract

Wind turbines and groups of wind turbines, or "wind plants", interact with the complex and heterogeneous boundary layer of the atmosphere. We define the boundary layer as the portion of the atmosphere directly influenced by the surface, and this layer exhibits variability on a range of temporal and spatial scales. While early developments in wind energy could ignore some of this variability, recent work demonstrates that improved understanding of atmosphere-turbine interactions leads to the discovery of new ways to approach turbine technology development as well as processes such as performance validation and turbine operations. This interaction with the atmosphere occurs at several spatial and temporal scales from continental-scale to turbine-scale. Understanding atmospheric variability over continental-scales and across plants can facilitate reliance on wind energy as a baseload energy source on the electrical grid. On turbine scales, understanding the atmosphere's contribution to the variability in power production can improve the accuracy of power production estimates as we continue to implement more wind energy onto the grid. Wind speed and directional variability within a plant will affect wind turbine wakes within the plants and among neighboring plants, and a deeper knowledge of these variations can help mitigate effects of wakes and possibly even allow the manipulation of these wakes for increased production. Herein, I present the extent of my PhD work, in which I studied outstanding questions at these scales at the intersections of wind energy and atmospheric science.

My work consists of four distinct projects. At the coarsest scales, I analyze the separation between wind plant sites needed for statistical independence in order to reduce variability for grid-integration of wind. Site data from three datasets spanning continents, durations and time resolution include 45 years of hourly wind speed data from over 100 sites in Canada, 4 years of five-minute wind speed data from 14 sites in the US Pacific Northwest, and one year of five-minute wind power generation data from 29 wind farms in southeastern Australia. I find similarities between these datasets in which correlations that fall to zero with increasing station separation distance, and the higher the high-pass cut-off frequency, the smaller the station separation required to achieve de-correlation. Shifting to atmospheric interaction on turbine-scales, I use 2.5 months of upwind tower and turbine data to understand how power production varies with different atmospheric stability and turbulence regimes. At lower wind speeds, periods of unstable and more turbulent conditions produce more power than periods of stable and less turbulent conditions, while at wind speeds closer to rated wind speed, periods of unstable and more turbulent conditions produce less power than periods of stable and less turbulent conditions. Using these new, stability- and turbulence-specific power curves to calculate annual energy production (AEP) estimates results in smaller AEPs than if calculated using no stability and turbulence filters, which could have implications for manufacturers and operators. In my third project, I address the problem of expensive power production validation. Rather than erecting towers to provide upwind wind measurements, I explore the utility of using nacelle-mounted anemometers for power curve verification studies. I calculate empirical nacelle transfer functions (NTFs) with upwind tower and turbine measurements. The fifth-order and second-order NTFs show a linear relationship between upwind wind speed and nacelle wind speed at wind speeds less than about 9 m s^{-1}, but this relationship becomes non-linear at wind speeds

higher than about 9 m s^{-1}. The use of NTFs results in AEPs within 1 % of an AEP using upwind wind speeds. Additionally, during periods of unstable conditions as well as during more turbulent conditions, the nacelle-mounted anemometer underestimates the upwind wind speed more than during periods of stable conditions and less turbulence conditions at some wind speed bins below rated speed. Finally, in my fourth project, I consider spatial scales on the order of a wind plant. Using power production data from over 300 turbines from four neighboring wind farms in the western US along with simulations using the Weather Research and Forecasting model's Wind Farm Parameterization (WRF-WFP), I investigate the advantage of using the WFP to simulate wakes. The case simulated in this study focuses on the nighttime stable hours during the early morning of 30 October 2011 into the daytime unstable hours of 30 October 2011. During this case, winds from the west and north-northwest range from about 5 to 11 m s^{-1}. A down-ramp occurs in this case study, which WRF predicts too early. The early prediction of the down-ramp likely affects the error in WRF-predicted power, the results of which show exaggerated wake effects. Variable differences in hub-height winds, surface winds, and surface temperature throughout the innermost domain are revealed, and likely caused by some instability upwind of the farms in the simulations or due to horizontal resolution as suggested by Rai et al. (2017).

While these projects span a range of spatio-temporal scales, a unifying theme is the important aspect of atmospheric variation on wind power production, wind power production estimates, and means for facilitating the integration of wind-generated electricity into power grids. Future work, such as universal NTFs for sites with similar characteristics, NTFs for waked turbines, or the deployment of lidars on turbine nacelles for operation purposes, should continue to study the mutually-important interconnections between these two fields.

ACKNOWLEDGEMENTS

Overall, grad school was a great experience in which I learned a lot. I would first like to thank m y undergraduate advisors at Penn State, Ken Davis and Susan Stewart, who indulged my request to somehow merge my interests of meteorology and wind energy. I also want to thank my graduate advisor, Julie Lundquist, for providing the right amount of guidance while also allowing me to be independent. My first year of graduate school was a steep learning curve and Mike Rhodes, Matt Aitken and Brian Vanderwende gave me guidance on improving my coding and data analysis skills. I would like to thank my research committee and co-authors, for their input and direction, and for taking the time for the many emails and drafts of papers I sent them along the way. I also want to thank Laurie Conway, for all the amazing work she does for ATOC.

I want to thank my family, for bearing with me as I moved halfway across the country for my career. My Aunt Fran provided me a home in Colorado and weekend get-aways when I needed them. I am glad I was fortunate enough to spend those last few years with you.

Finally, I would like to thank my roommates, Chris Maloney, Torie Hartwick and Josh Pettit, for their friendship. I appreciate you letting me bounce ideas off you and for teaching me about high-altitude clouds, high-energy electrons, and dust storms on Mars. Movie nights and those late night talks (often sitting on the floor in the kitchen) got me through grad school.

CONTENTS

TABLES

FIGURES

CHAPTER I

INTRODUCTION

The fight to mitigate the effects of climate change is a major driver of the clean energy industry at home and abroad. In December of 2015, representatives from countries around the world came together in Paris, France to come to a monumental, global agreement called the Paris Agreement. Now international law, this agreement has been made between 97 parties so far, including the worlds' top energy consumers: China, the US, Canada, Mexico, and Brazil, among many others. Besides the geopolitical accomplishment of so many countries agreeing on a way forward, a major outcome of this meeting was the agreement to work to reduce global greenhouse gas (GHG) emissions. The parties agreed to keep the global increase in mean temperature from pre-industrial levels below 2 °C, with the aim of keeping the mean temperature increase below 1.5 °C (United Nations, 2015).

According to the International Energy Agency (IEA), countries in the Organization for Economic Co-operation and Development (OCED) are already making progress to reach this goal: consumption of renewable and low-carbon fuels such as nuclear for electricity generation is increasing while consumption of combustible fuels for electricity generation is decreasing (Fig 1). Comparisons between 2015 and 2016 electricity production in by energy sector for the months of January through July reveal that the percentage of combustible fuels used for electricity decreased by about 1.6 %, while the percentage of nuclear, hydro, and other renewable fuel used for electricity increased 0.2 %, 0.7 %, and 0.9 %, respectively (Fig. 1, IEA Statistics, 2016).

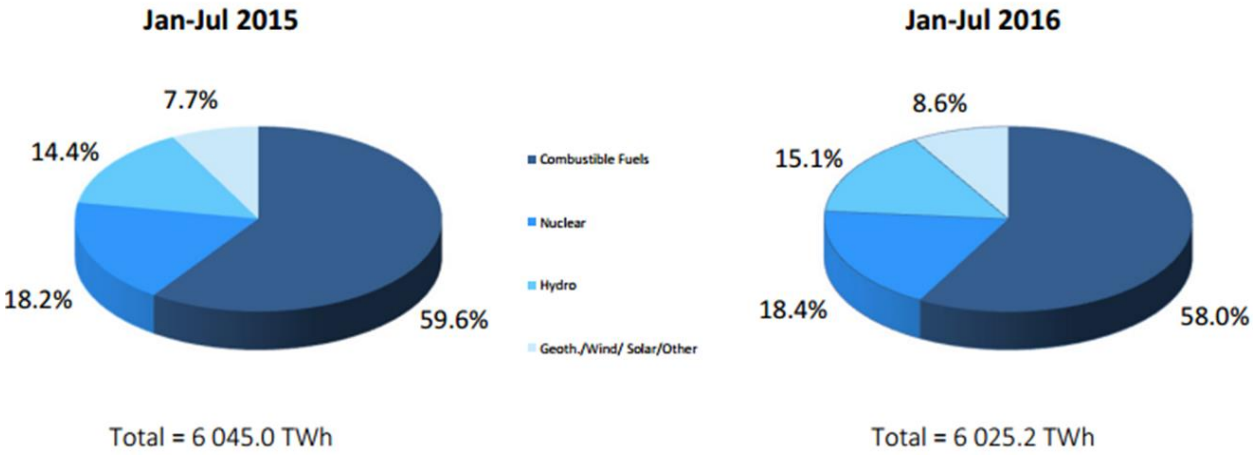

Figure 1. Electricity production by fuel type for countries in the OECD. Source: IEA (http://www.iea.org/media/statistics/surveys/electricity/mes.pdf).

"Clean" energy sources

As countries around the world strategize how to design their energy portfolios while also reducing GHG emissions, it is important to define what constitutes a "clean" fuel. We know that nuclear, geothermal, hydro, solar, and wind all result in zero direct emissions of GHGs, while the burning of coal and natural gas do emit GHGs. Natural gas emissions are, however, lower than emissions from coal: according to the Intergovernmental Panel on Climate Change (IPCC) Working Group III, the maximum direct emissions of coal for electricity production is 870 g CO2-eq/kWh while the maximum direct emissions of combined cycle gas for electricity production is 490 g CO2-eq/kWh (IPCC, 2014).

However, direct emissions are only a portion of the emissions from the entire lifecycle of an energy technology. The lifecycle of an energy technology includes any direct emissions, infrastructure and supply chain emissions, biogenic CO2 emissions and albedo effect, and methane emissions (IPCC, 2014). Even a "clean" fuel such as wind still results in some

emissions over its lifecycle. Median emissions from coal and natural gas for electricity production over their lifecycles are 820 g CO2-eq/kWh and 490 g CO2-eq/kWh, respectively (IPCC, 2014). Nuclear power emits a median of only 12 g CO2-eq/kWh (IPCC, 2014), but the US does not currently have an effective way of dealing with the increasing amount of nuclear waste. As a number of modern-technology nuclear plants come online in the next few years (U.S. NRC, 2016), developing safe and practical nuclear waste repositories as well as implementing policies for nuclear reprocessing will be crucial. Median emissions from hydro, solar PV and onshore wind are 24 g CO2-eq/kWh, 48 g CO2-eq/kWh, and 11 g CO2-eq/kWh, respectively (IPCC, 2014). Wind and nuclear are the "cleanest" technologies with regard to median lifecycle emissions of CO2, quickly followed by hydro and solar, with coal and natural gas emitting significantly more GHG than all other sources. According to a press release from the American Wind Energy Association (AWEA), the US wind industry reduced power sector emissions by 4.4 % in 2013. Wind generation avoids approximately 0.6 metric tons of CO2 per MWh (AWEA, 2014).

Current and projected energy market in the US

Wind energy is a clean energy, but reducing GHG through increased integration of wind does not necessarily mean increasing the market share of wind technology is easy and can happen overnight. US energy infrastructure includes multiple energy sources and technologies. However, we are making progress towards phasing out fossil fuels and implementing more clean energy technology. According to the US Energy Information Administration (EIA), while overall total energy production has increased by about 23.65 % in the US over the last 15 years, energy production from coal has decreased about 21.04 % while energy production from oil, natural gas, and renewables has increased about 59.31 %, 42.72 %, and 57.23 %, respectively (Fig. 2, EIA,

2016). Oil and natural gas markets have been notoriously volatile in recent years, reacting to global overproduction as well as various geopolitical issues. However, oil and natural gas reserves as of 2014 in the US almost certainly ensure the use of these sources for consumption, as proven oil reserves in the US have reached 39 billion barrels and proven natural gas reserves have reached 388 trillion cubic feet (EIA, 2015). Abundant reserves of natural gas in the US combined with the lower emissions from natural gas compared to coal has led to replacing coal plants with combined-cycle natural gas plants. Increased development of combined-cycle plants has contributed to the decrease in energy production from coal over the past 15 years. As seen in Fig. 2 below, total energy production from renewables has increased over the last 15 years. Since the US has reached the limit for hydro plant development and is more focused on refurbishing current hydro plants (NHA, 2016), much of this increase in renewables has come from wind and solar. Wind energy's share of the US electricity market has increased from less than 0.5 % in 2001 to 2.3 % in 2010 to 4.7 % in 2015, and projected to be near 5.6 % in 2016 (EIA, 2016).

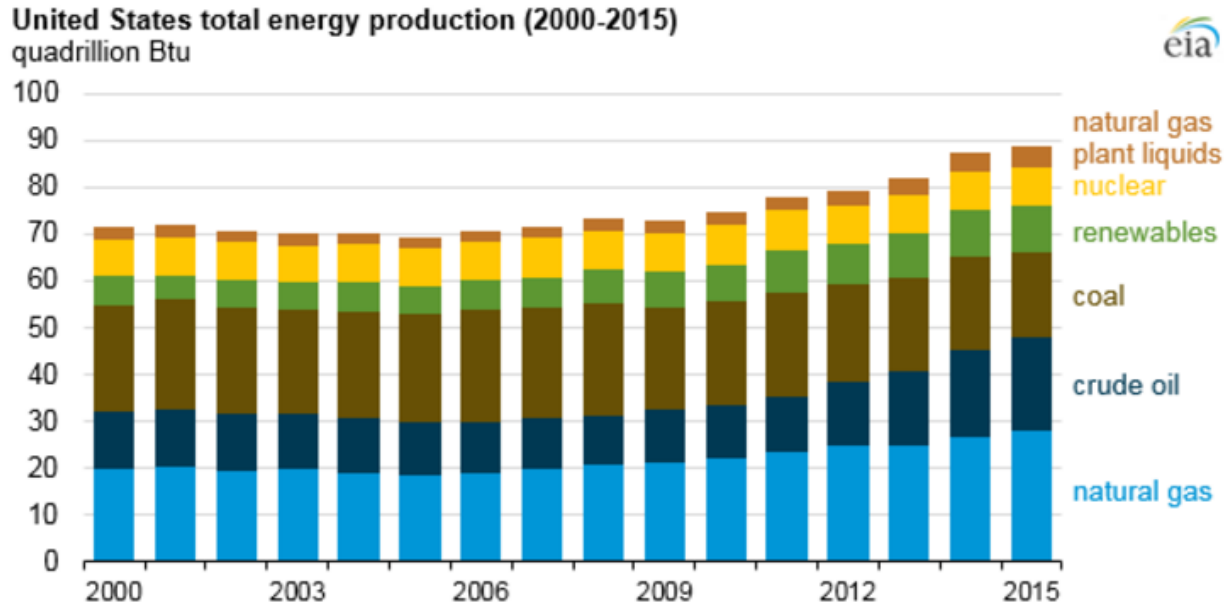

Figure 2. Total energy production in the US from 2000 to 2015. Source: EIA (https://www.eia.gov/todayinenergy/detail.php?id=25852).

In the US, policy drives energy technology in the electricity market, usually in the form of subsidies. However, more aggressive policy approaches are under consideration, including a possible carbon tax as well as the US Environmental Protection Agency's (EPA) Clean Power Plan (CPP). The CPP is a list of standards for states to reduce carbon pollution from power plants and is pending review by the US Supreme Court. According to the EIA in their Annual Energy Outlook report from 2016 (EIA, 2016), the CPP has the potential to increase the growth of renewable energy and natural gas generation while lowering that of coal (Fig. 3).

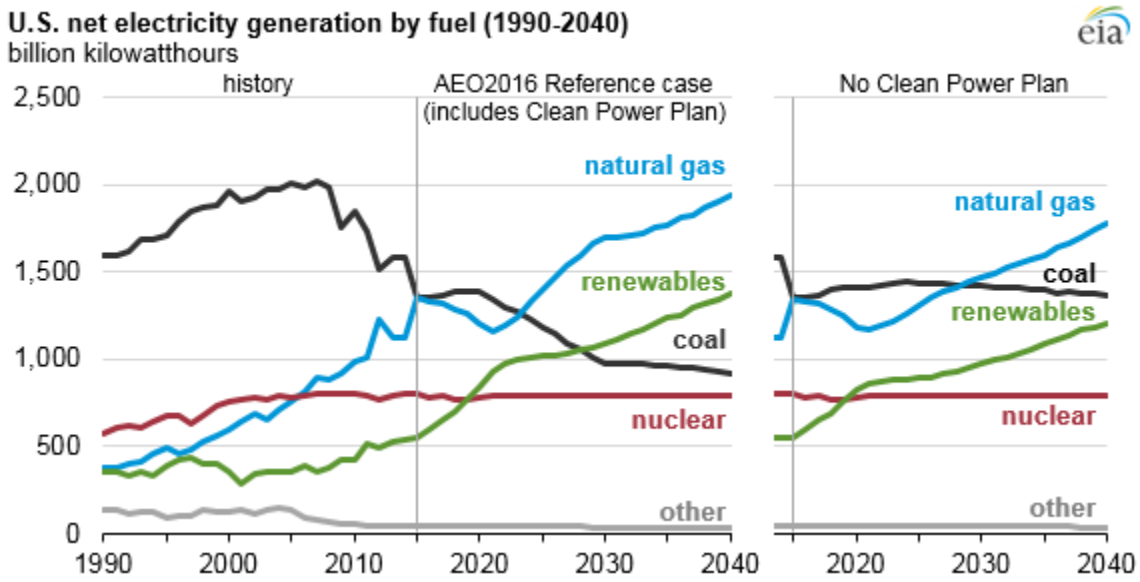

Figure 3. Net electricity generation by fuel in the US with and without the CPP. Source: EIA (http://www.eia.gov/forecasts/aeo/er/pdf/0383er(2016).pdf).

Wind energy sector

Global awareness of the impact of climate change has driven policy which has allowed for the development of a viable clean energy sector, in which global investments reached 329 billion USD in 2015 (GWEC, 2016). As part of this clean energy portfolio, wind energy is a

small but significant player in the world electricity market, supplying 3.7 % of the world's electricity with 433 GW of globally installed generation (GWEC, 2016).

Wind energy is widely considered a mature technology. Investors often determine opportunities by the maturity of a technology as defined by the Gartner Hype Cycle. Wind energy technology is entering the plateau on the Hype Cycle for emerging energy technologies, meaning wind energy is a mainstream and viable technology (Gartner, 2014). However, the wind industry is young compared to its fossil-fuel competitors, which means this industry has the opportunity to develop in a way to ensure longevity. The wind energy community is working to improve upon many aspects of the industry, making wind energy more efficient, with the goal of making wind the most cost-effective and therefore cost-competitive energy source. As of November 2015, the unsubsidized levelized cost of energy of onshore wind was as low as $32/MWh, which is lower than that for coal and gas combined cycle, which were as low as $65/MWh and $52/MWh, respectively (Lazard, 2015).

The fuel source for wind energy, wind, is an atmospheric resource that can be harvested without cost. Wind is also the primary source of the forces that affect the day-to-day operation of wind turbine machines, and the efficiency and competitiveness of the electricity that is generated. Thus, one of the areas of "low-hanging fruit" in the wind industry is the potential to improve our understanding of the relationship and interaction between the atmosphere and the wind turbine itself. This important relationship not only forms the foundation of this energy source as these machines capture energy from the atmosphere, but further understanding of the complications of the interaction between wind energy and the atmosphere also can improve a number of aspects of the industry itself. These aspects include research and development (R&D) of refurbished and prototype turbines, resource assessment and turbine siting, better use of

energy storage, turbine operation and performance, wind turbine and plant wakes, and wind farm grid integration.

Motivation

According to the EIA, the average US residence consumes almost 11 MWh/year of electricity (EIA, 2016). More than 48,000 utility-scale wind turbines installed in the US are currently powering an equivalent of about 20 million American homes (AWEA, 2016). With thousands of commercial-scale turbines installed in the US, manufacturers seek ways to make wind turbines more cost-effective. Wind speed increases with height in the troposphere and wind energy capture increases with blade length. As a consequence, wind turbines are growing, with taller towers and longer blades. Currently, utility-scale wind turbines have hub-heights of 80 to 100 m or higher, with the upper tip of the blades reaching upwards of 120 to 180 m in the atmosphere, and capacities of 2 to 3 MW or greater. Offshore turbines are typically larger than onshore turbines due to a stronger and more consistent resource combined with economies of scale offsetting the larger cost of energy offshore. The largest operating offshore wind turbine in the world is a Vestas 8 MW turbine with a rotor diameter of 164 m and a hub height of approximately 105 m. Figure 4 illustrates the increase in turbine hub heights and rotor diameter since the 1980s through today and projects them further into the 21st century.

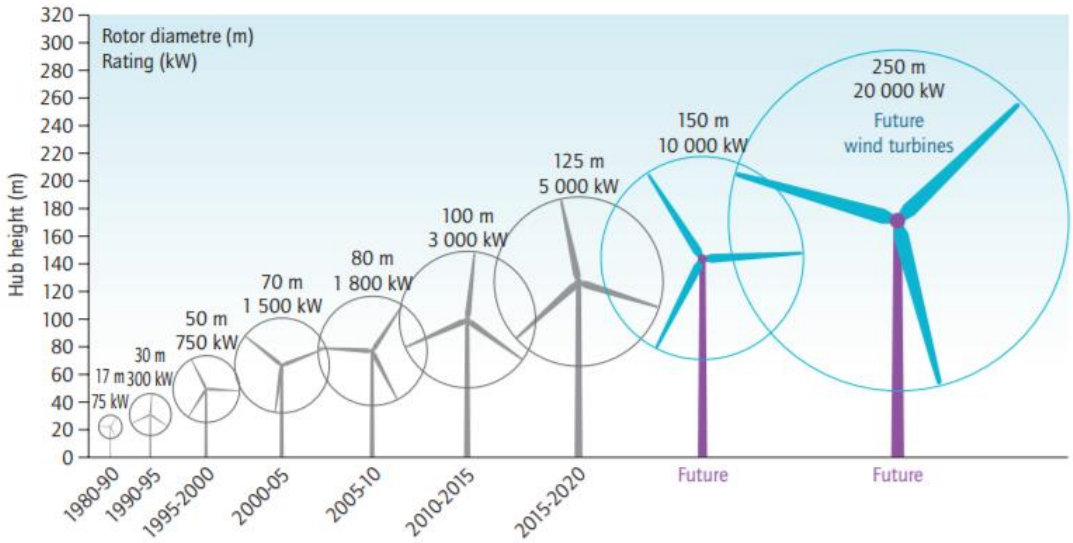

Figure 4. Evolution of wind turbine size over time. Source: IEA (https://www.iea.org/publications/freepublications/publication/Wind_2013_Roadmap.pdf).

With larger turbine capacity and size comes more cost, turbine operational exposure to different meteorological phenomena higher in the atmosphere, and risk, per machine. To lower the risk involved in deploying and operating these expensive machines, research is required to understand the interaction between these large machines and the atmospheric winds that fuel them.

Background

Earth's surface directly influences the lowest layer of the atmosphere which has been defined as the atmospheric boundary layer (ABL) (Stull, 1988). The height of the ABL varies depending on location and time of day (Fig. 5). The surface layer, typically defined as the lower 10% of the ABL, is often referred to as the constant flux layer because variation of vertical turbulent fluxes are small and the mechanical generation of turbulence through shear exceeds the

buoyant generation of turbulence. It is in this layer that Monin-Obukhov similarity theory holds, and the log law can describe the wind profile.

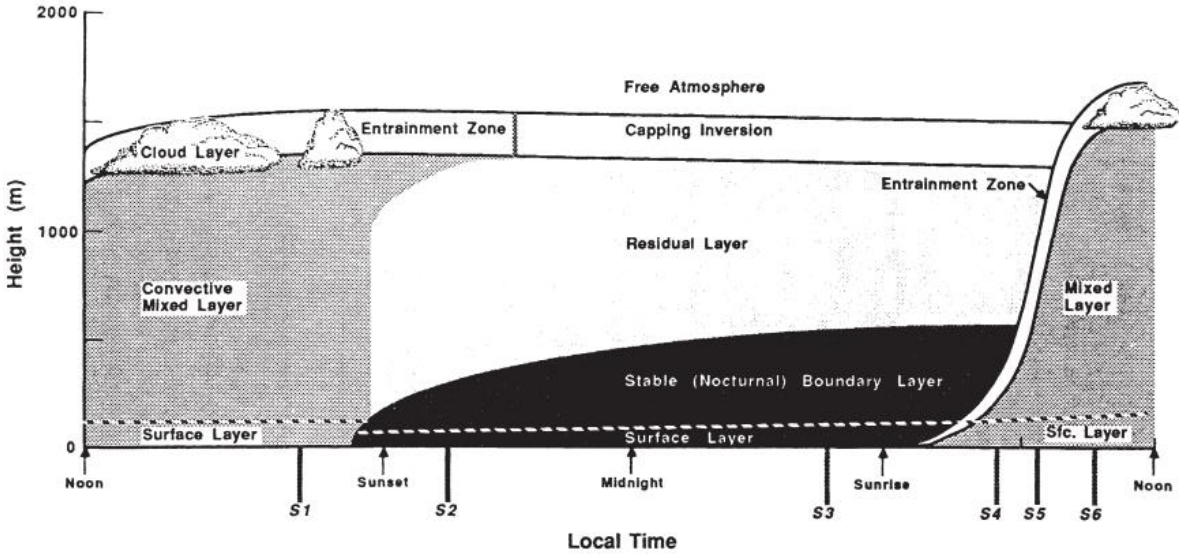

Figure 5. The boundary layer over time. Figure from Stull (1988).

As the surface layer typically reaches heights in the ABL on the order of 10s of meters, wind turbines have only previously stayed within this layer. However, turbine rotors now span up to about 190 m, interacting with more layers in the ABL. Turbine upper tips now breach the surface layer and reach into the convective mixed layer during the day and the stable boundary layer during the night. In layers of the ABL above the surface layer, manufacturers and operators encounter phenomena they did not anticipate, such as nocturnal low-level jets in the plains of the US or wind profiles not fitting the typical log-law profile of the surface layer. These phenomena can lower production as well as the lifetime of the turbine, both of which present a problem to the industry (Kelley et al., 2006). Further understanding of the physical characteristics of these higher layers in the ABL and how they interact with wind turbines will be imperative as these turbines continue to evolve and the industry continues to grow.

Scope

The scope of this dissertation spans from continental-scale variability down to the complexity of the flow around an individual turbine. I investigate atmospheric variability at each of these different scales, providing insight into a range of turbine-atmosphere interactions. Chapter II focuses on wind variability and how it might affect the electrical grid; we demonstrate how aggregating wind farms can mitigate this variability to enable wind to provide reliable baseload power. Chapter III focuses on individual turbines and their power production. We explore how power production varies with atmospheric conditions such as atmospheric stability and turbulence. Seeking to understand how wind power production can be optimized using instrumentation already available on wind turbines, Chapter IV focuses on how atmospheric stability and turbulence contributes to the variability in wind turbine nacelle transfer functions. These transfer functions allow the use of nacelle-mounted instruments in place of expensive towers or remote sensing instruments for power performance testing. Finally, Chapter V moves out in scale to consider aggregations of turbines into large wind farms. We test a mesoscale model parameterization of wind turbine and wind farm wakes during both stable and unstable conditions, with the goal of assessing how atmospheric variability affects these wakes. These wakes affect wind farm siting and wind power forecasting. Chapter VI summarizes my conclusions regarding the importance of rigorous assessment of atmospheric-turbine interactions for reducing the cost of energy and ultimately increasing the development of wind energy around the world.

Layout

This dissertation outlines the research I completed for my PhD work. Each of the following chapters before the conclusion contains published, submitted, or work in progress.

The first is a paper published in *Environmental Research Letters* (http://iopscience.iop.org/article/10.1088/1748-9326/10/4/044004). The second is published in *Wind Energy Science* (http://www.wind-energ-sci.net/1/221/2016/). The third is in review in *Wind Energy Science* (http://www.wind-energ-sci-discuss.net/wes-2016-45/). The fourth is in preparation for submission to *Monthly Weather Review*. Though each of these papers address some aspect of wind energy meteorology, each of these chapters is autonomous and therefore each follows the structure of a peer-reviewed paper including an abstract, conclusion, and acknowledgments. However, I list all references at the end of this document. Two of these publications have supplementary information presented in an Appendix at the end of this document.

CHAPTER II

WIND VARIABILITY AND INTERCONNECTING PLANTS

Wind is a variable energy source. The integration of wind-powered electricity into the electrical grid is complicated by variability in the wind resource. These challenges increase as wind penetration increases. However, variability can be reduced by interconnecting geographically diverse wind farms, provided the generators are far enough apart that their variations are not fully correlated, as noted in Fertig et al. (2012). So how far is far enough?

We look at data for both wind speed and wind generation, on two continents, and examine correlation vs. distance for wind variations on different timescales. We find, universally, in each region and for both wind speed and wind generation, that: (1) the correlation length saturates for variations on timescales longer than about 38 h, and (2) for shorter timescales τ the correlation length shrinks faster than $1/\tau$.

To our knowledge, this work is the first to articulate a systematic connection between the spatial scales and the temporal scales of wind correlation. Further, in order to unambiguously quantify correlation length, we also introduce a new "non-parametric" measure that does not depend on fitting correlation-vs.-distance data to some presumed functional form. Since it is well known that non-stationarities contaminate correlation-length estimates, we also remove periodic diurnal and seasonal variations in a statistically rigorous way, using techniques more sophisticated and more robust than evidenced in most previous work in this field.

Since grid management requires balancing power production on various timescales, our finding that the shorter the time period under consideration, the systematically smaller the site separation needed for the site pair to become un-correlated should be valuable to grid operators.

The work presented in this chapter reveals remarkable similarities in behavior between three unique datasets that, if universal, could be particularly useful for planning large-scale renewable energy deployment.

The following is adapted and reformatted from:

St. Martin, C. M., Lundquist, J. K., and Handschy, M. A.: Variability of interconnected wind plants: correlation length and its dependence on variability time scale. *Environ. Res. Lett.*, 10, 044004, doi:10.1088/1748-9326/10/4/044004, 2015.

Abstract

The variability in wind-generated electricity complicates the integration of this electricity into the electrical grid. This challenge steepens as the percentage of renewably-generated electricity on the grid grows, but variability can be reduced by exploiting geographic diversity: correlations between wind farms decrease as the separation between wind farms increases. But how far is far enough to reduce variability? Grid management requires balancing production on various timescales, and so consideration of correlations reflective of those timescales can guide the appropriate spatial scales of geographic diversity grid integration. To answer "how far is far enough," we investigate the universal behavior of geographic diversity by exploring wind-speed correlations using three extensive datasets spanning continents, durations and time resolution. First, one year of five-minute wind power generation data from 29 wind farms span 1200 km across southeastern Australia (Australian Energy Market Operator). Second, 45 years of hourly 10-m wind-speeds from 117 stations span 5000 km across Canada (National Climate Data Archive of Environment Canada). Finally, four years of five-minute wind-speeds from 14 meteorological towers span 350 km of the northwestern US (Bonneville Power Administration). After removing diurnal cycles and seasonal trends from all datasets, we investigate dependence

of correlation length on time scale by digitally high-pass filtering the data on 0.25–2000 hour timescales and calculating correlations between sites for each high-pass filter cut-off. Correlations fall to zero with increasing station separation distance, but the characteristic correlation length varies with the high-pass filter applied: the higher the cut-off frequency, the smaller the station separation required to achieve de-correlation. Remarkable similarities between these three datasets reveal behavior that, if universal, could be particularly useful for grid management. For high-pass filter time constants shorter than about τ = 38 hours, all datasets exhibit a correlation length ξ that falls at least as fast as τ^{-1}. Since the inter-site separation needed for statistical independence falls for shorter time scales, higher-rate fluctuations can be effectively smoothed by aggregating wind plants over areas smaller than otherwise estimated.

1 Introduction

Low CO_2 emission footprints make wind and solar power attractive choices for future electricity needs. However, their natural variability is challenging for the electric grid, which requires instantaneous matching of generation and load on all time scales from one AC cycle, through operational scheduling horizons (a day or two), out to planning horizons of more than a decade (von Meier, 2006). Variability can be reduced, and the grid-integration challenge lessened by interconnecting renewable electricity generators distanced enough that their variation is not fully correlated (Thomas, 1945; Kahn, 1979). At a great enough distance which depends on variability time scale as we see here, the wind-speed variations approach statistical independence: an ensemble of wind plants separated at least this distance from each other is "geographically diverse," and at the associated time scale variability of the ensemble's summed power output, will be reduced compared to that of an individual plant.

Better plans for future grids could be made if this effect were better understood. Many previous studies have relied on an empirical approach where the degree of smoothing that might have occurred over a specific region was estimated from historical meteorological or reanalysis data or even calculated from actual renewable generation (Molly, 1977; Palutikof et al., 1990; Landberg, 1997; Milligan and Factor, 2000; Wiemken et al., 2001; Archer and Jacobson, 2003, 2007; Holttinen, 2005; Sinden, 2007; Kiss and Jánosi, 2008; Kempton et al., 2010; Fertig et al., 2012; Fisher et al., 2013; Cosseron et al., 2013; Louie, 2014; Huang et al., 2014). However, it is often difficult to generalize the findings from the study scenario to realistic planning scenarios. As a first step, some have sought to model how correlation falls off with distance, using a variety of different forms: exponential, both with (Haslett and Raftery, 1989; Landberg, 1999; Kiss and Jánosi, 2008; and Katzenstein et al., 2010) and without (Giebel, 2000; Simonsen and Stevens, 2004; Holttinen, 2005; Achberger, 2006; and Kempton et al., 2010) a nugget (non-unity correlation at zero separation), stretched exponentials (Hasche, 2010; Louie, 2014), Gaussian forms (Buell, 1972) and Lorentzian forms (Buell, 1972; Julian and Thebaux, 1975); see Table 1. A few have gone further to propose forms predicting probability distributions of aggregated power as a function of the region size (Justus and Mikhail, 1978; Carlin and Haslett, 1982; Haslett and Raftery, 1989; Hasche, 2010).

How correlations depend on the variability time scale is equally important to how they depend on distance, since, for a given magnitude operational power excursion, the faster the excursion generally the more costly its regulation (Kirby, 2004). Without suggesting a particular functional form for the dependence, studies by Ernst et al. (1999) and by Mills and Wiser (2011) have found for wind and solar, respectively, that faster variations become uncorrelated at smaller spatial separations than slower variations. Variability time scale τ or frequency f can be inserted

into functional forms for correlation ρ vs. distance r by introducing a characteristic velocity v, and replacing correlation length ℓ by $v\tau$ or v/f, as proposed by Davenport (1961). Beyer et al. (1990;1993), McNerney and Richardson (1992), Nanahara et al. (2004), and Sørensen et al. (2008) have taken this approach for wind-speed correlation. Calling $r/(v\tau)$ a 'dispersion factor', Hoff and Perez (2010) introduced this concept to the study of solar variability and identified velocity v with cloud motion; it has since been used in solar correlation studies by Marcos et al. (2012), Lave and Kleissl (2013), and Hinkelman (2013). None of the studies based on characteristic-velocity functional forms have considered regions much larger than 100 km in extent, and more typically have been limited to the size of a single PV plant.

Here we revisit the methods used by Ernst et al. (1999) and by Mills and Wiser (2011), apply them to both wind-speed data and wind generation data from three different geographical regions, and find a single quantitative relationship between correlation length and time scale that parsimoniously characterizes behavior on time scales ranging from an hour to a quarter-year and over distances of a kilometer to a continent.

In Section 2, we highlight the unique features of the datasets used in this analysis as well as novel methods for investigating correlations between sites and quantifying correlation length scales. Section 3 describes the results found in our investigation and Section 4 sums up our conclusions and suggestions for future work. In the provided Supplementary Data, we describe, in detail, the filtering methodology used to eliminate non-stationarities in the time series and present the correlation results from all datasets.

Table 1. Correlation functions found in previous work.

source	functional form (r is distance)	adj. params., length (km)		data description
Buell, 1972	longitudinal: $\exp[-\frac{1}{2}(\alpha r)^2]$	α		500 mb wind data from Europe and the North Atlantic during the summer
	transverse: $[1+(\alpha r)^2]^{-q-1}$,	α, q		
	$[1-(\alpha r)^2]\exp[-\frac{1}{2}(\alpha r)^2]$,	α		
	$[1-(2q+1)(\alpha r)^2](1+(\alpha r)^2)^{-q-2}$	α, q		
Julian and Thiebaux, 1975	$[\alpha\cos(\omega r)+z-\alpha][1+(\lambda r)^2]^{-\gamma}$	$\alpha, \omega, \lambda, \gamma, z$		2 y of 500 mb wind data from North America during the winter (3 months)
Justus and Mikhail, 1978	$\alpha\exp(-r/L)$*	α, L	αL = 395–560*	(fit to data in J&M Fig. B-4) 1 y of 3-hrly data at 10 m from 22 US sites
Haslett and Raftery, 1989	$\alpha\exp(-\beta r)$	α, β	$\alpha\beta^{-1}$ = 722	18 y of hrly mean wind speeds from 12 Ireland stations
Beyer, et al., 1993	$\exp[-(kr)^m]$	k, m	k^{-1} = 870	3 y of hrly mean wind speeds (converted to power) from 4 sites in NW Germany
Landberg, 1999	$\exp(-r/a)-\beta$	a, β	$(1-\beta)a$ = 425	1 y of 10-min power output from 17 wind farms in Denmark
Giebel, 2000	$\exp(-r/D)$	D	D = 723	1 y of hrly 50-m wind speeds from 60 European stations
Simonsen and Stevens, 2004	$\exp(-\alpha r)$	α	α^{-1} = 323–588	1 y of hrly averaged 50-m wind speeds (converted to power) from 28 Midwest US sites
Holttinen, 2005	$\exp(-r/a)$	a	a = 500	1 y of hrly wind power output from 100's of Nordic sites
Gibescu et al., 2006	$\alpha\exp(-\beta r)$	a, β		1 y of 10-min averaged wind speeds for 18 sites in the Netherlands
Achberger et al., 2006	$\exp(-r/x_0)$	x_0	x_0 = 310*	(curve in Achberger Fig. 6a) 2 y of 3-hrly 10-m winds from 142 sites in Sweden
Kiss and Jánosi, 2008	$\exp(-r/L)$	L	L = 400–600	44 y of 6-hrly wind (converted to power) from ECMWF ERA-40 model output
Adams, 2009	$\exp(-\alpha r)$	α	α^{-1} = 333	2 yr of hrly production from wind farms in Ontario
Hasche, 2010	$\exp(-ar^\alpha)$	a, α	$a^{-(1/\alpha)}$ = 322;	1 y of hrly 10-m wind speeds (converted to power) from 24 German sites
			$a^{-(1/\alpha)}$ = 22	as above, 2-hour ramps
Katzenstein et al., 2010	$\alpha\exp(-r/D)$	α, D	αD = 271	15-min power output from 20 wind farms in Texas
Kempton et al., 2010	$\exp(-r/D)$	D	D = 430	5 y of (5-49-m) wind data (converted to power) from 11 stations on the US East Coast
Baïle and Muzy, 2010	$\lambda^2\ln(L/r)$	λ, L	L = 600	17 y of hrly 10-m wind at 27 locations in the Netherlands
Šaltytė Benth and Šaltytė, 2011	$\exp\left(\sqrt{\theta_2 x^2+y^2}/\theta_1\right)$	θ_1, θ_2	θ_1 = 370	($r^2 = x^2 + y^2$) 31 y of daily wind data from 18 stations in Lithuania

Hill et al., 2012	$\alpha \exp(-r/L)$	α, L	αL = 340	multiple y of wind speed from 14 sites in the U.K.
Louie, 2014	$\exp(-\alpha r^{\beta})$	α, β	$\alpha^{-(1/\beta)}$ = 1100	3 yr of hrly power output from US system operators
* our fit to cited data.				

2 Data & Methods

2.1 Datasets

Although previous studies have characterized correlations within an individual region, the present study seeks universal behavior across multiple regions and datasets: an Australian wind generation dataset (AUS), a Canadian wind speed dataset (CAN) and a Bonneville Power Administration wind speed dataset (BPA). The three datasets presented here bring different features to the study, such as wind power production data (AUS), great extent (CAN) or fine time resolution (AUS, BPA). More details on these datasets, including maps of the stations used, appear in the Supplementary Data.

2.1.1 Australian Generation Dataset (AUS)

The Australian Energy Market Operator (AEMO) provides a 1-year (October 2013–October 2014) dataset of five-minute electricity generation data from 32 wind farms across southeastern Australia including the provinces of New South Wales, South Australia, Tasmania and Victoria (Table 2). AEMO reported in 2013 that they might curtail wind power systems in the future (AEMO, 2013); therefore we suspect few curtailment effects in this dataset. We utilize a subset of 29 wind farms, combining production for different wind farm stages and selecting only the larger-producing member of wind farm pairs within 5 km of one another. We make no correction for wake effects of neighboring wind farms (Fitch et al., 2013) in this analysis.

Table 2. Description of datasets used in this work.

Dataset	AUS	CAN	BPA
Location	SE Australia	Canada	NW US
Type of data	wind farm generation	wind speed	wind speed
Height	hub height	10 m	6-53 m
Time Resolution	5 min	1 hr	5 min
Duration	1 y	45 y	4 y
Horizontal Extent	1274 km	5344 km	354 km
Closest Site Pair	8 km	19 km	13 km
Number of stations	29	117	14

The terrain elevations of these wind farms range from 3 m to 900 m above sea level (asl). Plant output data are normalized by each wind plant's generation capacity, which range from 20 MW to 420 MW. The closest pair of farms is separated by 8 km and the farthest by 1274 km.

2.1.2 Canadian Wind Speed Dataset (CAN)

The National Climate Data Archive of Environment Canada provides a 54-year dataset of hourly surface wind-speeds from 117 stations ranging across more than 5000 km of Canada (Table 2). While the entire dataset spans 1953 through 2006, missing data are less frequent in later years, so we use a 45-year subset of data, from 1962–2006. During the data collection, the measurement heights of the stations ranged from 5 m to 32 m above ground level (agl), but Wan et al., (2010) homogenized these data to the standard 10-m height assuming a logarithmic wind profile. The terrain elevations within this dataset vary from sea level to 1084 m asl. Separation distances between sites vary from a minimum of 19 km to a maximum of 5344 km.

2.1.3 Bonneville Power Administration Wind Speed Dataset (BPA)

The Bonneville Power Administration provides a dataset of five-minute wind-speeds from meteorological towers in Washington and Oregon in the northwestern US (Table 2). For

this analysis, we use data from 14 sites from 2010–2014 due to the higher temporal resolution of these data, although several stations provide data for longer durations with lower time resolution (Bonneville Power Administration).

These 14 towers in the BPA network are generally located along the Columbia River Gorge on the border of Washington and Oregon or along the Pacific Coast. The elevations of these stations range from 19 m to 1261 m asl. The anemometer heights range from 9 m to 53 m agl. No "standard height" homogenization methodology is used on this dataset; correlation coefficient calculations between sites would be unchanged if either a logarithmic wind profile was assumed or the wind power law was used to homogenize the measurements to a 10 m height. Separation distances between sites vary from a minimum of 13 km to a maximum of 354 km.

2.2 Data processing

2.2.1 Pre-processing

Although both deterministic variability, such as diurnal or seasonal cycles, and random or stochastic variability will figure in any complete accounting of wind power variability, it is the stochastic phenomena that are less understood and not as predictable; so we focus on them here. The analysis of underlying stochastic components is complicated by the presence of temporal periodicities, as noted by Haslett and Raftery (1989), Gunst (1995), Robeson and Shein (1997), Achberger et al. (2006), and Hill et al. (2012). To remove the diurnal cycle in order to more clearly characterize stochastic spatial correlations, we make a "local" estimate of the amplitudes of the first four daily harmonics by least-squares fitting using a 90-day moving window to allow for seasonal variation in the daily cycle (Baïle et al., 2011). This cycle, estimated once for each of the days in the dataset, is subtracted from that day's wind-speed or power data, as further

described in the Supplementary Data. By also subtracting the 90-day moving average, we remove low-frequency variability, including the seasonal or annual cycle.

As shown by previous investigators (Ernst et al., 1999), rapid wind-speed or power variations become uncorrelated at smaller spatial separations than do slow variations. In order to further investigate this effect, we prepare versions of each time series with trends slower than a chosen time-constant removed by calculating the average of the wind speed or power data over a segment centered at each time point and subtracting the segment average from the value at the center point. By varying the width of the segment ("window width"), we control the corner frequency of this high-pass filtering operation. Our process, described further in the Supplementary Data, differs from that used by Ernst et al. (1999), Mills and Wiser (2011), and Hinkelman (2013) in that it subtracts from the original data an averaged version of that data, rather than calculating "ramps" by differencing one block average value from the next. Thus, the number of data points in the filtered versions of our time series is reduced from the original only by the width of filter window, rather than being decreased by a factor of the window width. We analyze the effects of high-filtering for window widths $\tau \leq 1049$ h, and denote by $\tau = 2160$ h data from which the 90-day seasonal bias term has been subtracted but no further filtering applied.

2.2.2 Correlation length

After pre-processing the data as described above and discussed in more detail in the Supplementary Data, we calculate correlations between each pair of stations for each high-pass filtered version of the data. The scatter plot in Fig. 1, for example, shows the correlation data for CAN at filter window τ = 65 hours. Given the high degree of scatter shown here, estimating a

single correlation length for each dataset at each filtering window τ is problematic since a functional form of correlation vs. distance appropriate for fitting is not known *a priori*.

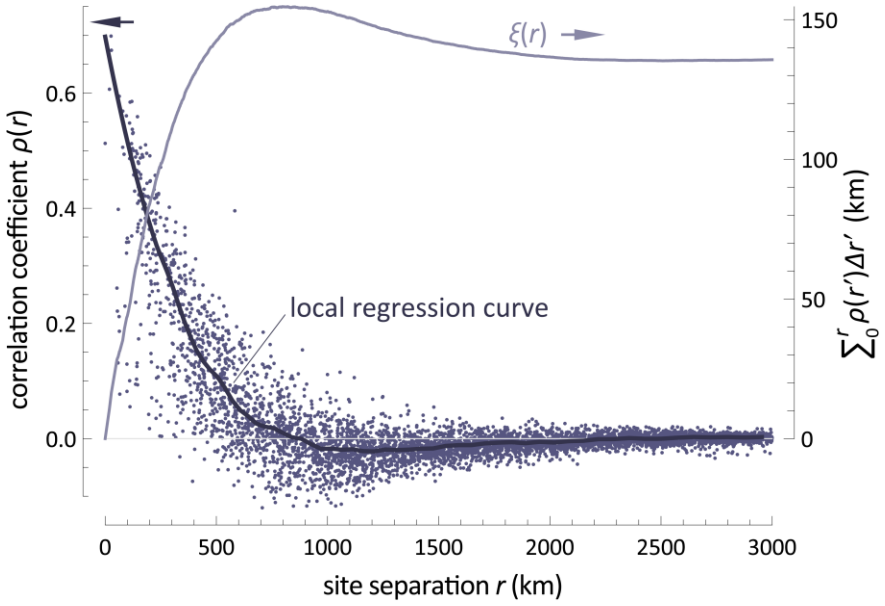

Figure 1. Correlation vs. distance for CAN data high-pass filtered with τ = 65 h (scatter plot and dark-blue local-regression curve, left axis). Numerically integrated correlations as a function of integration range (integration of scatter points, light-blue curve, right axis).

Wishing to avoid the functional-form conundrum, we sought a "non-parametric" distance measure. For a given averaging window width τ we order the correlation coefficient values ρ_{ij} by increasing station separation distance, with increasing values of separation distance signified with single index as r_k, r_1 denoting the smallest separation (the closest pair of stations) and r_N denoting the largest separation (the farthest pair). We then numerically "integrate" the correlation data over distance using the trapezoid rule:

$$\xi(r_n) = \sum_{k=1}^{n} \frac{1}{2}(r_k - r_{k-1})\left(\rho_{r_k} + \rho_{r_{k-1}}\right) \tag{1}$$

In the familiar case $\rho(r_i) = \exp(-r_i/\ell) + \varepsilon_i$, where ε_i is mean-zero noise, this procedure gives $\xi = \ell$ in the limit of large r. For our observations, we take $r_0 \equiv 0$, and estimate ρ_{r_0} as the intercept of a local regression curve (see Section 2.2.3 below). As shown by the light blue line in Fig. 1, $\xi(r_n)$ varies smoothly with r_n and approaches a near-constant value at the largest separations (here 139 km at r_N = 5300 km) as the ρ_{r_k} scatter there around zero. We refer to the value at the greatest separation $\xi(r_N)$ (at a given high-pass filter window width τ hereinafter ξ_τ) as the *correlation length*; it has a meaning similar to Bretherton's "correlation radius" (1999) or the term "integral scale" in turbulence (Batchelor, 1959). Our methodology bears some resemblance to that of Şen's cumulative semivariogram (Şen, 1989; Şen and Şahin, 1997).

2.2.3 Local regression curves

To facilitate graphical comparisons of correlation vs. distance behaviors that might otherwise be obscured by the high degree of scatter in the individual $\rho(r_k)$ values, we also calculate $\rho(r)$ curves using local regression techniques (Cleveland 1979), where, to find the curve value at a given site-separation distance r', we fit a 2nd-order polynomial to the fraction α of the correlation data points that are closest to the given distance (for example in the CAN dataset and choosing α = 0.05, the 339 correlation data points out of 6786 total having the smallest values of $|r - r'|$). This gives results as exemplified by the thick blue line in Fig. 1.

2.2.4 Importance of pre-processing

The high-pass filtering and diurnal-cycle removal (outlined in detail in the Supplementary Data) have significant effects on the correlation behavior, as shown in Fig. 2, which, to facilitate comparison, portrays correlation vs. distance as local regression curves. With no pre-processing (raw data, dashed brown curve), correlation does not fall below about 0.04 at the

largest site separations, while with the diurnal cycle and seasonal bias removed (solid brown curve), correlation falls to zero. For raw data high-pass-filtered with τ = 33 h (aqua), the correlation doesn't fall below about 0.10 (dashed curve) for separations smaller than 4000 km, while if the high-pass filter is applied to data from which the diurnal cycle has first been removed, correlation falls to near zero for separations of 600 km (solid curve). High-pass cutoffs of τ = 25–37 h give similarly high correlation floors on raw data while the height of the floor decreases noticeably for cutoffs smaller than 21 h or larger than 41 h.

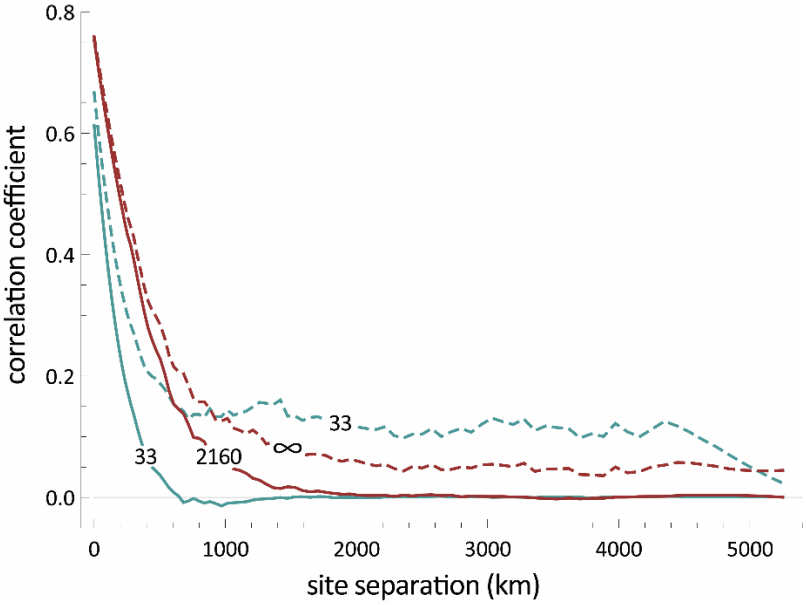

Figure 2. Effect of diurnal-cycle and low-frequency removal on 1962–2006 CAN hourly data correlation (local regression curves). Brown: no pre-processing (dashed, ∞); diurnal-cycle and seasonal bias removed (solid, 2160). Aqua: τ = 33 h high-pass filtered with diurnal cycle subtracted (solid, 33) and without diurnal-cycle subtracted (dashed, 33).

3 Results and Discussion

3.1 Correlations

Despite the differences in methodology, the behavior of correlation with distance and high-pass filtering window width qualitatively resembles the previous wind-power results of Ernst et al. (1999) and insolation work of Mills and Wiser (2011): correlation falls off more rapidly with site separation the smaller the window-width τ, as seen for the CAN data in Fig. 3. Interestingly, we observe that for some high-pass filter window widths (for example, a 65-hr window width in CAN), the correlations actually become negative between 500-km and 1000-km separation distances, perhaps for reasons similar to those identified for solar correlations by Hoff and Perez (2010) and Hinkelman (2013).

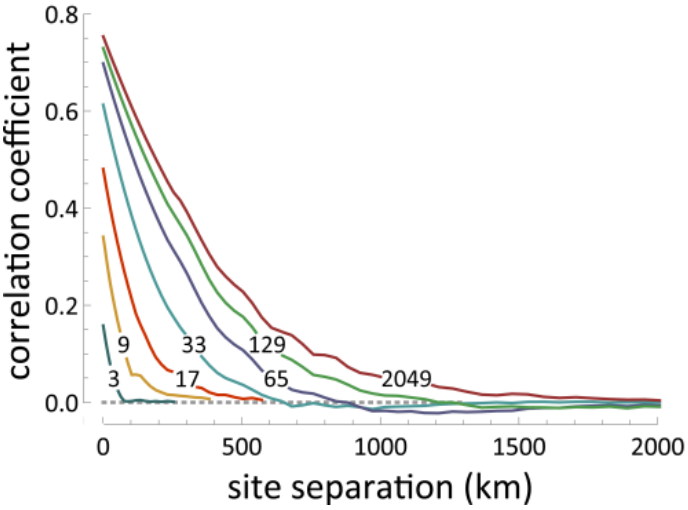

Figure 3. CAN correlation coefficients vs site separation simplified by robust local regression for multiple indicated high-pass window widths in hours.

Substantial scatter of the correlation vs. distance values is a prominent feature of data from all three regions at all but the shortest filter widths (see Supplementary Figs. 5-7). We explored several potential causes of this large scatter as well as the negative correlations by

separating stations by region (north vs. south as well as east vs. west) and by azimuthal bearing. East/west differences (Fig. 4a) and north/south differences (Fig. 4b) explain neither the scatter nor the slight anti-correlations. It is clear from previous work (Buell, 1972, Ramanathan et al., 1973; Julian and Thiebaux, 1975) that the longitudinal and transverse horizontal wind components have different correlation behaviors, with the transverse correlation falling faster and exhibiting more negative values, similar to the behavior of fully developed turbulence (von Kármán, 1948; Batchelor, 1953). Unfortunately, the CAN dataset provides wind speed but not wind direction. Nevertheless, some of the scatter in the CAN correlations can be attributed to the azimuthal bearing of each station pair, as stations separated along a line 10° North of West-East are systematically less correlated and more often anti-correlated than those perpendicular to that line (Fig. 4c). Šaltytė Benth and Šaltytė (2011) also observed directional anisotropy in wind-speed correlation fall off. We presume the anisotropy we observe arises from the prevailing westerly winds produced by the large-scale circulation in this region, although, contrary to our expectation, we see higher correlations for stations separated along the crosswind direction.

Finally, given previous work that has identified a connection between the interannual climate oscillation of the El Niño Southern Oscillation (ENSO) and Canadian wind resources (St. George and Wolfe, 2009), we separated the time series into intervals with strong climate signals (1988–1989 La Niña and 1982–1983 El Niño, 1964–1965 La Niña and 1965–1966 El Niño, 1970–1971 La Niña and 1972–1973 El Niño), and calculated each site-pair's correlation coefficient over the El Niño interval and over the La Niña interval. Comparison of all these periods gave results similar to that seen in Fig. 4d for the 1964–1966 periods. No difference in correlations between El Niño and La Niña periods emerges (Fig. 4d). The pairwise differences between the '65–66 El Niño and the '64–65 La Niña correlations have mean $|\mu| = 0.0011$ and

standard deviation 0.044 (see Fig. S8); the non-parametric sign test of null hypothesis H_0 that $\mu = 0$ against alternative hypothesis H_1 that $\mu \neq 0$, fails to reject H_0 with a p-value of 0.12.

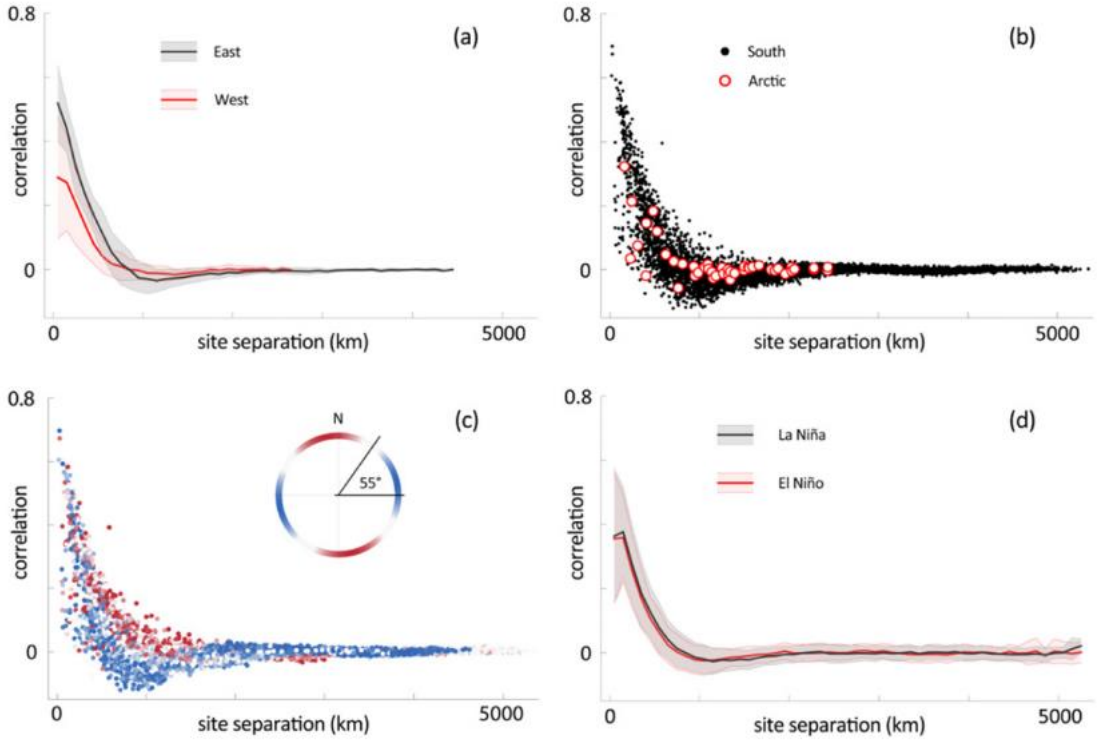

Figure 4. Correlation vs station separation for τ = 65 h high-pass filtered CAN 1962–2006 hourly data. (a) Red: 1326 station pairs west of 100°W longitude, black 2080 station pairs east of 100°W longitude. Means of 100-km-wide bins are shown by the solid line; the envelope represents ± one standard deviation σ; (b) red: 45 station pairs north of the Arctic Circle, black: 5671 station pairs south of the Arctic Circle; (c) azimuth of each station-pair bearing indicated by color in compass; (d) correlations during a 19-month period of strong El Niño (red) and during a 19-month period of strong La Niña (black). Means of 100 km wide bins are shown by the solid line; the envelope represents ± one standard deviation σ.

3.2 Correlation length estimates

Figure 5 shows the results of our "integral-scale" calculations for CAN, AUS and BPA. The 5300-km geographic extent of Canada clearly exceeds the observed correlation lengths,

allowing the integration to fully saturate for even the widest filter, giving $\xi_{2160\,\mathrm{h}}$ = 273 km. The AUS data yield slightly larger values, with $\xi_{2160\,\mathrm{h}}$ = 368 km. The geographic extent of the BPA region is not sufficient for the correlation integration to saturate, making the $\xi_{2160\,\mathrm{h}}$ = 89 km obtained an underestimate of the full correlation length.

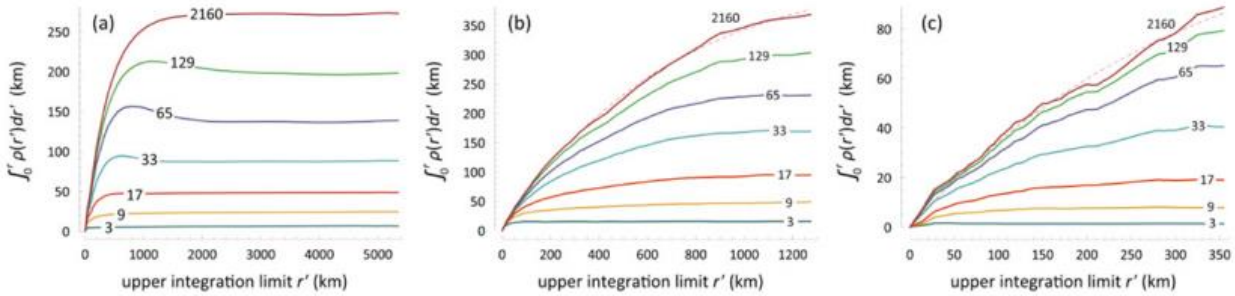

Figure 5. Numerically integrated correlation as a function of integration range for indicated high-pass filter window widths in hours for: (a) CAN, (b) AUS, and (c) BPA; 2160-h curves result from removal of diurnal cycle and 90-day moving average—curves with shorter window widths are further high-pass filtered. Dashed lines in (b) and (c) are least-squares fits to the form $\beta\ell[1 - e^{-(r/\ell)}]$, giving at τ = 2160 h β = 0.65 and ℓ = 685 km for AUS, β = 0.40 and ℓ = 323 km for BPA. Similar fit gives β = 0.70 and ℓ = 388 for CAN (not shown).

Figure 6 shows the variation of correlation length ξ_τ with high-pass filter cutoff τ for the three regions; the ξ values for each region normalized by the maximum to facilitate comparison between datasets. The envelope surrounding the correlation length values as a function of τ indicates an empirically-found range of behavior common to all three datasets:

$$\frac{1}{\left[1+\frac{38\ \mathrm{h}}{\tau}\right]^2} < \frac{\xi_\tau}{\xi_{\max}} < \frac{1}{\left[1+\left(\frac{38\ \mathrm{h}}{\tau}\right)^2\right]^{½}} \qquad (2)$$

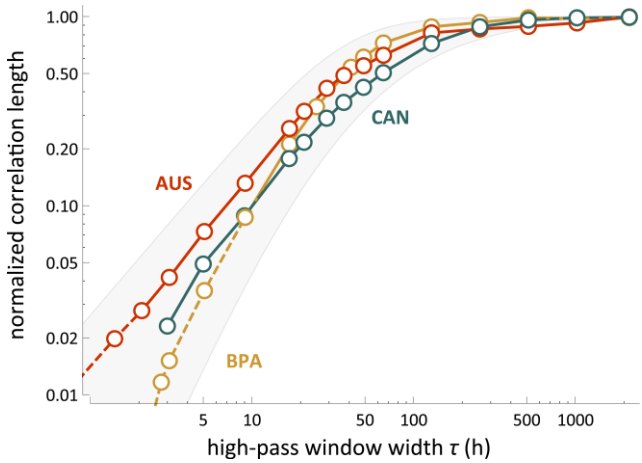

Figure 6. Correlation length vs high-pass window width for AUS, CAN and BPA data; shaded envelope spans $[1 + \tau_0/\tau]^{-2}$ to $[1 + (\tau_0/\tau)^2]^{-½}$, with τ_0 = 38 h. Dashed curve segments dependent on non-zero nugget.

3.3 Discussion

The characteristics of the correlation length-scale metric introduced in equation (1) and used above deserve further explication. This measure has the advantage that it is essentially free of assumptions about the functional form of the correlation vs. distance data. It quantifies the site-separation distance needed to reduce average inter-station correlation to a small value. However, it is important to remember, especially with data with such large scatter as observed here, that ξ_τ is just one of multiple possible measures of "how far is far enough". For example, as seen in Fig. 1 for the CAN data, numerically integrating the scattered $\rho(r)$ points according to equation (1) gives $\xi_{65\,\mathrm{h}}$ = 139 km (right-hand end of light-blue curve) while integrating the dark-blue robust local-regression curve for the same window width gives the significantly larger value of 172 km (integral not shown). This occurs because the residuals of the local-regression fit are negatively skewed, and the "robust" fitting process (Cleveland, 1979) pulls the fit towards the median by assigning small weights to points determined to be outliers; here more often below the curve than above.

The integral-scale metric ξ_τ measures the separation distance required for correlation to fall to a value small compared to unity; this can be substantially less than the distance ℓ over which it falls to a fraction (say, 1/*e*) of its initial value (at $r = 0$) if the initial value is small. This discrepancy between the integral-scale metric and the 1/*e* distance ℓ can be seen from the parameters of fitting of an exponential form to the data, as shown by the dashed-lines in Fig. 5 (b) and (c). Here we fit $\xi(r) = \beta\ell(1 - e^{-r/\ell})$ as would be the case for correlation falling as $\beta e^{-r/\ell}$ with distance. Fitting results are shown in Table 3. Due to the large nugget effect (Matheron, 1963) observed in all three regions, the best-fit correlation at zero site-separation, β, is substantially smaller than unity, proportionately reducing the area ξ under the $\rho(r)$ curve. For the CAN data this gives $\xi(r_N) \approx \beta\ell$, but in the AUS and BPA regions $\xi(r_N) < \beta\ell$ since the regions sizes do not permit separations *r* large enough to bring $\rho(r)$ to zero and hence to bring ξ to saturation.

The nugget effect has a particularly strong influence on ξ_τ values at small τ. Had we constrained $\rho(0) = 1$ rather than estimating the value at the origin using local regression, Figure 6 would have shown the decline in ξ_τ/ξ_{2160} ending at a floor value limited by our trapezoid-rule integration to half the separation of the closest site pair (0.03, 0.01, and 0.07 for CAN, AUS, and BPA, respectively), affecting only the dashed portion of the curves.

Table 3. Comparison of least-squares fit parameters (β, ℓ) to integral-scale correlation-length metric ($\boldsymbol{\xi_{max}}$).

Dataset	τ (hr)	β	ℓ (km)	$\beta\,\ell$ (km)	ξ_{max} (km)
CAN	2160	0.70	388	273	273
AUS	2160	0.65	685	447	368
BPA	2160	0.40	323	130	89

4 Conclusions

Variability in wind-generated electricity can be reduced by interconnecting wind farms across large regions, as distant wind farms are only weakly correlated. We investigate the geographic extent needed for this aggregation to be effective using three extensive data sets. Using a "non-parametric" estimator ξ based on the area under the correlation vs. distance curve, we found for the slowest variabilities ξ_{max} = 273 km for 10-m wind speeds in Canada, 368 km for wind-plant generation in southeastern Australia, and 89 km for tower wind-speeds in the northwestern US. Since the Australia and BPA regions are small enough that even for the most distant sites correlation never drops to zero, our ξ values for the widest filter window-widths are underestimates of the extent needed for fully effective aggregation. Quantities more representative of the extent needed for smoothing the slowest variabilities are given by the larger $\beta\ell$ values of 447 km and 130 km respectively, in Table 3, obtained by fitting $\xi(r)$ to the form $\beta\ell(1 - e^{-r/\ell})$ and extrapolating ξ to $r = \infty$. These values can be compared to like values from previous work listed in Table 1.

Although the regional length scales have different magnitudes, we find a dependence of ξ on variability time-scale that is remarkably similar across the three regions, as seen in Fig. 6. At time scales τ shorter than 38 hours, ξ falls at least as fast as τ^{-1}, while at longer scales it is essentially constant. Thus, on time scales longer than a day or so the variability-reduction benefit of aggregating wind power over a region of a given size will be independent of time scale. For time scales shorter than a day, the faster the variability, then the more smoothing that region could provide. It is the shrinking of correlation length with time scale that gives high-frequency spectral slopes a larger magnitude for power aggregated over a region compared to a single site (Beyer et al., 1990; McNerney and Richardson, 1992; Nanahara et al., 2004; Katzenstein et al.,

2010; Tarroja et al., 2011; Fertig et al., 2012); similarly for solar power (Curtright and Apt, 2008; Marcos et al., 2011).

Our findings help disentangle the effects on variability reduction of *generator number*, *region size*, and variability *time scale*. In general, aggregating the outputs of N uncorrelated generators should reduce variability magnitudes by a factor of $\sqrt{N}$. A geographic region of area A has roughly $N \approx A/(2\xi)^2$ potential uncorrelated sites; thus, for a fully populated region (Hasche, 2010) variability could be attenuated by a factor up to $\sqrt{A}/(2\xi)$. For time scales shorter than $\tau \approx 1.5$ days, the number of potential uncorrelated sites within a fixed area, and hence achievable attenuation, grows at least as fast as $1/\tau$. If the actual number of generators in a region is less than $A/(2\xi)^2$, the lesser number will determine attenuation.

Further work to better understand whether the high degree of scatter in correlation vs. distance is a stable manifestation of some unidentified geographic process or is just persistent, random temporal variation that would average away over longer records would improve model utility. Additionally, analysis of solar data over a large region could determine if time and length scale of solar variability are linked in a way similar to what we found here for wind.

Acknowledgements

Wind data used in this work was provided by the Australian Energy Market Operator (AEMO), Environment Canada, and the Bonneville Power Administration, United States Department of Energy. This work was partially supported by a seed grant from Colorado Research and Education in Wind. This material is based upon work funded by the National Science Foundation under Grant IIP-1332147.

CHAPTER III

STABILITY AND TURBULENCE EFFECTS ON POWER CURVES

Global growth in wind development suggests an increasing reliance on wind generation, motivating efforts to refine all steps of the wind resource assessment and power performance testing processes, including the calculation of annual energy production (AEP), a critical parameter for wind farm financing pre- and post-wind farm construction. The AEP depends both on the wind speed distribution at a site and the wind turbine power curve. Calculating and understanding a wind turbine power curve is crucial for power performance testing and AEP assessments.

We use 2.5 months of detailed upwind and nacelle-based measurements from a utility-scale wind turbine and calculate power curve and AEP and explore their sensitivity to different atmospheric parameters. We find that: (1) increased turbulence intensity (TI) and turbulence kinetic energy (TKE) undermines power production at wind speeds near rated, but increases power production at lower speeds, (2) decreased stability as defined by the Bulk Richardson number undermines power production at wind speeds near rated, but increases power production at lower speeds, and (3) wind resource estimates that fail to consider these atmospheric regimes may overestimate the AEP.

In this chapter we suggest that different power curves be calculated for different conditions, which will allow for a more refined understanding of how the turbine is operating in different atmospheric conditions, and may lead to a more accurate and reliable performance result and AEP calculation.

The following is adapted and reformatted from:

St. Martin, C. M., Lundquist, J. K., Clifton, A., Poulos, G. S., and Schreck, S. J.: Wind turbine power production and annual energy production depend on atmospheric stability and turbulence, Wind Energ. Sci., 1, 221-236, doi:10.5194/wes-1-221-2016, 2016.

Abstract

Using detailed upwind and nacelle-based measurements from a General Electric [GE] 1.5sle model with a 77-m rotor diameter, we calculate power curves and annual energy production (AEP) and explore their sensitivity to different atmospheric parameters to provide guidelines for the use of stability and turbulence filters in segregating power curves. The wind measurements upwind of the turbine include anemometers mounted on a 135-m meteorological tower as well as profiles from a lidar. We calculate power curves for different regimes based on turbulence parameters such as turbulence intensity (TI) as well as atmospheric stability parameters such as the Bulk Richardson number (R_B). We also calculate AEP with and without these atmospheric filters and highlight differences between the results of these calculations. The power curves for different TI regimes reveal that increased TI undermines power production at wind speeds near rated, but TI increases power production at lower wind speeds at this site, the U.S. Department of Energy (DOE) National Wind Technology Center (NWTC). Similarly, power curves for different R_B regimes reveal that periods of stable conditions produce more power at wind speeds near rated and periods of unstable conditions produce more power at lower wind speeds. AEP results suggest that calculations without filtering for these atmospheric regimes may overestimate the AEP. Because of statistically-significant differences between power curves and AEP calculated with these turbulence and stability filters for this turbine at this site, we suggest implementing an additional step in analyzing power performance data to incorporate effects of atmospheric stability and turbulence across the rotor disk.

1 Introduction

Power performance testing and annual energy production (AEP) assessments rely on accurate calculations of wind turbine power curves. Previous work on power performance highlights the role of turbulence intensity (TI) and wind shear in influencing power production (Elliot and Cadogan, 1990; Hunter et al., 2001; Kaiser et al., 2003; Sumner and Masson, 2006; Gottschall and Peinke, 2008; Antoniou et al., 2009; Rareshide et al., 2009; Wharton and Lundquist, 2012a, 2012b; Clifton et al., 2013a; Dörenkämper et al., 2014). Wharton and Lundquist (2012b) also found that vertical TI and turbulence kinetic energy (TKE) affect power performance and Rareshide et al. (2009) found that veer affects power performance. Atmospheric stability induces deviations of power from the manufacturer power curve (MPC) (Motta et al., 2005; van den Berg, 2008; Vanderwende and Lundquist, 2012; Wharton and Lundquist, 2012b), and atmospheric variations across the rotor disk can influence power performance results (Sumner and Masson, 2006; Wagner et al., 2009; Choukulkar et al., 2016).

Because the power curve so closely impacts AEP, factors that influence power performance typically influence AEP calculations as well. As suggested by the works mentioned above, the two most closely explored atmospheric factors with regard to AEP are TI and wind shear, but the existing studies do not agree on the influence of TI and wind shear on AEP. The simulation-based study of Antoniou et al. (2009) found that low wind shear supported high AEP. For low wind speeds, the highest AEP occurred during conditions of high TI, but at higher wind speeds, the highest AEP occurred when TI was low. In contrast, based on data from a number of wind farms in the continental United States, Rareshide et al. (2009) also compared AEP calculated with different TI and shear combinations, and found that AEP typically decreased with increasing TI, but increased with increasing shear.

In this study, we also investigate the influence of different atmospheric stability and turbulence regimes on wind turbine power curves and AEP calculations, incorporating a broad set of atmospheric parameters as well as different approaches to measuring these parameters. In Sect. 2 we describe our data set, which includes an upwind meteorological (met) tower with measurements spanning the rotor disk as well as a wind-profiling lidar. In Sect. 3 we present our data analysis methods, which include filtering the data by atmospheric parameters like shear, TI, and atmospheric stability. The effects of atmospheric parameters on power curves and AEP are presented in Sect. 4, and in Sect. 5 we summarize conclusions about the effects of atmospheric stability and inflow turbulence on power curves and AEP calculations.

2 Data

2.1 Measurement site

The measurements used in this analysis were collected at the U.S. Department of Energy (DOE) National Wind Technology Center (NWTC, Fig. 1) at the National Renewable Energy Laboratory (NREL), located just south of Boulder, Colo., and about 5 km east of the Colorado Front Range (Clifton et al., 2013b; Aitken et al., 2014b). The prevailing wind direction at 80 m (hub height) at this site during this campaign (29 November 2012 – 14 February 2013) was west–northwesterly.

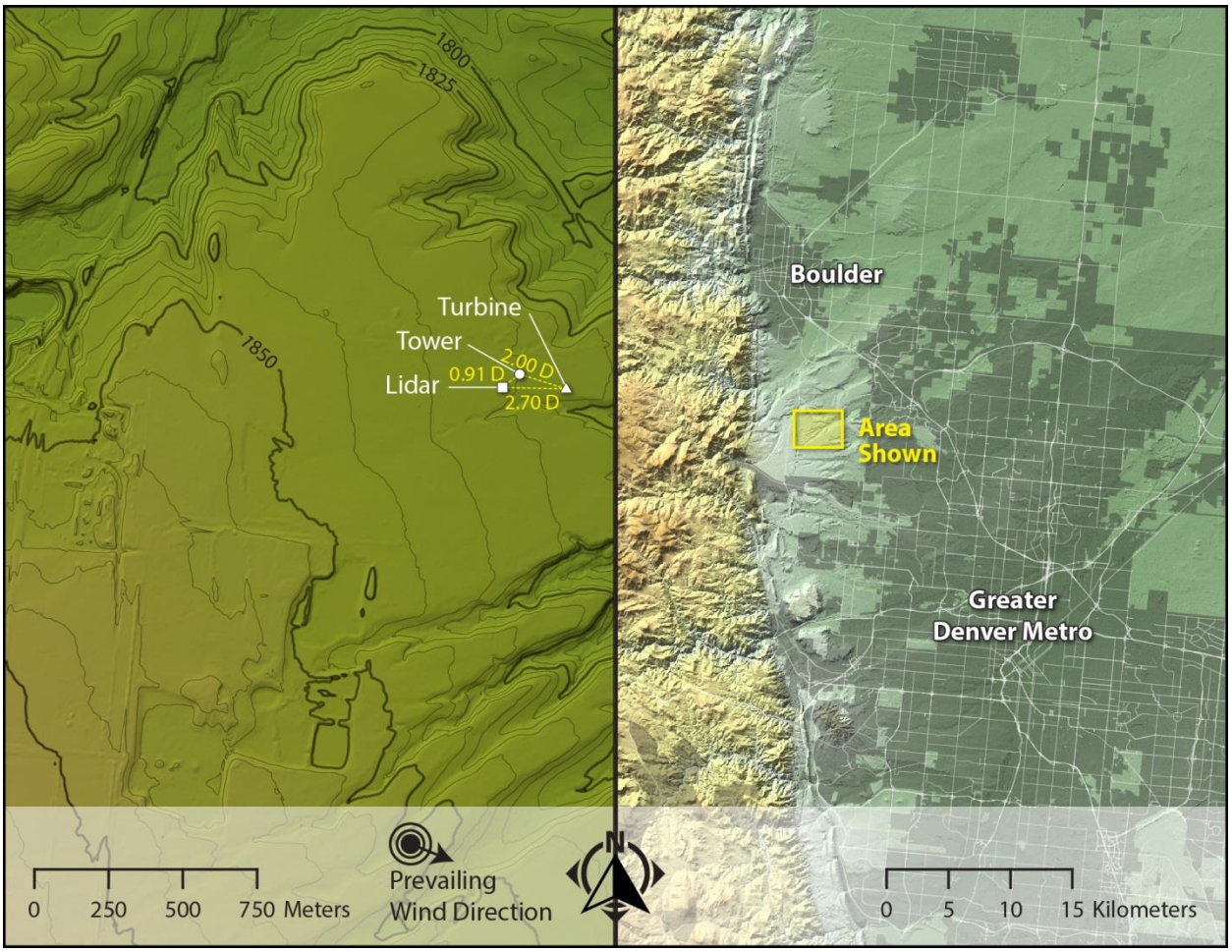

Figure 1. Left: Local map of the NWTC with instrument locations and topographic contours in meters above sea level. Right: The regional setting of the NWTC between the Greater Denver Metro area and Boulder, with the Front Range of the Rocky Mountains shown in the higher topography west of the site. (Courtesy of Joshua Bauer and Billy Roberts at NREL.)

This wind direction also dominated a 14-year period from a neighboring met tower at the NWTC (Clifton and Lundquist, 2012). During the winter, the downslope flow from the nearby Rocky Mountains is frequently channeled through Eldorado Canyon, located just west-northwest of the NWTC (Banta et al., 1996; Poulos et al., 2000, 2007; Clifton et al., 2013b; Aitken et al., 2014b). The NWTC site slopes upward with about 20 m in elevation change toward the west for about 1.5 km before dropping off 20 m towards the highway on the western edge of the site. The surface is mostly short grass.

2.2 Upwind measurements

Upwind measurements were taken using a Renewable NRG Systems (NRG)/LEOSPHERE WINDCUBE v1 vertically-profiling Doppler lidar (Courtney et al., 2008; Rhodes and Lundquist, 2013) and a 135-m met tower. The tower supports several levels of cup anemometers, vanes, sonic anemometers, and temperature sensors, along with precipitation and air-pressure sensors (Fig. 2, Table 1) all on booms pointing in the dominant wind direction (west-northwest). Data were collected during the winter season, typically the season of the strongest winds at the NWTC (from 29 November 2012 through 14 February 2013). The lidar is located about 216 m (2.7 D) west of the General Electric (GE) 1.5sle turbine on the NWTC site. The met tower is located approximately 160 m (2.0 D) west-northwest of the turbine (Fig. 1). Because different instruments employ different averaging methods, Fig. 3 demonstrates that all wind speed data sets were synchronized and illustrates how the power output responds to changes in wind speed.

2.2.1 Lidar

The NRG/LEOSPHERE WINDCUBE v1 lidar measures volumetric-averaged wind speeds and directions every 20 m from 40 m to 220 m, thereby spanning the entire vertical extent of the turbine rotor disk. The wind speeds are measured with an accuracy of 0.2 m s^{-1} and the wind directions are measured with an accuracy of 1.5° (Courtney et al., 2008). First, we filtered the nominally 1-Hz measurements of the horizontal wind speeds and directions for suitable carrier-to-noise ratio (CNR). Next, we averaged these 1-Hz data to 10-min averages for comparison with the tower and turbine data. The lidar takes a volumetric measurement, assuming homogeneity over the entire volume it is measuring. This process introduces an uncertainty in the lidar measurements in inhomogeneous flow (Bingöl et al., 2009; Rhodes and Lundquist,

2013; Lundquist et al., 2015); this possible source of error is discussed in further detail in the supplement (Sect. S1).

2.2.2 Meteorological tower

The M5 met tower (NWTC, 2016, similar to the M4 tower at the site, which was studied by Rinker et al., 2016) is instrumented with cup anemometers at 3, 10, 30, 38, 55, 80, 87, 105, 122, and 130 m, and vanes at 3, 10, 38, 87, and 122 m (Fig. 2 and Table 1). Barometric pressure and precipitation sensors are located at 3 m and temperature sensors at 3, 38, and 87 m (Table 1). Sonic anemometers are mounted at 15, 41, 61, 74, 100, and 119 m (Fig. 2 and Table 1). The tower booms are directed at 278°, into the prevailing wind direction, slightly north of west. Measurements from the sonic anemometers at 15 and 74 m are used to calculate turbulent fluxes of momentum and heat for assessment of atmospheric stability and turbulence as discussed in the following sections.

2.3 Wind turbine data

A GE 1.5MW turbine (GE 1.5/77 sle) with an 80-m hub height was chosen for this study. The GE 1.5MW is the most widely deployed utility-scale turbine in the world with more than 12,000 turbines deployed around the globe as of 2009 (GE Energy, 2009). The supervisory control and data acquisition (SCADA) system of the turbine provides 10-min averages of nacelle wind speed, nacelle orientation, turbine power, blade pitch angles, and generator speed set point. These measurements can be compared with the upwind measurements to quantify power curves and AEP. The cup anemometer mounted on the nacelle of the turbine is a NRG IceFree Hybrid XT Turbine Control Anemometer. The GE 1.5sle reaches its nameplate capacity, 1.5 MW, at a wind speed of 14 m s^{-1} (GE Energy, 2009). We refer to this wind speed as the rated wind speed

for the rest of this article. The lower and upper extremes of the swept area of the GE 1.5sle in this study are approximately 41.5 m and 118.5 m above ground. More details on this turbine and power performance testing results as well as instrument and site calibration information can be found in Mendoza et al. (2015).

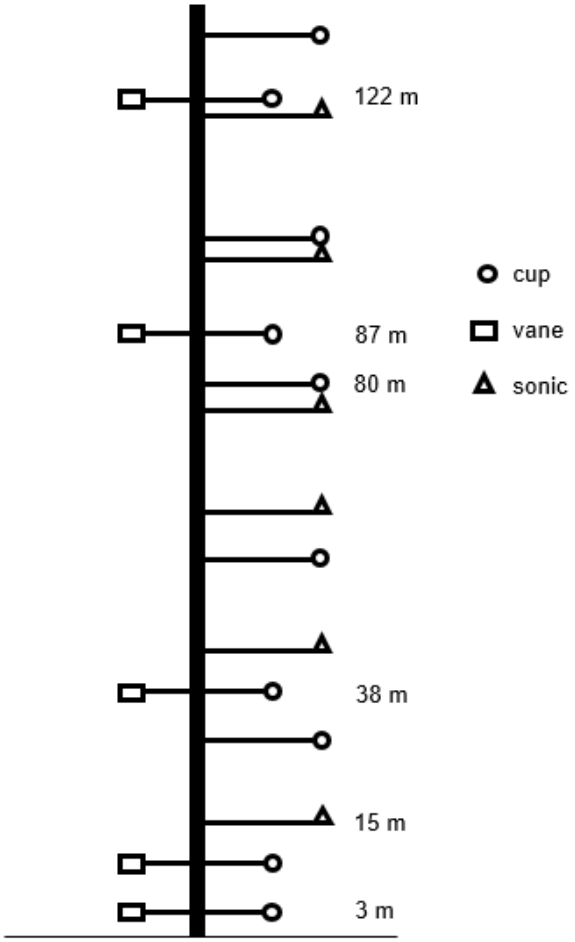

Figure 2. 135-m meteorological tower configuration with some key heights labeled. This tower varies slightly from the M4 tower described in Clifton et al. (2013b), but data are available online (NWTC, 2016).

Table 1. 135-m met tower instrument information.

Type	Instrument	Mounting Heights (m)	Accuracy
Cup anemometer	Met One SS-201	3, 10, 38, 87, 122	0.5 m s^{-1}
Cup anemometer	Thies 4.3351.10.0000	30, 55, 80, 105, 130	0.2 m s^{-1}
Wind vane	Met One SD-201	3, 10, 38, 87, 122	3.6°
Air temperature sensor	Met One T-200A platinum RTD	3, 38, 87	0.1°C
Differential temperature sensor	Met One T-200A	38, 87, 122	0.1°C
Sonic anemometer	ATI 'K' type	15, 41, 61, 74, 100, 119	0.01 m s^{-1}
Boom triaxial acceleration sensor	Summit 34201A	15, 41, 61, 74, 100, 119	
Sonic temperature	ATI 'K' type	15, 41, 61, 74, 100, 119	0.1°C
Barometric pressure sensor	AIR AB-2AX	3	
Dew point temperature sensor	Therm-x 9400ASTD	3, 38, 87, 122	
Precipitation sensor	Vaisala DRD11A	3	

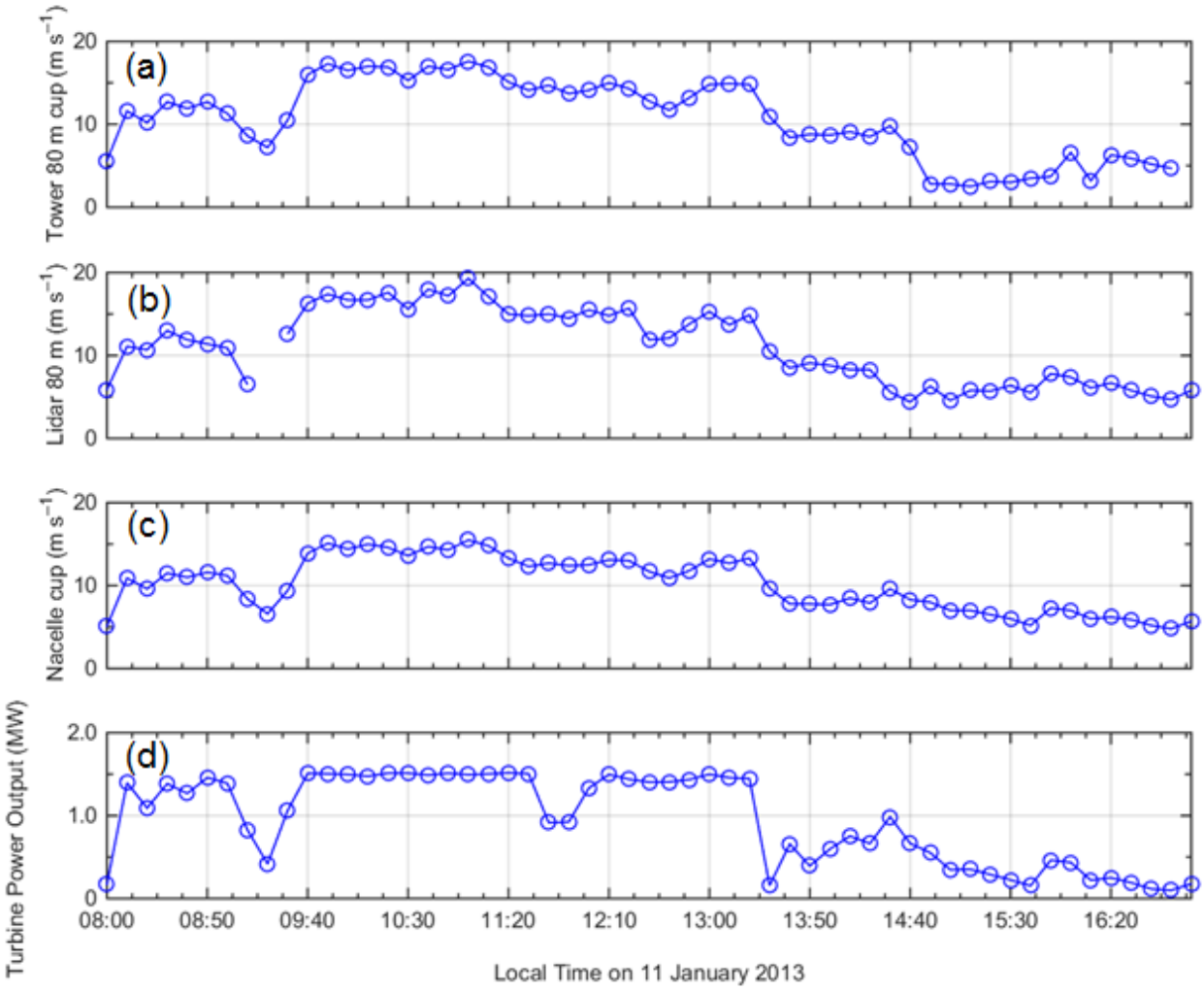

Figure 3. Time series from 11 January 2013 from 08:00 to 17:00 Mountain Standard Time (MST): (a) is a time series of 80-m wind speeds measured by the cup on the tower; (b) is a time series of 80-m wind speeds measured by the lidar; (c) is a time series of the hub-height wind speeds measured by the cup anemometer on the nacelle; and (d) is a time series of the power output from the turbine.

3 Analysis methods

Before calculating atmospheric parameters, all meteorological and turbine data are checked for data quality as described in Sect. 3.1.

3.1 Data quality control

3.1.1 Lidar

All lidar-measured wind-speed measurements are filtered by CNR: only measurements with a CNR greater than –18 dB are retained. Lower CNR results from clean-air conditions (Aitken et al., 2012), which occur frequently on Colorado's Front Range in the winter. After additional filtering for quality control purposes (such as removing bad data as defined by the manufacturer's wind speed and temperature limits), the data recovery rate is approximately 33.5 % for horizontal wind speeds and directions at 40 m, 40 % for horizontal wind speeds and directions at 60 and 120 m, and 45 % for horizontal wind speeds and directions at 80 and 100 m.

3.1.2 Meteorological tower

Quality control filtering methods performed on the met tower data discard data that are flagged for a number of reasons, including irregular timing (the time between measurements is inconsistent), insufficient percentage of data points within an averaging period (less than 95 %), low standard deviation (less than 0.01 % of the mean) or constant values during the measurement interval (which indicate icing events), empty data channels, bad values as defined by manufacturer limits, or when an instrument records a "NaN" in place of a real measurement. After filtering for quality control purposes, the met tower provides horizontal wind speeds and directions and temperatures about 90 % of the time at all levels during this study.

Several spikes in wind speed occur in the raw sonic anemometer data. Therefore, a de-spiking filter is applied based on the change in wind speed from each data point to the next. Data points are removed if they are preceded and followed by changes exceeding the lowest 99 % of all changes. After filtering the spikes in the sonic anemometers as well as the previously

discussed quality control procedure, the sonic anemometers provide wind speed and temperature about 90 % of the time at 15 m and about 60 % at 74 m during this study.

3.2 Wind speed and direction subselection

Although the dominant wind direction at the site is west-northwesterly, other wind directions do occur. To ensure the lidar and met tower measurements are upwind of the turbine, we consider only data from time periods of hub-height wind from the 235°–315° wind direction sector. This sector includes the most frequent and highest wind speeds as measured by both upwind instruments (Fig. 4). Only wind speeds between cut-in (3.5 m s^{-1}) and cut-out (25 m s^{-1}) are considered to ensure that the turbine is operating.

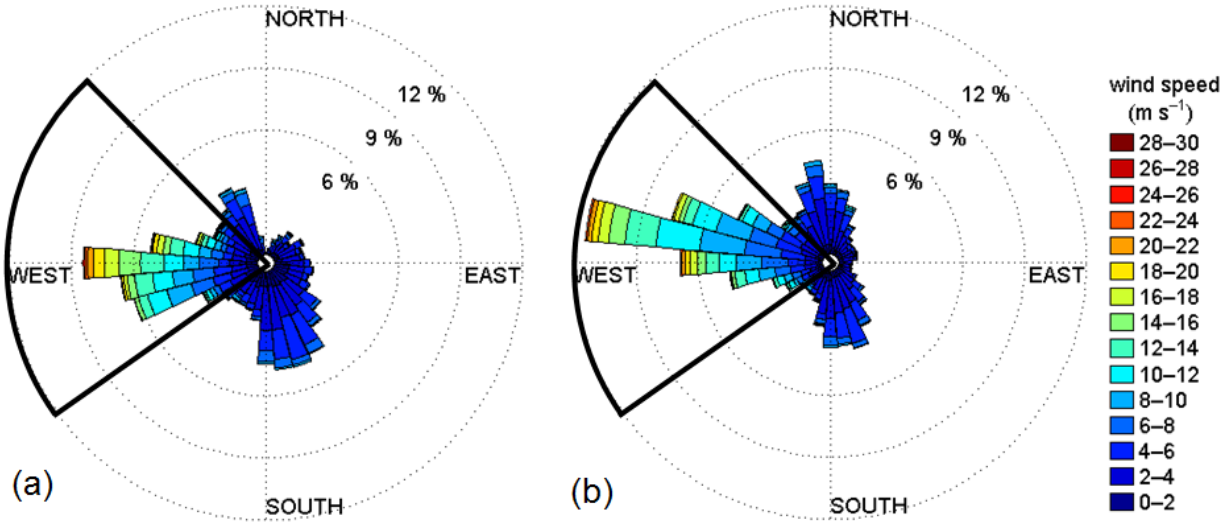

Figure 4. Wind roses for (a) lidar 80-m altitude and (b) met tower 87-m altitude, the closest to hub-height with both a cup and vane. Wind speed bins are 2 m s^{-1} and wind directions bins are 10°. The black outline highlights the chosen wind direction sector.

3.3 Filtering turbine underperformance

After filtering for quality control as well as wind speed and direction, a large number of times occur when the turbine is producing significantly less power than expected—

underperforming—as seen in Fig. 5a. We test two methods to isolate and discard the cases where the turbine is producing significantly lower power, inconsistent with "normal operation." The first approach relies on blade pitch angle to segregate data and flag most of these underperforming periods; this approach could be used by wind plant owner-operators with access to limited SCADA parameters. When more SCADA parameters are available, such as generator speed set point, these values may be used in a more rigorous way to filter on curtailment and to define normal turbine operation.

3.3.1 Filtering based on blade pitch angle

Without access to the turbine control system or data more refined than 10-min averages, typical blade pitch angles can be quantified as a function of wind speed (Fig. 5b). The median value for blade pitch angle for each wind speed bin as well as $\pm$ 4.5 median absolute deviation (MAD), equivalent to 3 σ, are shown by the red envelope in Fig. 5b. (We use MAD here instead of mean absolute deviation so that the calculation is not biased by a few outliers.) When plotted on a power curve using the tower 80-m cup anemometer for wind speed, Fig. 5a, the majority of the points outside of the $\pm$ 4.5 MAD envelope and between 5 and 17 m s^{-1} show underperformance. To identify underperformance, then, we calculate MAD blade pitch angles from each blade for each wind speed bin between 5 and 17 m s^{-1}. Time periods with blade pitch angles outside of $\pm$ 4.5 MAD are discarded. While variability on timescales shorter than 10 min may affect turbine operation, the effective filtering seen in the red scatter in Fig. 5a suggests that this approach is sufficient. This filtering by blade pitch angle also has the advantage of using only data to which a typical wind plant operator would have access.

After filtering for hub-height wind speed and direction, positive power production, and blade pitch angle, 1,240 out of 7,949 lidar 80-m wind speed data points remain (16 %), and 2,235

out of 9,918 met tower 80-m wind speed data points remain (23 %). Concurrent lidar, met tower, and turbine data that fulfill the various screening criteria occur during 1,107 10-min periods.

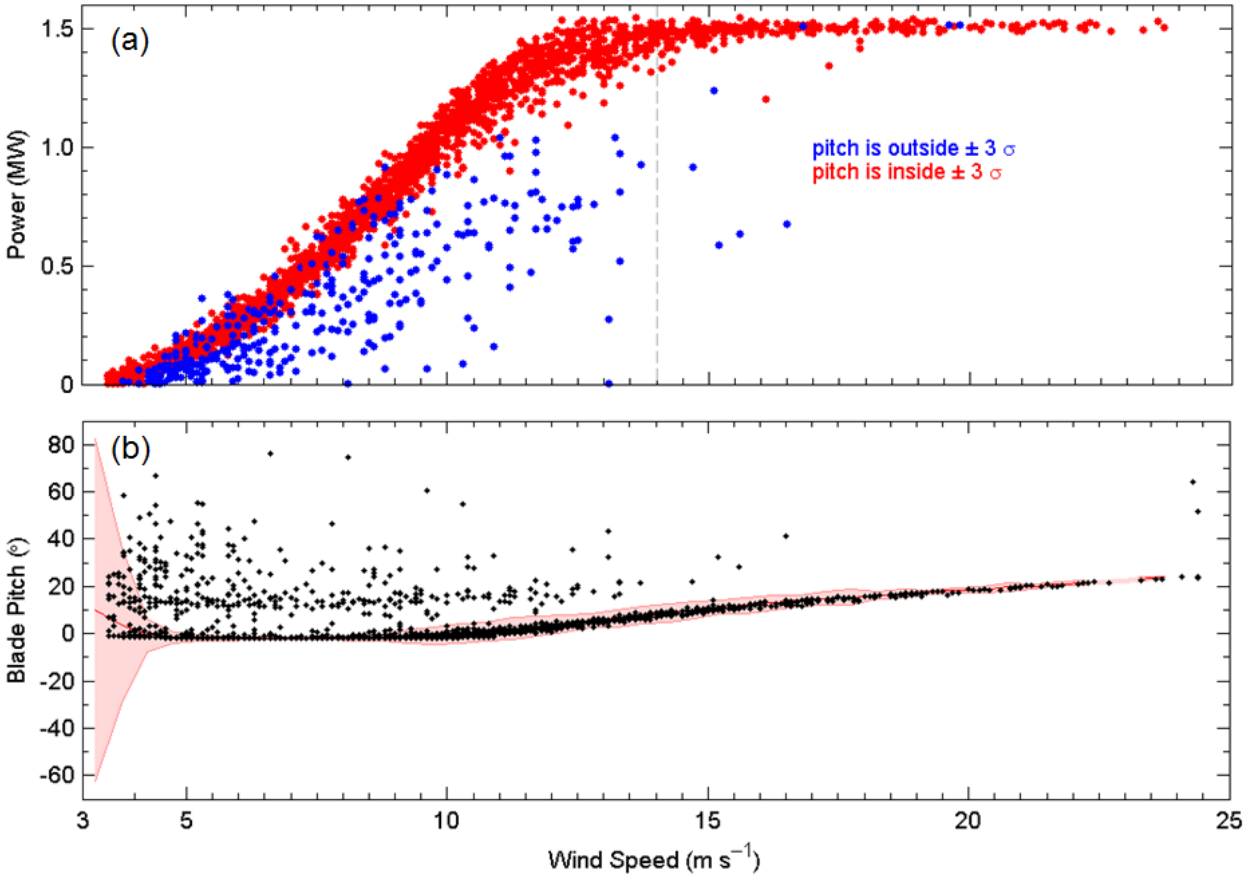

Figure 5. (a) Scatter power curve based on the tower 80-m wind speed. Blue dots show points that are outside of the median absolute deviation (MAD) envelope in (b) and the red dots represent points that are within the MAD envelope in (b). The vertical grey dashed line marks rated speed; (b) blade pitch angle from a single blade versus tower 80-m wind speed. Red envelope represents $\pm$ 4.5 MAD of the blade pitch angle within wind speed bins 0.5 m s^{-1} wide.

3.3.2 Filtering based on extensive SCADA turbine operational parameters

Access to a number of turbine control parameters from the SCADA on the DOE GE 1.5 allows for a more accurate definition of normal turbine operation, mostly based on generator speed set point filtered on curtailment. However, from cut-in wind speed until around 5.5 m s^{-1},

using generator speed set point to filter the data results in discarding too many data points. Therefore, between cut-in wind speed and about 5.5 m s^{-1}, the generator speed set point is not used; rather data points are discarded only when the turbine is not grid connected and is faulted. Above 5.5 m s^{-1}, only generator speed set point is used to filter on curtailment and for normal operation. The data points filtered using this method are represented in Fig. 6 in blue, while the red points in Fig. 6 represent the data points that pass this filtering method.

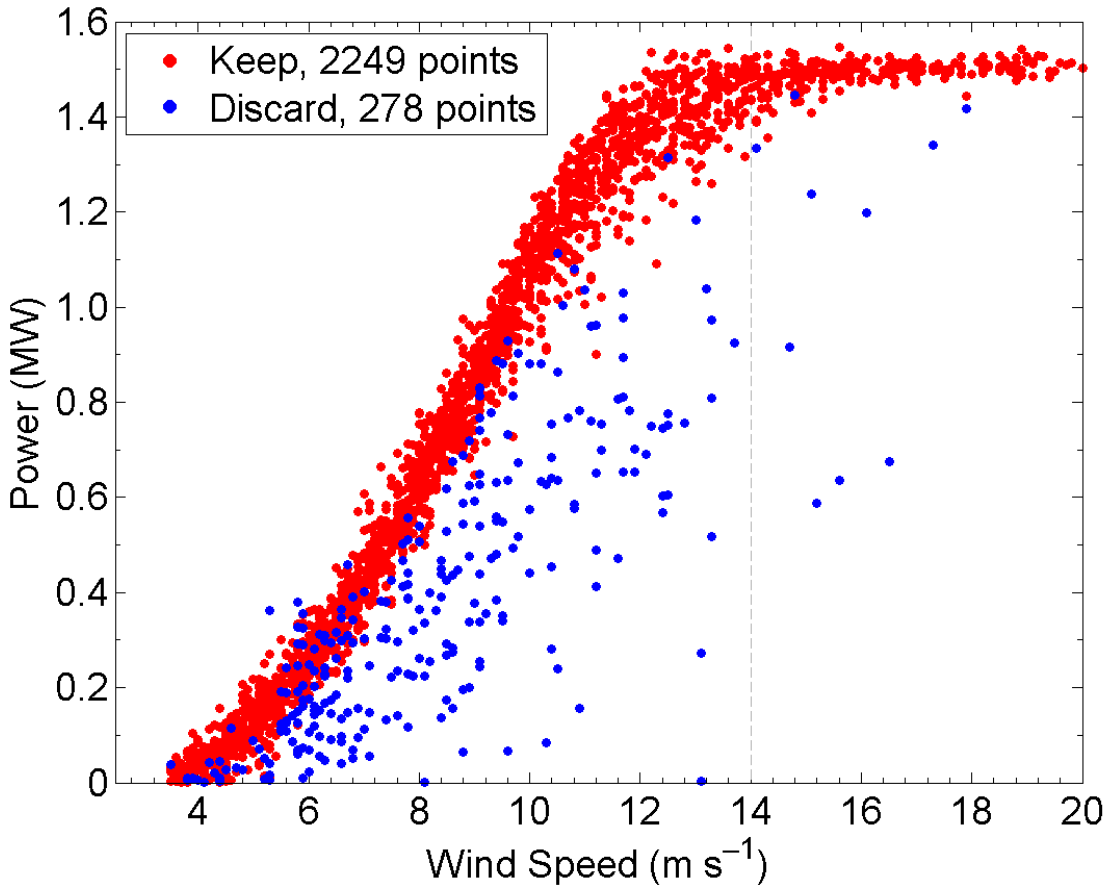

Figure 6. Scatter power curve using the tower 80-m wind speed. Blue dots show points filtered out using turbine control parameters described in Sect. 3.3.2. Red dots show data points that passed this filtering process. The grey dashed line marks rated speed.

After filtering for hub-height wind speed and direction, positive power production, and normal turbine operation, 1,227 out of 7,949 lidar 80-m wind speed data points remain (15 %), and 2,249 out of 9,918 met tower 80-m wind speed data points remain (23 %). Concurrent lidar, met tower, and turbine data that fulfill the various screening criteria occur during 1,127 10-min periods.

3.3.3 Comparison of different turbine operation filters

The turbine operation filters described in Sect. 3.3.2 not only filter out all of the times when the turbine is producing significantly less power than expected, but allows the use of about 2 % more data points deemed "bad" by the blade pitch angle filtering method described in Sect. 3.3.1. Many of the data points that would be discarded using the blade pitch angle filtering method are between cut-in wind speed and 10 m s^{-1}, and lie reasonably within the expected power curve, on top of data points that passed through the filter. Therefore, the remaining analysis is based on data filtered using the methodology described in Sect. 3.3.2.

3.4 Power curves

Power curves based on wind speeds normalized by air density following International Electrotechnical Commission (IEC) 61400-12-1 (2015) can be used to evaluate turbine performance. The observed power curves, comparing power production to 80-m tower anemometer wind speeds (Fig. 7a), 80-m lidar wind speeds (Fig. 7b), and nacelle anemometer wind speeds (Fig. 7c), generally show good agreement with an approximation of the MPC (GE Energy 2009). This approximated MPC is determined by placing the publicly-available MPC for the GE 1.5sle on a grid (with dimensions of 0.5 m s^{-1} by 50 kW) and estimating expected power produced at each wind bin.

The nacelle-mounted anemometer does not observe the ambient wind speed that the rotor disk experiences because the wind that flows through the rotor disk and along the nacelle during operation is modified by the blades and nacelle (Antoniou and Pedersen 1997; Smith et al. 2002; Frandsen et al. 2009; Zahle and Sørensen 2011). However, power curves calculated using nacelle wind speeds are shown here along with power curves calculated using upwind measurements in order to compare the different methods. In many cases, operators calculate these nacelle-based power curves due to lack of other data.

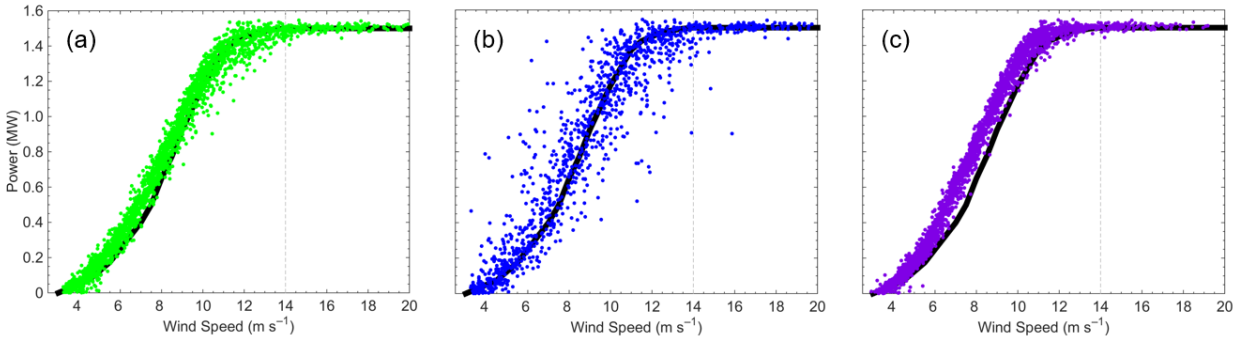

Figure 7. Power curves after filtering for wind speeds between 3.5 and 25 m s^{-1}, wind directions between 235°and 315°, and for normal turbine operation: (a) turbine power production versus 80-m cup anemometer wind speed from the met tower; (b) turbine power production versus 80-m wind speed from the lidar; (c) turbine power production versus hub-height wind speed from the anemometer on the nacelle. The black line represents an approximation of the manufacturer power curve for the GE 1.5sle (GE Energy, 2009). Wind speed is normalized for density following IEC 61400-12-1 (2015). The grey dashed line marks rated speed.

The power curves created from 10-min tower and nacelle-mounted anemometer measurements (Fig. 7a, Fig. 7c, respectively) show less variability than the lidar power curve (Fig. 7b). It is especially apparent from the power curve created from 10-min lidar measurements (Fig. 7b) that the lidar variability at this particular site is vulnerable to inhomogeneity in the flow. Although lidars are widely available and used in the field (Clifton, 2015), the variability between the lidar and tower measurements (Fig. 8) indicates sufficient inhomogeneity in the flow at this particular site (as observed by Aitken et al., 2014b) to cause us to discuss and show other

upwind data from the tower from this point forward. Note, however, that not all sites are subject to the inhomogeneity seen at the NWTC, and all instruments available for wind measurement should be considered. Concurrent met tower and turbine data that fulfill the screening criteria occurred during 2,240 10-min periods, equivalent to about 373 h of data, which is more than twice the 180 h of data that the IEC 61400-12-1 standard (2015) recommends for power performance testing.

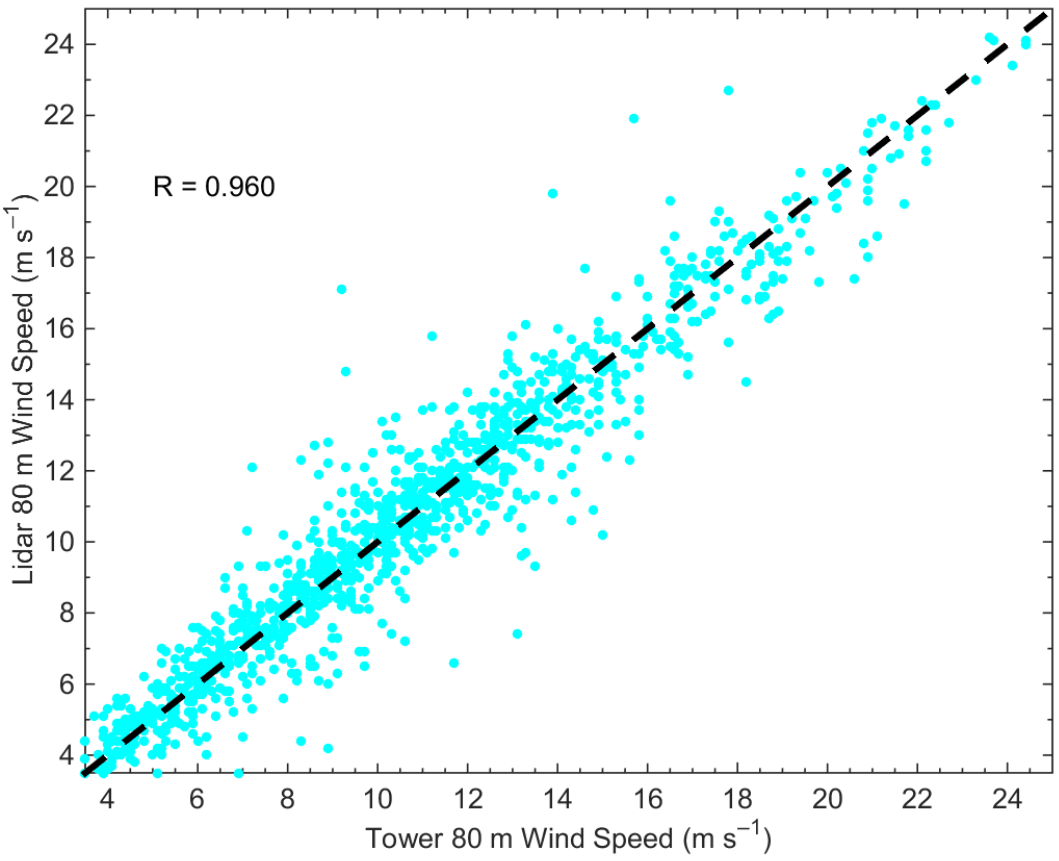

Figure 8. Lidar 80-m wind speeds compared to tower 80-m wind speeds filtered for wind speeds between 3.5 and 25.0 m s^{-1}, wind directions between 235° and 315°, and for normal turbine operation. Black dashed line represents a 1:1 relationship**.**

3.5 Atmospheric stability regimes

Numerous approaches are available for classifying the atmospheric stability of a given 10-min or 30-min time period. Bulk Richardson number (R_B) calculations use temperature and wind speed differences from the lowest met tower measurement to the height of the top of the rotor disk to compare the buoyant production of turbulence to the wind-shear-generated mechanical production of turbulence (Stull, 1988) as

$$R_B = \frac{g\,\Delta T\,\Delta z}{\bar{T}\,\Delta U^2}\ , \tag{1}$$

where g is the gravitational constant 9.81 m s^{-2}, Δz is the change in height, ΔT is the change in 10-min averages of temperature across Δz, $\bar{T}$ is the mean temperature across Δz, and ΔU is the change in the 10-min averages of horizontal wind speed across Δz. Note that Eq. (1) does not consider wind direction variability because cup anemometer measurements provide only information about horizontal wind speed. Typical stability classifications based on R_B calculations are as follows: turbulent flow in unstable conditions when R_B is less than 0, laminar flow in stable conditions when R_B is greater than 0.25, and neutral conditions when R_B is between 0 and 0.25 (Stull, 1988). These stability classifications are similar to those used in previous work on stability effects on wind turbine fatigue and loading in Kelley (2011), and slightly different from the stability classifications used in Vanderwende and Lundquist (2012). The distribution of R_B calculated from the tower measurements for this campaign (Fig. 9), however, suggests that slightly different regimes, shown in Table 2, could be used to better represent the data at this site. Similar to the approach used in Aitken et al. (2014b), the R_B distribution is split roughly into thirds to allow for less overlap between stable and unstable

regimes. The uncertainty in R_B for these instruments over the measurement period is about 0.01, therefore the R_B classifications used are larger than the uncertainty.

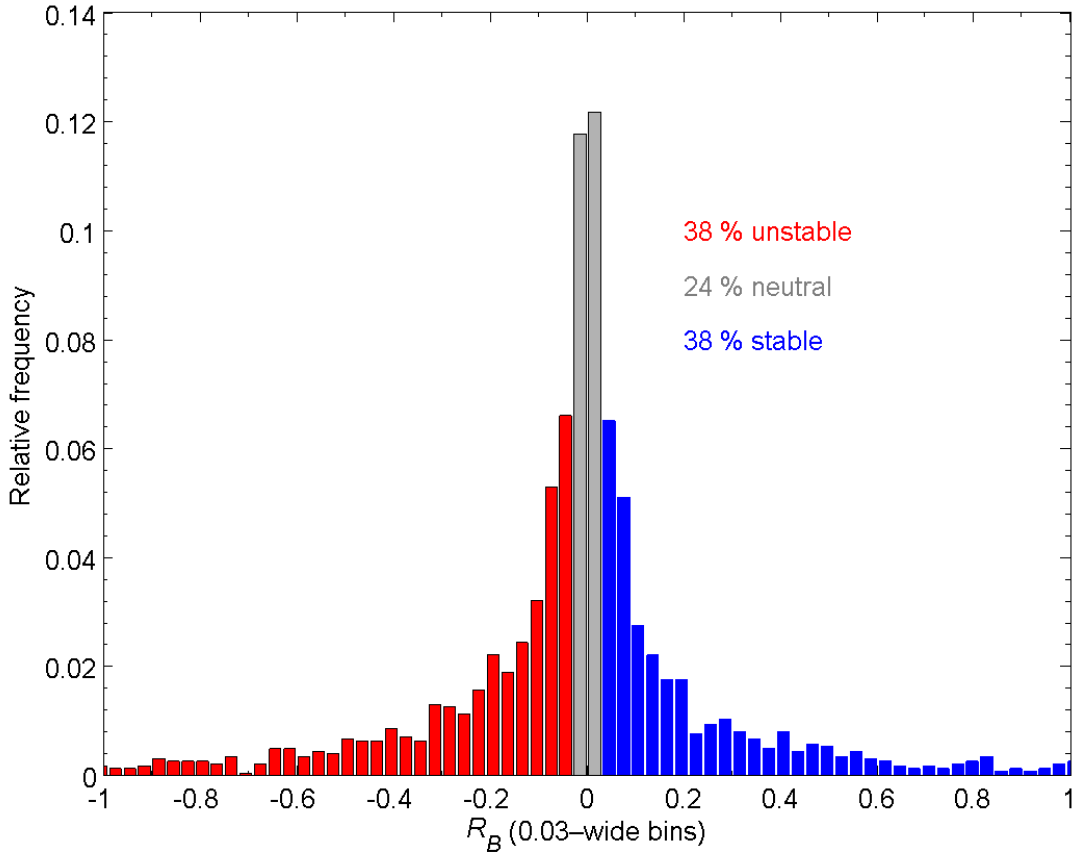

Figure 9. R_B distribution using thresholds in Table 2, including data filtered for tower 80-m wind speeds between 3.5 and 25.0 m s^{-1}, 87-m wind directions between 235° and 315°, and for normal turbine operation.

Obukhov length *(L)* is also a useful measure of atmospheric stability, relying on surface stresses as well as heat fluxes to estimate the height in the surface layer at which the buoyant production of turbulence dominates wind-shear-generated mechanical production of turbulence (Stull, 1988) as

$$L = -\frac{{u_*}^3}{k\,g}\,\frac{T_v}{\overline{w'T_s'}} \quad , \tag{2}$$

where u_* is the friction velocity, *k* is the von Karman constant 0.41, T_v is the virtual temperature, w' is the vertical wind speed fluctuation in the 30-min averaging period, and ${T_s}'$ is the sonic temperature fluctuation in the 30-min averaging period. *L* calculations are based on sonic anemometer measurements at 15 m and temperature measurements interpolated to 15 m to ensure *L* is calculated using measurements within the surface layer. Typical stability classifications are used in this work and are based on *L* calculations as defined by Muñoz-Esparza et al. (2012); shown in Table 2. These classifications are slightly different from those used in Wharton and Lundquist (2012b). The distributions of *L* are shown in Fig. 10.

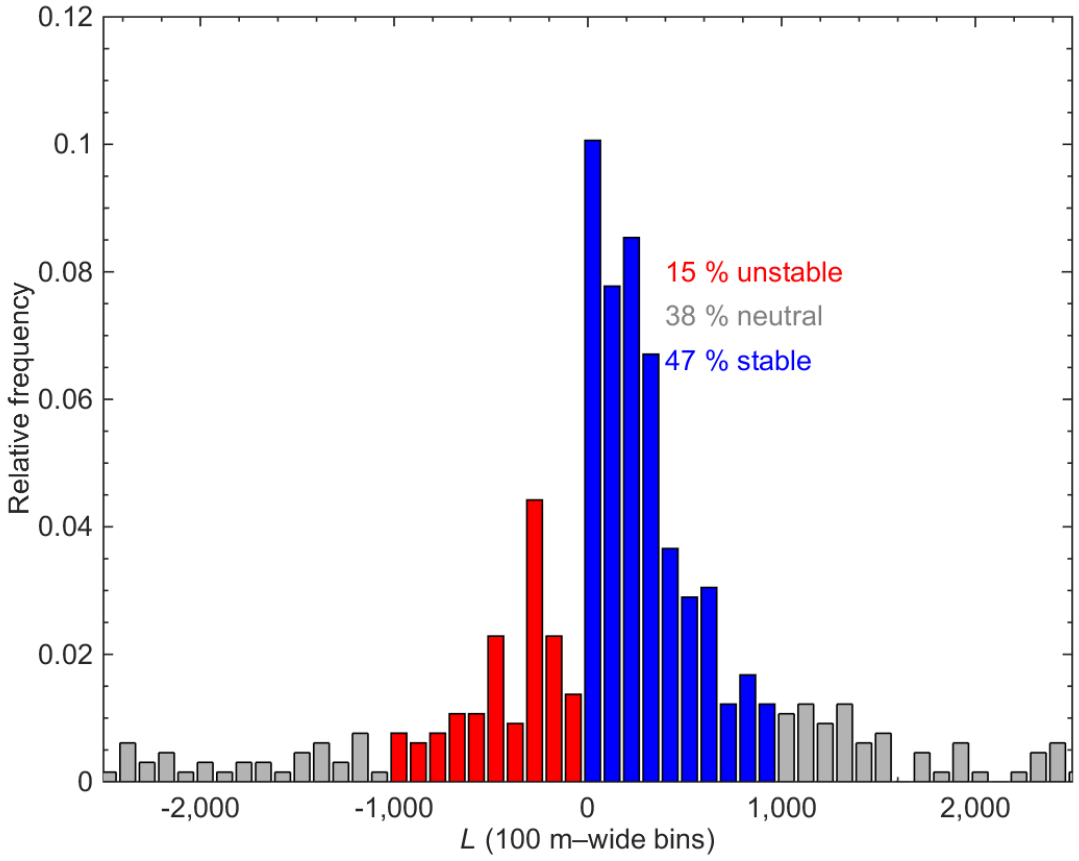

Figure 10. *L* distribution using thresholds in Table 2. Note that some neutral cases are outside of these axes. Includes data filtered for tower 80-m wind speeds between 3.5 and 25.0 m s^{-1}, 87-m wind directions between 235° and 315°, and for normal turbine operation.

Table 2. Defined stability regimes

Stability class	R_B	L **(m)**	α
Unstable conditions	$R_B < -0.03$	$-1{,}000 < L \leq 0$	$\alpha < 0.11$
Neutral conditions	$-0.03 < R_B < 0.03$	$\lvert L \rvert \geq 1{,}000$	$0.11 < \alpha < 0.17$
Stable conditions	$R_B > 0.03$	$0 \leq L < 1{,}000$	$\alpha > 0.17$

When the R_B and L stability approaches are compared against one another and against time-of-day, as in Fig. 11, the stability parameters differ slightly in their definitions of unstable

and stable. Because of differences in stability classes due to varying approaches to defining atmospheric stability, we treat R_B-defined stability classes separately from L-defined stability classes in the power curves.

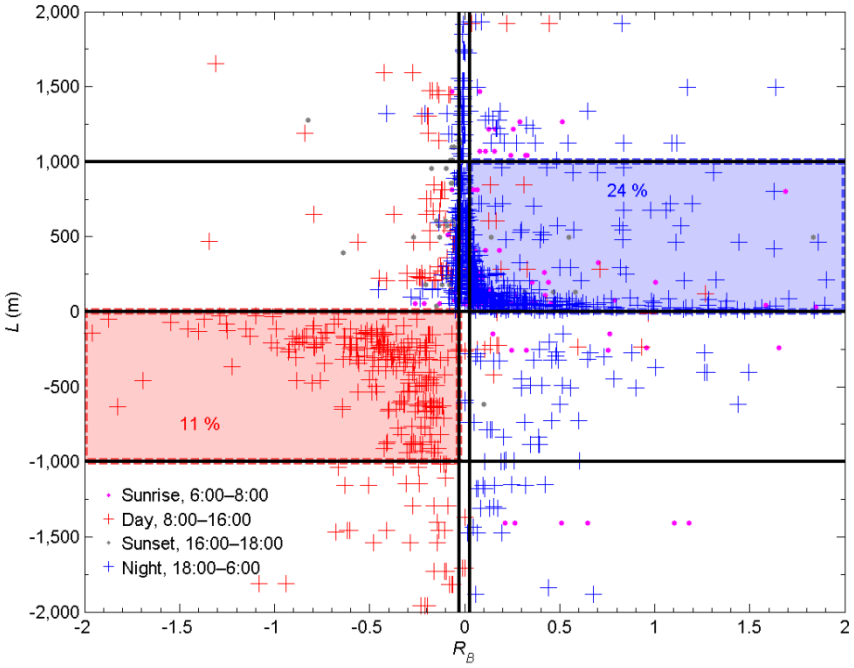

Figure 11. L versus R_B. Blue box represents where both L and R_B agree on the stable conditions; percentage (24 %) represents the percentage of data points in this box. Red box represents where both L and R_B agree on the unstable conditions; percentage (11 %) represents the percentage of data points in this box. Includes data filtered for tower 80-m wind speeds between 3.5 and 25 m s^{-1}, 87-m wind directions between 235° and 315°, and for normal turbine operation.

3.6 Turbulence regimes

TI can also be used to describe atmospheric conditions, as demonstrated by Rareshide et al. (2009), Wagenaar and Eecen (2011), and Wharton and Lundquist (2012a). TI is typically defined as

$$TI = \frac{\sigma_{80m}}{U_{80m}} * 100 \,, \tag{3}$$

where σ_{80m} is the 10-min standard deviation of the horizontal wind speed at 80 m and U_{80m} is the 10-min mean horizontal wind speed at 80 m. Although the TI approach has been used successfully at other locations, the NWTC consistently features strong turbulence likely resulting from the terrain characteristics of the site (Fig. 12, Fig. 13), making it difficult to distinguish typical stability classes from TI calculations. This strong ambient turbulence has led to the choice of site-specific turbulence classification defined in Table 3.

When the atmospheric stability regimes are compared to the TI regimes defined here (Fig. 14), the R_B and TI regime percentages also differ slightly in their definitions of unstable atmospheric conditions and highly turbulent conditions. Most of the daytime points are within the unstable regime as defined by R_B; however, only about 17 % of the data fall within unstable conditions with higher TI. This comparison, again, emphasizes the highly turbulent characteristics of the NWTC.

To further understand the turbulence characteristics demonstrated during this campaign, we also calculate TKE using the 74-m 3D sonic anemometer mounted on the M5 met tower. Although TI is a parameter typically calculated and analyzed in the wind industry, TKE has the advantage of including the vertical component of the wind:

$$TKE = \frac{1}{2}\left(\overline{u'^2} + \overline{v'^2} + \overline{w'^2}\right) \ , \tag{4}$$

where we calculate TKE per unit mass, *u'* is the perturbation from a 30-min average of the zonal component of the wind, *v'* is the perturbation from a 30-min average of the meridional component of the wind, and *w'* is the perturbation from a 30-min average of the vertical component of the wind. Using this TKE approach also reveals the strong turbulence at the NWTC, only slightly affected by the diurnal cycle during this wintertime campaign (Fig. 12, Fig.

15). Turbulence classifications based on TKE are determined by the distribution in Fig. 15 and are listed in Table 3.

Many cases with relatively high TI or TKE are considered neutral and stable according to our stability definitions in Table 3. Depending on whether TI, TKE, R_B, or L is considered as a measure of atmospheric stability, a particular time period may be classified differently. In other words, different results are found depending on the metric selected.

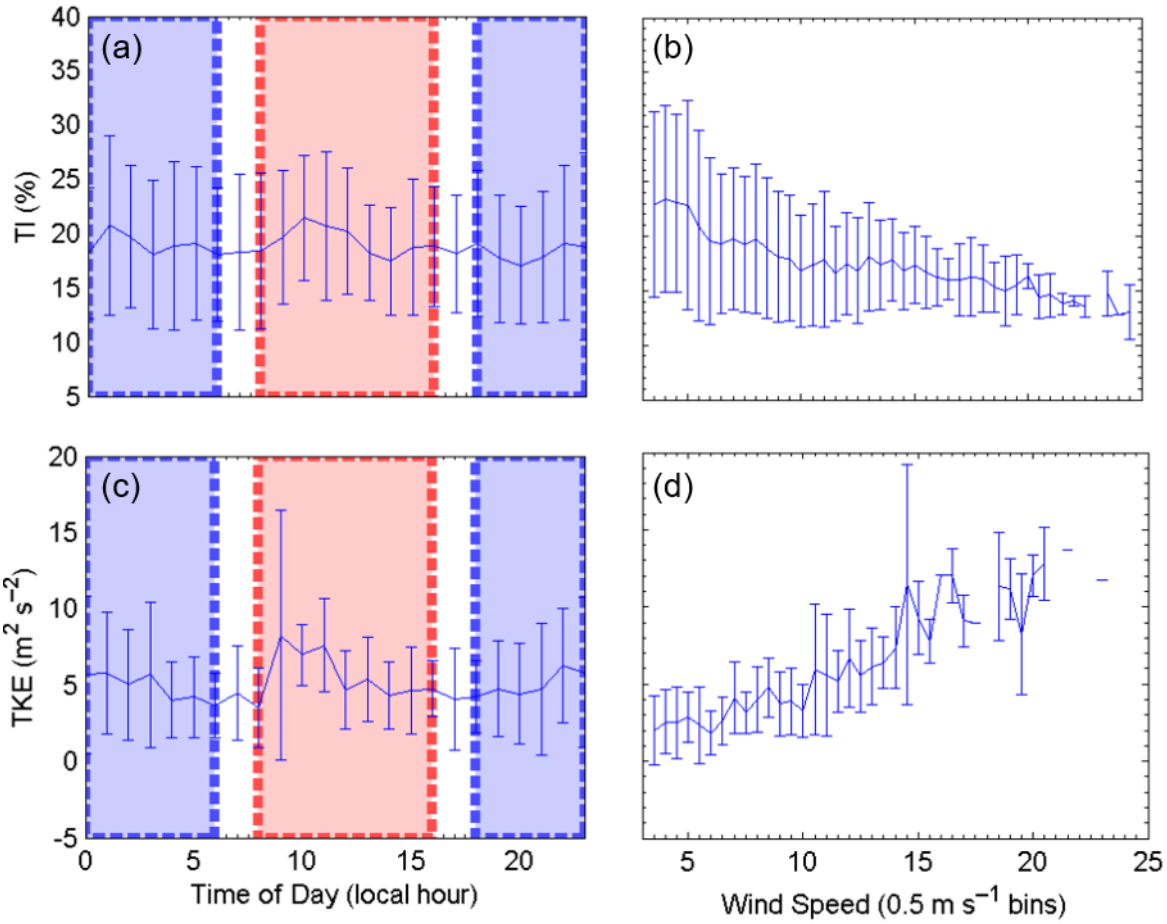

Figure 12. TI (a) and TKE (c) calculated with near hub-height tower measurements versus time of day, where hour 0 and hour 24 represent local midnight. The blue line represents the mean TI in the corresponding hour and the error bar represents the standard deviation. The blue rectangle represents nighttime hours and the red rectangle represents daytime hours. Mean and standard deviation of TI (b) and TKE (d) calculated with near hub-height tower measurements in each wind speed bin. Includes data filtered for tower 80-m wind speeds between 3.5 and 25.0 m s^{-1}, 87-m wind directions between 235° and 315°, and for normal turbine operation.

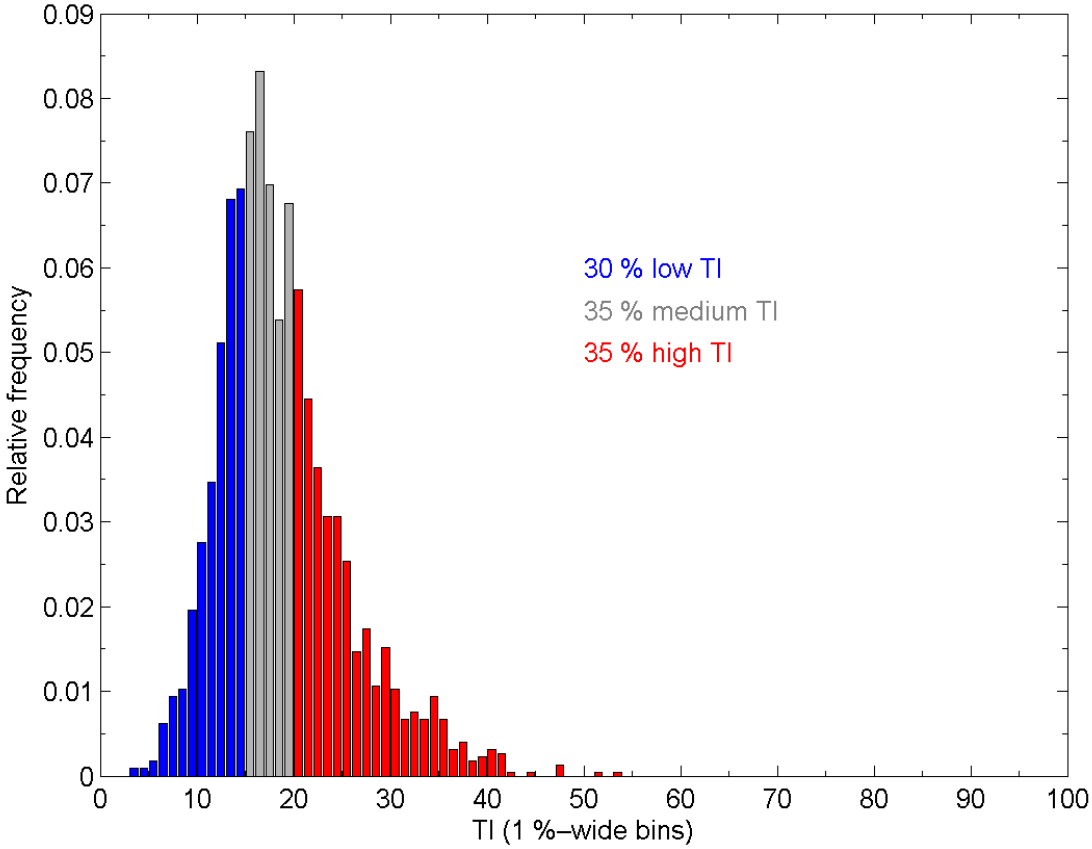

Figure 13. TI distribution using thresholds in Table 3. Includes data filtered for tower 80-m wind speeds between 3.5 and 25 m s^{-1}, 87-m wind directions between 235° and 315°, and for normal turbine operation.

Table 3. Defined turbulence regimes

Turbulence regime	**TI (%)**	**TKE (m^2 s^{-2})**
High turbulence	TI > 20	TKE > 6.5
Medium turbulence	15 < TI < 20	3.0 < TKE < 6.5
Low turbulence	TI < 15	TKE < 3.0

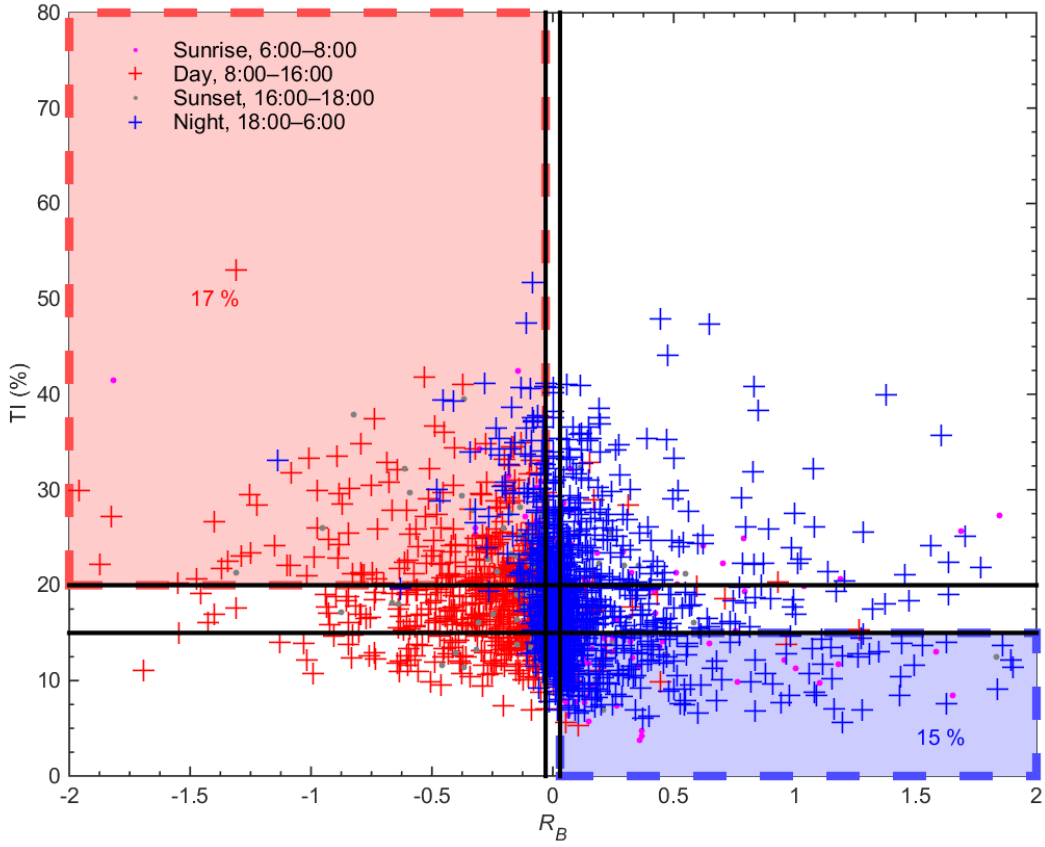

Figure 14. TI versus R_B . Blue box represents where both TI and R_B agree on the stable conditions; percentage (15 %) represents the percentage of data points in this box. Red box represents where both TI and R_B agree on the unstable conditions; percentage (17 %) represents the percentage of data points in this box. Includes data filtered for tower 80-m wind speeds between 3.5 and 25 m s^{-1}, 87-m wind directions between 235° and 315°, and for normal turbine operation.

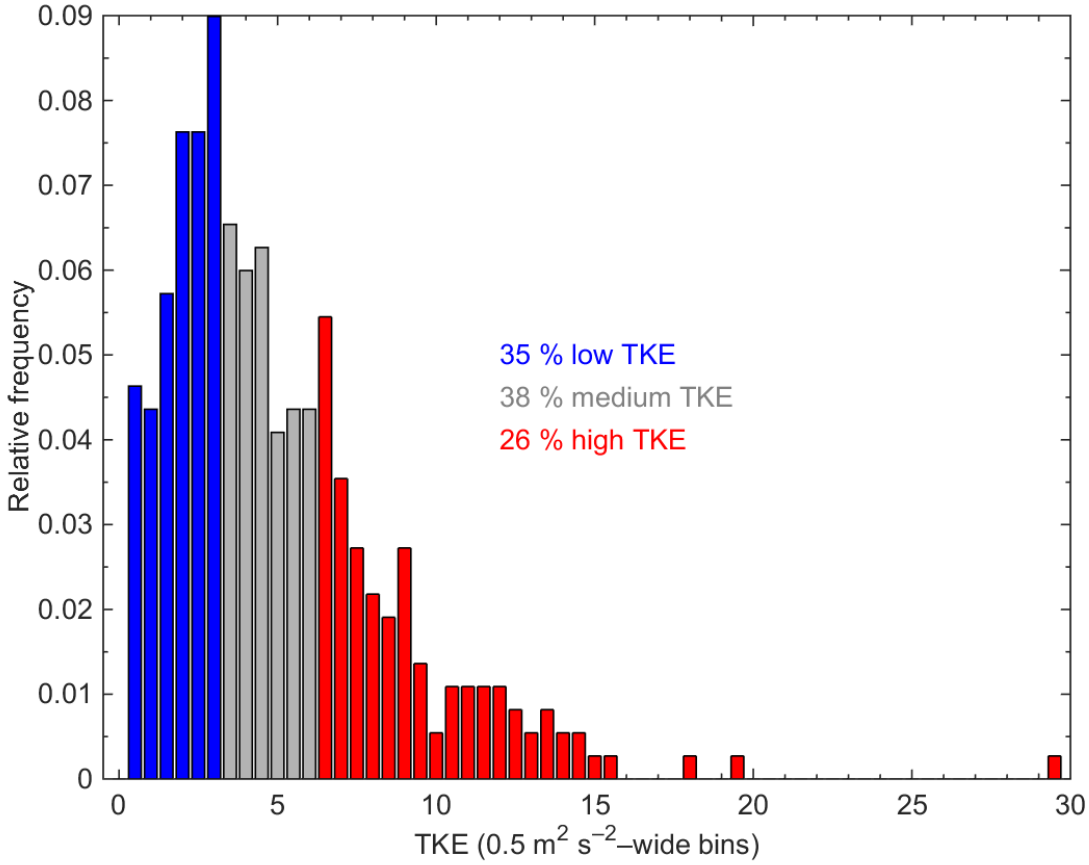

Figure 15. TKE distribution using thresholds in Table 3. Includes data filtered for tower 80-m wind speeds between 3.5 and 25.0 m s^{-1}, 87-m wind directions between 235° and 315°, and for normal turbine operation.

3.7 Wind shear regimes

To estimate the effect of the wind speed vertical profile across the rotor disk, the wind shear exponent or power law exponent parameter, α, is typically used in the wind energy industry:

$$\alpha = \frac{\log\left(\frac{U_2}{U_1}\right)}{\log\left(\frac{z_2}{z_1}\right)}, \quad (5)$$

where z_1 is the reference height, z_2 is the height above ground level, U_2 is the wind speed at height z_2, and $U_1$is the wind speed at height z_1. At the NWTC during this study, the average wind shear exponent using the 122 m and 38 m tower wind speeds as z_2 and z_1, respectively, is 0.15. The standard deviation is 0.14 and the maximum wind shear exponent is 1.10.

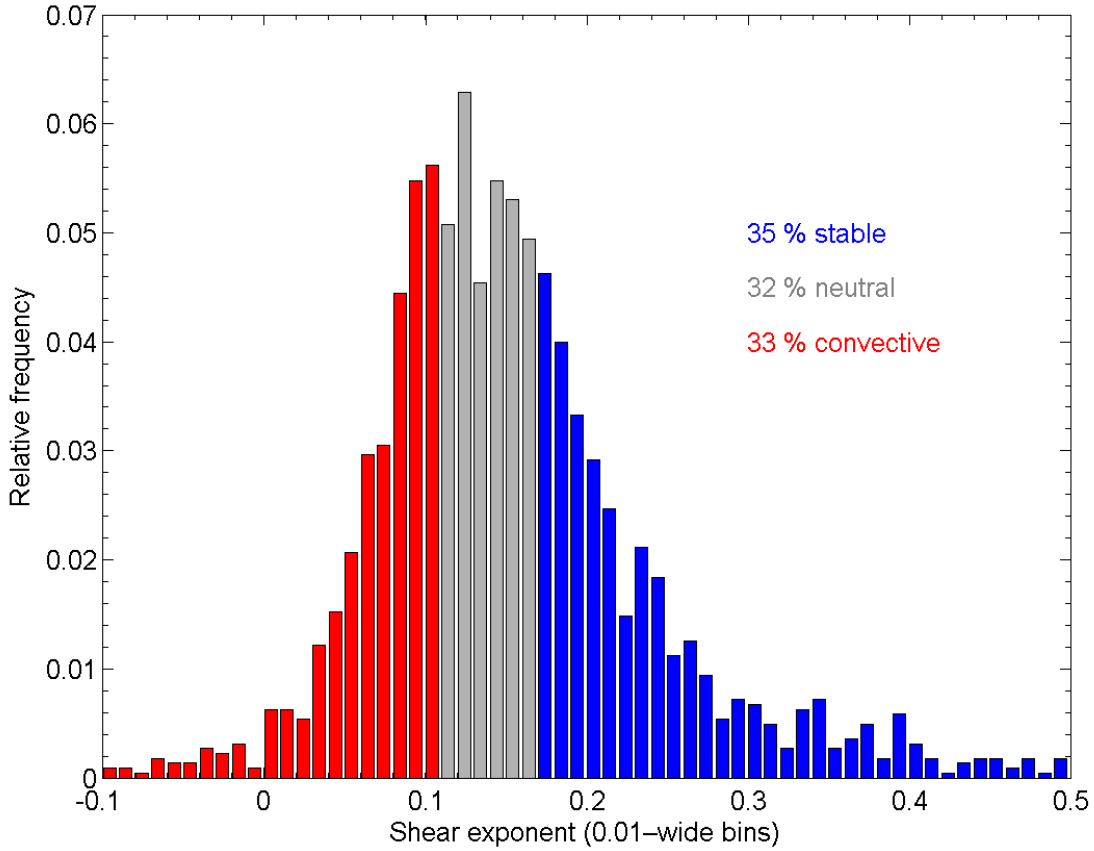

Figure 16. Shear exponent distribution using thresholds in Table 2. Includes data filtered for tower 80-m wind speeds between 3.5 and 25.0 m s^{-1}, 87-m wind directions between 235° and 315°, and for normal turbine operation.

For this period of time at this site, however, it was rare for the rotor equivalent wind speed (REWS) to deviate significantly from the hub-height wind speed (Sect. S2). Therefore, shear exponents are separated into regimes simply by splitting the shear exponent distribution

into thirds (Table 2, Fig, 16). Other approaches to classify stability regimes using shear exponents such as combining with other stability measures such as L and R_B, (Vanderwende and Lundquist, 2012) or using a REWS in the power curves (Elliott and Cadogan, 1990), may work at other sites.

4 Results

To explore the variability in the power curves, we apply filters to the power curves based on factors such as atmospheric stability and TI. We apply a new method to calculate AEP using these classifications. We can consider periods with low TI to be approximately "stable" by R_B and L; "unstable" conditions would generally have high TI. Our results show that, generally, at this site with little veer, stable conditions (with varying degrees of significance) lead to over-performance at wind speeds just below rated power. At lower wind speeds, however, unstable conditions lead to over-performance.

4.1 Power curves

The NWTC site generally exhibits high TI throughout this data collection period. Even so, some differences in power produced emerge at wind speeds between 5 and 7 m s^{-1} and at wind speeds between 10 and 14 m s^{-1} after separating the TI into relative classes of low, medium, and high TI (Fig. 17a, Fig. 17c, Fig. 18a, Fig. 18c, Table 3). Statistically-distinct differences within each wind speed bin between the TI classes defined in Table 3 are determined by the Wilcoxon rank sum test with a 1 % significance level. These statistically-distinct bins are denoted by closed circles in Fig. 17a, Fig. 17c, Fig. 18a, and Fig. 18c. This statistical test shows that for the power curves using nacelle winds, periods of relatively high TI produce significantly more power than periods of relatively low TI at wind speeds between 5 and 9 m s^{-1} (Fig. 17a,

Fig. 18a). For the power curves using upwind tower winds, periods of relatively high TI produce significantly more power than periods of relatively low TI at wind speeds between 6.0 and 6.5 m s^{-1} (Fig. 17c, Fig. 18c). Conversely, power curves using nacelle winds show that at wind speeds between 10.5 and 13.5 m s^{-1}, periods of relatively low TI produce significantly more power than periods of relatively high TI. Power curves using upwind tower winds show that at wind speeds between 9.5 and 15.5 m s^{-1}, periods of relatively low TI produce significantly more power than periods of relatively high TI. Rareshide et al. (2009) found similar behavior.

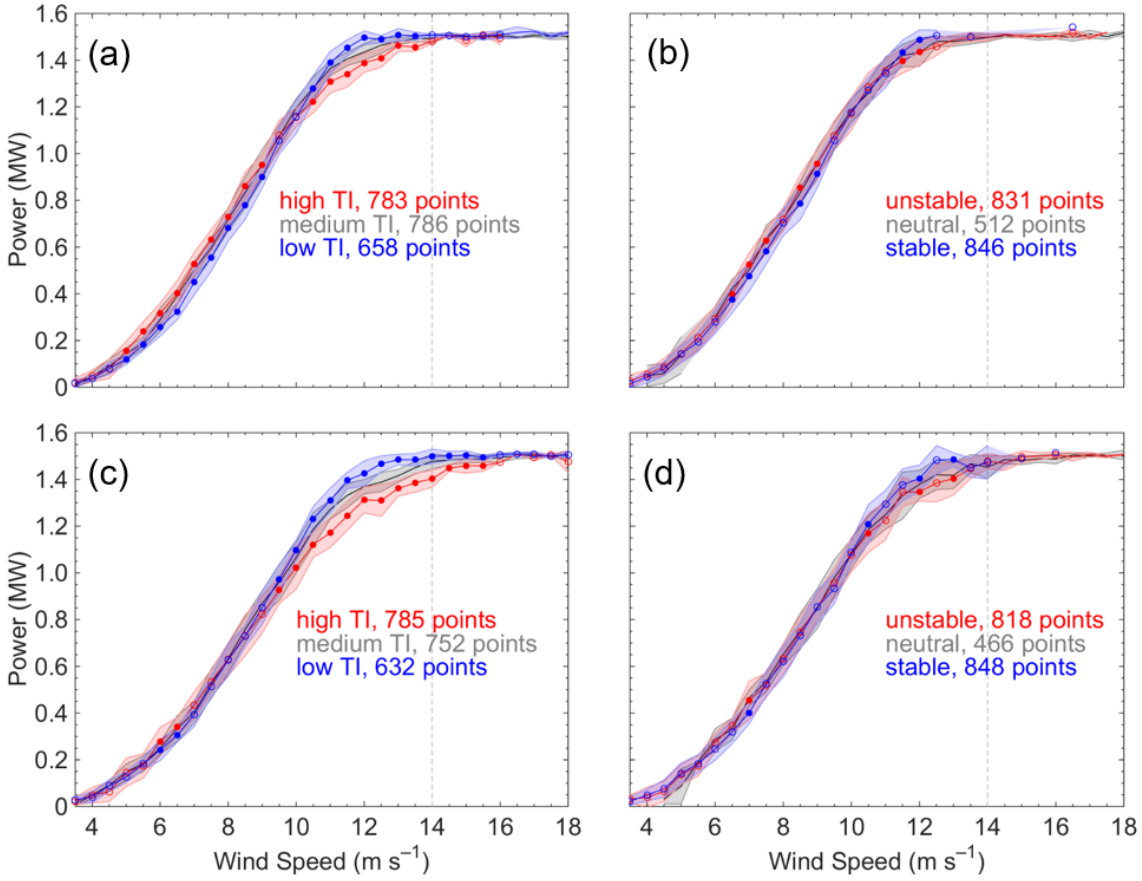

Figure 17. Nacelle anemometer power curves with (a) TI regimes and (b) R_B regimes. Eighty-meter tower anemometer power curves with (c) TI regimes and (d) R_B regimes. Median statistics are used to avoid outlier effects. Statistically distinct differences within each wind speed bin between the regimes are determined by the Wilcoxon rank sum test with a 1 % significance level and denoted by closed circles. Includes data filtered for tower 80-m wind speeds between 3.5 and 25.0 m s^{-1}, 87-m wind directions between 235° and 315°, and for normal turbine operation. Envelopes represent ± 1 MAD for each wind speed bin. The grey dashed line marks rated speed.

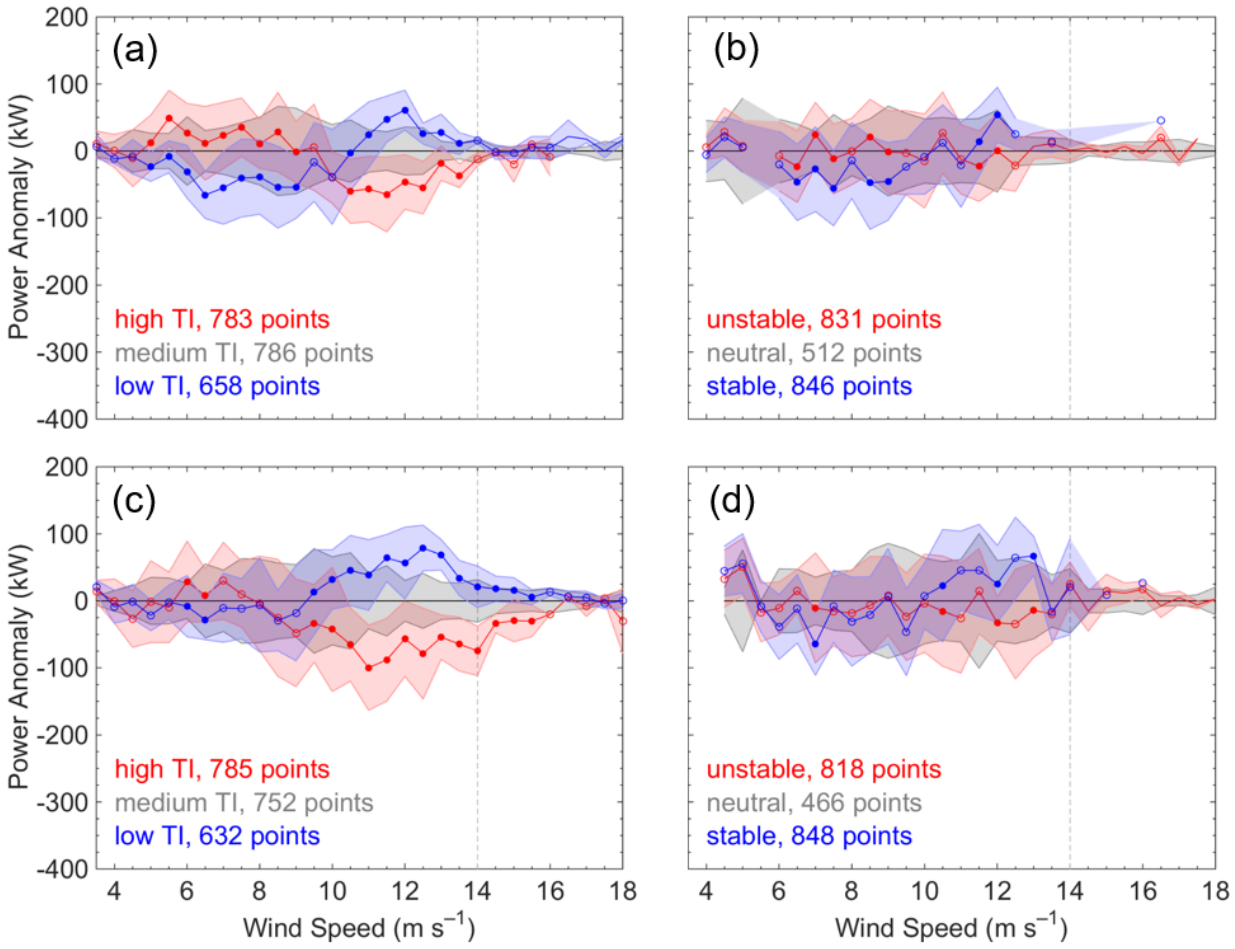

Figure 18. Nacelle anemometer power curves shown as the anomaly from the neutral or medium power curve of the (a) TI regimes and (b) R_B regimes. Eighty-meter tower anemometer power curves shown as the anomaly from the neutral or medium power curve of the (c) TI regimes; (d) R_B regimes. Median statistics are used to avoid outlier effects. Statistically distinct differences within each wind speed bin between the regimes are determined by the Wilcoxon rank sum test with a 1 % significance level and denoted by closed circles. Includes data filtered for tower 80-m wind speeds between 3.5 and 25.0 m s^{-1}, 87-m wind directions between 235° and 315°, and for normal turbine operation. Envelopes represent ± 1 MAD for each wind speed bin. The grey dashed line marks rated speed.

On the other hand, power curves separated by R_B-defined stability class show only a few bins that are statistically distinct in power produced (Fig. 17b, Fig. 17d, Fig. 18b, Fig. 18d). Power curves using nacelle winds show that at most wind speeds between 6.5 and 9.0 m s^{-1}, periods of unstable conditions produce significantly more power than periods of stable

conditions. Power curves using upwind tower winds show that at wind speeds around 7 m s^{-1}, periods of unstable conditions produce significantly more power than periods of stable conditions. Power curves using both nacelle winds and tower winds show that at wind speeds around 12 m s^{-1}, periods of stable conditions produce significantly more power than periods of unstable conditions.

Distinct differences between power curves calculated from nacelle winds and power curves calculated from upwind tower winds occur in the power curves of both of these atmospheric parameters. Statistically distinct wind speed bins in power curves calculated from nacelle winds tend to be similar to those in power curves calculated from tower winds near rated speed. At lower wind speeds, however, between about 5 and 9 m s^{-1}, many more statistically distinct differences emerge between nacelle power curves than between tower power curves, most notably in the power curves segregated by TI regimes. Turbine operations are especially variable in this region of rapid increase in power with wind speed. The turbine reacts directly to the conditions as measured by instruments on the turbine. The nacelle-mounted anemometer observes winds that flow through the rotor disk and along the nacelle during turbine operation, and therefore likely measures different wind speeds than the upwind met tower. The nacelle anemometer observes complex flows behind the rotor disk that are strongly influenced by ambient turbulence, leading to more statistically significant differences in the nacelle power curves for TI regimes.

Agreement between the TI and R_B methods means that at wind speeds around rated, low TI and high stability result in over-performance relative to high TI and low stability. Both methods also agree that somewhere in between cut-in and rated, sometimes called “region 2,” high TI and low stability result in over-performance relative to low TI and high stability. Power

curves separated by *L*-defined stability class as well as power curves separated by shear class do not show any statistically-significant differences in power produced between unstable and stable periods (not shown). Power curves separated by TKE class show few statistically-significant differences in power produced between high and low TKE periods, likely because of the few data points available for the 30-min averaging period, therefore these results are shown in the supplement (Sect. S4).

4.1.1 Underlying physics

The large variability reported in the literature (and herein) regarding power production can be understood by recognizing the interactions between a pitch-controlled turbine and the atmosphere: the operation of control algorithms changes with wind speed, with varying effects depending on the ambient turbulence.

Sensitivity to atmospheric turbulence occurs at low wind speeds, near cut-in wind speed. In these conditions, the turbine generator speed (revolutions per minute, RPM) increases, as does the generator torque. As a result, the blades will often pitch backward, changing the angle of attack to generate more lift, and the power production ramps up. At low wind speeds and higher turbulence, the turbine can react to the higher variation in wind speed and can capitalize on the variation seen in the wind flow because of the additional lift resulting from the blade pitch, and the turbine produces more power. Conversely, at low wind speeds with lower turbulence, the variation in wind speed is lower, and so the turbine experiences more consistent wind than in highly turbulent conditions and therefore produces less power.

At higher wind speeds, closer to or just below rated speed, control mechanisms seek to maintain rated generator speed, rather than continuing to increase generator speed. The blades

will pitch forward (or "feather"), allowing the power production to maintain rated power. This process effectively decreases the amount of lift when compared to lift generated by a non-feathered blade. At these wind speeds during periods of high TI, a turbine reacts to the high variation in wind speed with subtle changes in blade pitch. For example, if the turbine detects a drop in wind speed, the blades may pitch back to generate more lift, but then if the wind speed increases quickly after, the blades will pitch forward again. If the blade pitch cannot immediately respond to increases in wind speed, then power losses occur. At these higher wind speeds, lower turbulence enables consistent blade pitch to match atmospheric conditions, and so the turbine can capture more power.

It is also important to mention the strong connection between turbulence and shear: high shear will eventually erode turbulence (Wharton and Lundquist, 2012a). Periods of high shear generally coincide with periods of low turbulence and vice versa. With low shear, the mean wind speed is more consistent over the height of the rotor disk. However, since we did not see significant differences in power curves for different shear regimes here, we cannot speculate further on this in this analysis. Finally, if veer occurs in the wind profile (as in Vanderwende and Lundquist, 2012 and Dörenkamper et al., 2014), which usually occurs only in stable or low turbulence atmospheric conditions, that veer will generally undermine power production as the turbine blades are not oriented perpendicular to the flow at all vertical levels.

4.2 Annual energy production

AEP allows developers and operators to quantify the projected energy production of a turbine. To quantify the impact on AEP of these stability- and turbulence-driven differences in power curves, we use a Weibull distribution for wind speed and calculate AEP with no filter, as well as with TI and stability filters. These turbulence and stability filters for the AEP calculations

can be further explained as AEP calculated using the power curves calculated from nacelle winds (Fig. 17a,b) as well as the power curves calculated from upwind tower winds (Fig. 17c,d). These power curves are used together with a sample wind distribution using Weibull distribution parameters based on wind speed data separated into each stability class (Table 4) as suggested by IEC 61400 12-1 (2015) for a site-specific AEP. For each of these filters, separate AEP calculations are made for each regime, weighted by the number of data points in that regime, and then added together to compare with the AEP calculated with no atmospheric filter. Note that although data are collected only during 2.5 months in the winter of 2012, AEP is calculated for an entire year to show values closer to a representative AEP value.

Table 4. Weibull parameters for the case of no stability or turbulence filter as well as for each turbulence and stability class.

	Scale parameter	**Shape parameter**	**Mean**
No filter	10.04	2.63	8.90
low TI regime	10.83	2.59	9.60
med TI regime	10.81	2.90	9.63
high TI regime	8.52	2.81	7.57
low R_B regime	10.12	3.09	9.05
med R_B regime	13.29	3.45	11.96
high R_B regime	7.64	3.10	6.83

Results in Table 5 show a higher AEP when using no filter, followed by an AEP calculated with a TI filter and then a stability filter. The lower AEP calculated when separating by stability and turbulence regimes suggests that the AEP calculated using no filters may be overestimating the production, perhaps because the higher and lower extremes of the parameter ranges bias the averages in each bin.

AEP results in Table 5 also show that the AEP calculated using nacelle winds underestimates the AEP when compared with an AEP calculated using upwind tower measurements. This underestimation of the nacelle anemometer-calculated AEP is true for both

the AEP calculated for the entire dataset as well as with each stability or turbulence filter and is likely because the nacelle anemometer underestimates the ambient wind speed due to flow interference of the rotor disk and nacelle.

Table 5. AEP in megawatt-hours/year calculated for different atmospheric and turbulence regimes using a Weibull distribution with a scale and shape parameter associated with the corresponding wind speed distribution.

	No filter	**TI filter**	**R_B filter**
AEP using tower data	7,479.3	7,409.6	7,278.7
AEP using nacelle data	7,430.6	7,388.9	7,266.7

When the AEP's low and high regimes are compared to the medium regimes of their respective atmospheric parameters, the AEP for medium-TI periods is higher than that for low-TI periods and for high-TI periods for both the nacelle anemometer-calculated AEP and the tower-calculated AEP (Table 6). Using low- and high-TI power curves results in an AEP smaller than that calculated using the medium-TI power curve. These results are likely obtained because the low-TI power curve loses production at lower wind speeds and the high-TI power curve loses production around rated speed. When using a stability filter, the AEP calculated with the low-R_B power curve is higher than that with the high-R_B power curve (Table 6). This contrast between AEP calculated for the low stability regime and AEP calculated for the high stability regimes suggests that the unstable power curve (Fig. 17b,d) gains enough production at lower wind speeds to surpass the production gain by the stable power curve (Fig. 17b,d) near rated speed.

Table 6. AEP in percentage calculated for different filter regimes using a Weibull distribution with a scale factor and a shape factor representative of the corresponding wind speed distribution. Medium regime is set at 100 % and low and high regimes are percentages compared to the medium regime. The highest value within each row is italicized.

Filter	Low regime	Medium regime	High regime
TI using tower data	85.03	*100.00*	68.20
R_B using tower data	*116.28*	100.00	71.33
TI using nacelle data	84.76	*100.00*	68.32
R_B using nacelle data	*115.86*	100.00	70.52

5 Conclusions

Using 2.5 months of data from upwind and nacelle-based instruments, we calculate power curves for different regimes of atmospheric stability and turbulence as well as AEP with and without these atmospheric filters. This work focuses not only on the idea of calculating different power curves for different atmospheric conditions for power performance testing but also highlights the differences in AEP that can emerge from the application of stability- or turbulence-dependent power curves. We also summarize extensive data quality-control methods, including two approaches for filtering out turbine underperformance or curtailments.

Statistically-significant differences emerge among power curves segregated by TI and R_B. At wind speeds between 5 and 7 m s^{-1}, during periods of high TI, significantly more power is produced than during periods of low TI. From about 10 to 14 m s^{-1} (near rated wind speed), during periods of low TI, significantly more power is produced than during periods of high TI. During periods of stable conditions, significantly more power is produced than during periods of unstable conditions around 12 m s^{-1}, and significantly less power is produced than during periods of unstable conditions at some wind speeds between 6.5 and 9.0 m s^{-1}. Statistically significant distinctions in power curves did not occur when filtering for TKE, *L*, yaw error, wind shear, or wind veer for this data set at this site, perhaps explaining why stable conditions promote

overperformance here, as in Wharton and Lundquist (2012b). A site with veer, however, exhibits underperformance in stable conditions (Vanderwende and Lundquist 2012).

After calculating an AEP for each regime and comparing the high and low regimes with the medium regime, differences between AEP calculated using different atmospheric filters are revealed. An AEP calculated with no atmospheric or turbulence filter is higher than any AEP calculated with these filters. In addition, the AEP calculated using a TI filter shows that the AEP calculated with the medium TI regime is greater than the AEP calculated with the low or high TI regimes. The AEP calculated with the R_B filter shows that the low regime AEP is much larger than the AEP in the high and medium regimes.

As a small percent difference in AEP leads to a large deviation in cost for both operators and manufacturers, calculating different power curves for different atmospheric conditions may not only be a practical approach, but may lower the financial risks for both operators and manufacturers.

As discussed by Rareshide et al. (2009), manufacturers increasingly filter out data that represent what they consider anomalous or extreme atmospheric conditions for power performance testing. The IEC-61400-12-1 standard (2015) calls for at least 180 h of data to be used in a power performance test. Consequently, if manufacturers filter out data based on higher TI values, for instance, this means that more data must be gathered to make up for the discarded data. We see this discarding of data as unnecessary and potentially more costly. We suggest that instead of discarding these data, different power curves be calculated for different conditions. This approach can allow for a more nuanced understanding of how a turbine operates in different atmospheric conditions, and may lead to a more accurate and reliable performance result and AEP calculation.

Acknowledgements

The authors express appreciation to the Center for Research and Education in Wind for supporting this work, to Thomas Fischetti and Peter Gregg at GE Renewable Energy for their assistance in turbine data collection and interpretation, and to the reviewers of a previous version of this work. This work was supported by the U.S. Department of Energy under Contract No. DE-AC36-08GO28308 with the National Renewable Energy Laboratory. Funding for the work was provided by the DOE Office of Energy Efficiency and Renewable Energy, Wind and Water Power Technologies Office.

CHAPTER IV

STABILITY AND TURBULENCE EFFECTS ON NACELLE TRANSFER FUNCTIONS

Power performance validation has traditionally relied on hub-height wind speed observations from a meteorological tower upwind of a turbine. However, tower installation and maintenance can be time-consuming and expensive. Alternatively, every utility-scale turbine installed around the world already has an anemometer mounted on the nacelle. With sufficiently accurate transfer functions to correct for the interference of the rotor blades and nacelle, is it possible the supervisory control and data acquisition (SCADA) data from these instruments can provide a valuable, extensive, and continuous source of turbine-specific performance information?

We use 2.5 months of detailed upwind and nacelle-based measurements from a utility-scale wind turbine and investigate the influence of different atmospheric stability regimes and turbulence regimes on nacelle transfer functions (NTFs) used to correct nacelle-mounted anemometer measurements. We find that: (1) fitting the data to a fifth-order polynomial to estimate the NTF results in a slightly higher r-squared value and smaller root mean squared error (RMSE) than fitting to a second-order polynomial, (2) the use of NTFs in annual energy production (AEP) calculations results in less than a 1% difference from the AEP calculated with the upwind met tower wind speed, and (3) during periods of relatively low stability and high turbulence intensity (TI) and turbulence kinetic energy (TKE), the nacelle anemometer underestimates the ambient wind speed more than during periods of relatively high stability and low TI and TKE at wind speed between cut-in and rated.

This chapter shows that correcting nacelle winds using NTFs results in more accurate AEP estimates similar to estimates obtained using upwind meteorological tower-based wind speeds. Further, stability and turbulence metrics have been investigated for their influence on NTFs and found to have an effect on NTFs below rated speed. We suggest calculating different NTFs for different conditions to determine the sensitivity of the NTFs to these atmospheric conditions, understanding of which may lead to a more accurate and reliable performance result and AEP calculation.

The following chapter is adapted and reformatted from:

St. Martin, C. M., Lundquist, J. K., Clifton, A., Poulos, G. S., and Schreck, S. J.: Atmospheric turbulence affects wind turbine nacelle transfer functions, Wind Energ. Sci. Discuss., doi:10.5194/wes-2016-45, in review, 2016.

Abstract

Despite their potential as a valuable source of individual turbine power performance and turbine array energy production optimization information, nacelle-mounted anemometers have often been neglected because complex flows around the blades and nacelle interfere with their measurements. This work quantitatively explores the accuracy of and potential corrections to nacelle anemometer measurements to determine the degree to which they may be useful when corrected for these complex flows, particularly for calculating annual energy production (AEP) in the absence of other meteorological data. Using upwind meteorological tower measurements along with nacelle-based measurements from a General Electric (GE) 1.5sle model, we calculate empirical nacelle transfer functions (NTFs) and explore how they are impacted by different atmospheric and turbulence parameters. This work provides guidelines for the use of NTFs for deriving useful wind measurements from nacelle-mounted anemometers. Corrections to the

nacelle anemometer wind speed measurements can be made with NTFs and used to calculate an AEP that comes within 1 % of an AEP calculated with upwind measurements. We also calculate unique NTFs for different atmospheric conditions defined by temperature stratification as well as turbulence intensity, turbulence kinetic energy, and wind shear. During periods of low stability as defined by the Bulk Richardson number (R_B), the nacelle-mounted anemometer underestimates the upwind wind speed more than during periods of high stability at some wind speed bins below rated speed, leading to a more steep NTF during periods of low stability. Similarly, during periods of high turbulence, the nacelle-mounted anemometer underestimates the upwind wind speed more than during periods of low turbulence at most wind bins between cut-in and rated wind speed. Based on these results, we suggest different NTFs be calculated for different regimes of atmospheric stability and turbulence for power performance validation purposes.

1 Introduction

Traditionally, each wind turbine has an anemometer and wind vane mounted on its nacelle, behind the hub (Fig. 1). Measurements collected from these instruments are used for yaw control and turbine cut-in/cut-out procedures. Nacelle measurements could also be used to help improve turbine or park efficiency. For example, power performance verifications for individual turbines can now be based on the nacelle anemometer with suitable nacelle transfer functions (NTFs) (International Electrotechnical Commission [IEC] 61400-12-2 2013). Nacelle measurements can also provide critical input for wind farm production optimization (Fleming et al., 2016). With sufficiently accurate NTFs, these data can provide a valuable, extensive, and continuous source of turbine-specific performance information.

Power performance validation has traditionally relied on hub-height wind speed observations from a meteorological (met) tower upwind of a turbine (Link and Santos, 2004; IEC 61400-12-1, 2015). The IEC 61400-12-1 (2015) standards require a met tower to be placed at the turbine location prior to turbine erection (the so-called "site calibration" procedure) for a power performance test to be considered valid (of sufficiently low total uncertainty) in complex terrain. However, it is not feasible to erect "site calibration" met towers after the turbine has been erected. And, even if "site calibration" is not required because a site is in simple terrain, tower erection is time-consuming and unrealistic to complete for every turbine at a given park. These factors motivate exploration of the use of nacelle-mounted anemometers to provide wind speed data for power performance validation.

Figure 1. GE-1.5/77 sle turbine at the National Wind Technology Center. Photo credit: Dennis Schroeder/NREL (image gallery number 25872).

Several studies have found that nacelle anemometer measurements can be adjusted by the use of transfer functions between some upwind hub-height measurement and the nacelle-mounted anemometer measurement (Antoniou and Pedersen, 1997; Hunter et al., 2001, Smith et al., 2002; Smaïli and Masson, 2004). The IEC 61400-12-2 (2013) standard now allows the use of nacelle-mounted anemometers to verify power curves based on these transfer functions, or fitted functions of correction factors between upwind hub-height wind speed (UHWS) measurements and nacelle-mounted anemometer wind speed (NAWS) measurements.

An empirical NTF may not result in a linear relationship between the UHWS and NAWS. In fact, Antoniou and Pedersen (1997) found that the transfer functions fit well with a fifth-order polynomial curve. Hunter et al. (2001) similarly found a non-linear relationship and that a linear regression would overestimate the wind speed between 6 and 11 m s^{-1} and underestimate the wind speed at wind speeds less than 4 m s^{-1} and greater than 16 m s^{-1}. Smith et al. (2002) found a linear relationship with the exception of wind speeds below cut-in and wind speeds about 15 m s^{-1}.

In previous work, the relationship between UHWS measurements and NAWS measurements has been found to depend on multiple factors. Antoniou and Pedersen (1997) found that relations between the UHWS and the NAWS were dependent on rotor settings such as blade pitch angle and the use of vortex generators, yaw error, anemometer position, and terrain. They concluded that if these factors were kept constant, the relation could be used for all wind turbines of the same make and type. Frandsen et al. (2009) found a dependence on flow induction caused by the rotor. Dahlberg et al. (1999) discovered that pitch angle affects the relation. Dahlberg et al. (1999), Smith et al. (2002), and Frandsen et al. (2009) also stressed the importance of the correct calibration of the nacelle anemometers and that this calibration has an

effect on the error measured in the relation. Zahle and Sørensen (2011) found that the inflow angle to the rotor and yaw misalignment influences the relationship. Smith et al. (2002) concluded the relation may depend on turbine controls, topography, and nacelle height and position. Smaïli and Masson (2004) implemented a numerical model and concluded that a relation should account for rotor-nacelle interactions and hypothesized that wakes, topography, and nacelle misalignment would all have some effect on the relation. To summarize, the factors found to be relevant in NTFs are: rotor settings, yaw error, anemometer position, terrain, flow induction (decrease in wind speed just in front of or just behind the rotor), nacelle anemometer calibration, and inflow angle.

The roles of inflow turbulence and atmospheric stability on NTFs have not yet been explored. However, previous work on power performance and annual energy production (AEP) does acknowledge the role of atmospheric stability, wind shear, and turbulence intensity (TI) in inducing deviations of power from the manufacturer power curve (MPC) (e.g., Sumner and Masson, 2006; Antoniou et al., 2009; Rareshide at el., 2009; Wagenaar and Eecen, 2011; Wharton and Lundquist, 2012a; Vanderwende and Lundquist, 2012; St. Martin et al., 2016).

In this study, we quantify the effect of NTF-corrected nacelle anemometer measurements on the AEP and investigate the influence of different atmospheric stability and turbulence regimes on these NTFs. In Sect. 2, we briefly summarize our data set, which includes upwind as well as nacelle-based measurements, as well as our data analysis methods which include filtering based on turbine operation, and definitions of the stability and turbulence regimes. We present results of AEP calculations as well as separate NTFs for different stability and turbulence regimes in Sect. 3, and in Sect. 4 we summarize conclusions about the effect of the NTF on the AEP as well as the effects of atmospheric stability and inflow turbulence on the NTFs.

2 Data and methods

2.1 Meteorological and turbine data

For this analysis, we use 2.5 months of data collected at the U.S. Department of Energy (DOE) National Wind Technology Center (NWTC) at the National Renewable Energy Laboratory (NREL) during the wintertime (29 November 2012–14 February 2013). Ten-minute-averaged turbine supervisory control and data acquisition (SCADA) data used in this study are from a General Electric (GE)-1.5-MW turbine (GE-1.5/77 sle, Fig. 1), with a cut-in wind speed of 3.5 m s^{-1}, rated wind speed of 14 m s^{-1}, and cut-out wind speed of 25 m s^{-1}. A map of the site can be found in St. Martin et al. (2016) (Fig. 1). See Mendoza et al. (2015) for power performance test results from the DOE GE-1.5 along with instrument and site calibration information.

Upwind data include 1-Hz measurements of wind speed and direction averaged to 10 min from a Renewable NRG Systems (NRG)/LEOSPHERE WINDCUBE v1 vertically profiling Doppler lidar (2.7 D upwind) and 10- and 30-min averages from a 135-m met tower (2.0 D upwind). Volumetric-averaged wind speeds and directions are measured by the lidar every 20 m, from 40 m to 220 m. Comparison of the lidar wind profiles to those from the met tower suggest that the lidar data at this site suffered from inhomogeneities as a result of complex flows (Bingöl et al., 2009; Rhodes and Lundquist, 2013; Lundquist et al., 2015), and so the majority of this paper will focus on the results of the analysis using the tower data. On the met tower, cup anemometers placed at 3, 10, 30, 38, 55, 80, 87, 105, 122, and 130 m measure wind speed, vanes placed at 3, 10, 38, 87, and 122 m measure wind direction, and three-dimensional (3-D) sonic anemometers placed at 15, 41, 61, 74, 100, and 119 m measure the components of the wind.

Barometric pressure and precipitation amounts are measured at 3 m and temperature is measured at 3, 38, and 87 m. See Fig. 2 in St. Martin et al. (2016) for a schematic of the tower.

As discussed in St. Martin et al. (2016), meteorological and turbine data are filtered for quality assurance. Data are only considered during time periods when the turbine is operating and wind direction indicates the turbine is located downwind of the lidar and met tower (235°–315°). As the turbine data from the SCADA system is available in 10-min increments, variability of the turbine parameters on a shorter timescale cannot be discerned. However, we filter for "normal turbine operation" based on curtailment using generator speed set point for wind speeds greater than 5.5 m s^{-1}, whereas for wind speeds less than 5.5 m s^{-1}, we discard data when the turbine is not grid-connected and is faulted (Fig. 6 in St. Martin et al., 2016).

Further, it is possible that the nacelle-reported wind speeds used in this analysis have been subjected to a simple, built-in transfer function before the retrieval from the SCADA system of the DOE GE 1.5sle turbine. We see this uncertainty as an advantage to our analysis as a typical wind plant operator would only have access to similar data.

2.2 AEP calculations

To simulate a scenario in which a wind plant operator only has nacelle-based measurements and no upwind tower or remote-sensing measurements, we calculate an AEP (as described in Sect. 9.3 of IEC 61400-12-2, 2013) using only nacelle winds to compare to an AEP calculated with upwind met tower 80-m winds. We then correct the nacelle-based measurements with NTFs and calculate AEP based on these results for comparison as well. Although data for this analysis only spans 2.5 months in the wintertime at the NWTC during the 2012–2013 season, we calculate AEPs using the total amount of hours in an entire year to show values close

to a representative AEP value. A sample wind distribution using Weibull distribution parameters representative of the data set (scale parameter: λ = 10.04 m s^{-1}, shape parameter: k = 2.63, figure not shown) is used in these calculations as suggested by IEC 61400 12-1 (2015) for a site-specific AEP.

2.3 Stability metrics

We calculate Bulk Richardson number (R_B), Obukhov length (L), and the power law exponent (α) and use these as stability metrics for these data. Using wind speed and temperature differences between surface and upper tip (3 m and 122 m, respectively) tower measurements, we calculate 10-min values of R_B to compare the buoyant production of turbulence to the mechanical production of turbulence. Using near-surface flux measurements at 15 m (within the surface layer) as well as surface temperature and humidity measurements interpolated to 15 m, we calculate 30-min values of L to estimate the height at which the buoyant production of turbulence dominates the mechanical production of turbulence. Using horizontal wind speeds as measured by cup anemometers at 38 m and 122 m (lower tip and upper tip of the rotor disk), we calculate 10-min values of α to quantify the wind speed vertical profile across the rotor disk. Though some previous studies combine metrics to define stability (Vanderwende and Lundquist, 2012), the three atmospheric stability metrics discussed here are treated separately with regard to the NTFs because of slight differences between their definitions of unstable and stable conditions (see Fig. 11 in St. Martin et al., 2016). These differences may be attributed to distinctions between each approach in defining atmospheric stability, a difference in averaging period, heights of the measurements used in the calculations, or how R_B and L use wind speed and temperature measurements to define stability, whereas α uses only wind speed measurements.

Further, we calculate TI and turbulence kinetic energy (TKE) to provide turbulence metrics and estimate the effect of hub-height inflow turbulence on the NTFs. Using 80-m wind speed measurements from the met tower, we calculate 10-min values of TI, or the standard deviation of the horizontal wind speed normalized by the average horizontal wind speed at hub height. Using 74-m wind measurements from a 3-D sonic anemometer on the tower, we calculate 30-min values of TKE per unit mass, or the sum of the variances of the components of the wind divided by two. Note that after filtering out spikes in the raw 74-m sonic anemometer data, only about 367 thirty-min TKE values remain (183.5 h) and the fewer number of data points likely affects the statistical significance of the NTFs for different TKE regimes.

Regimes or classifications for these stability and turbulence parameters are defined in Table 1 and described in detail in St. Martin et al. (2016), along with more detailed descriptions of the data from the lidar, tower and turbine, as well as filtering methods.

Table 1. Defined stability and turbulence regimes.

Regime	R_B	L **(m)**	α	**TI (%)**	**TKE ($m^2 s^{-2}$)**
Low	$R_B < -0.03$	$-1{,}000 < L \leq 0$	$\alpha < 0.11$	TI < 15	TKE < 3.0
Medium	$-0.03 < R_B < 0.03$	$0 \leq L < 1{,}000$	$0.11 < \alpha < 0.17$	15 < TI <20	3.0 < TKE < 6.5
High	$R_B > 0.03$	$\lvert L \rvert \geq 1{,}000$	$\alpha > 0.17$	TI > 20	TKE > 6.5

3 Results

To explore the variability of the NTF, we calculate specific NTFs filtered by atmospheric stability metrics, TI, and TKE. We investigate filters that have either previously been found to affect the transfer function or are suspected to have an effect on the transfer functions based on power curve studies (e.g., St. Martin et al., 2016). Additionally, we explore the effects of yaw error and wind veer and distributions of these variables, but, as in St. Martin et al. (2016), yaw

error and wind veer do not seem to impact either the power curves or the NTFs at this site and therefore are not shown.

3.1 Preliminary NTFs

A general NTF (Fig. 2a) compares the tower 80-m wind speed to the nacelle-reported wind speed using all data that pass the wind speed, wind direction, and normal operation criteria defined in Sect. 2.1 and in more detail in Sect. 3.2 and 3.3 in St. Martin et al. (2016). As a fifth-order polynomial fit was found to be suitable for power curve assessment in previous work by Antoniou and Pedersen (1997) and Hunter et al. (2001), we also apply this type of fit to the wind speeds in this work to estimate an empirical transfer function between 80-m tower wind speed measurements and nacelle-mounted anemometer wind speed measurements (Fig. 2a). The r-squared value of the fifth-order polynomial fit to the data is 0.9912, which means the fit line predicts 99.12% of the variance in the tower data. The root-mean-square error (RMSE) of the fifth-order polynomial fit is 0.3615 m s^{-1}. After correcting the nacelle-measured wind speeds using this NTF, deviations between the corrected nacelle wind speed and the tower 80-m wind speeds (Fig. 2b) vary between -0.2 and 0.2 m s^{-1} throughout all wind speed bins between cut-in and cut-out wind speed.

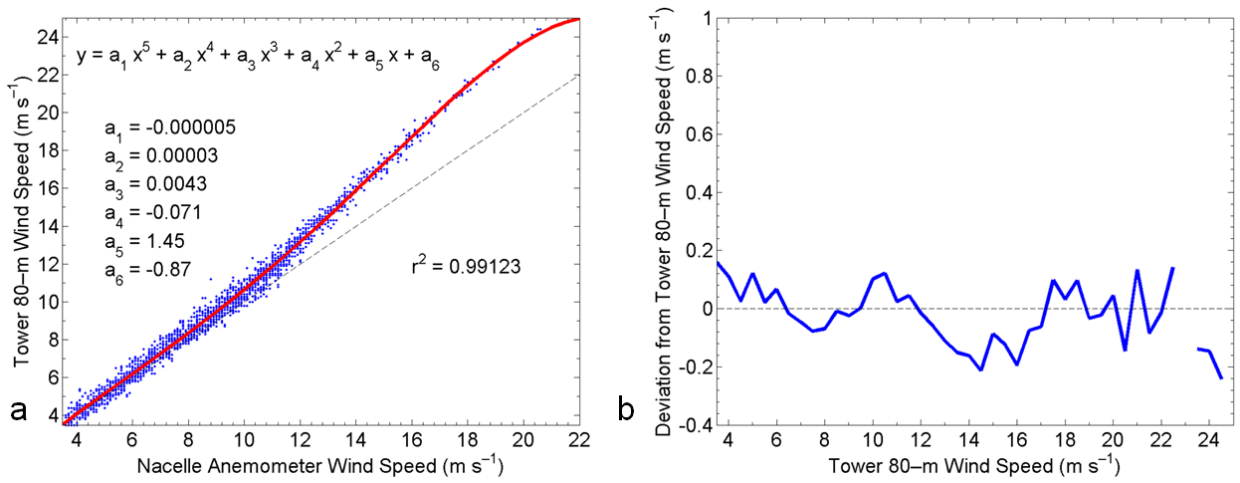

Figure 2. Comparison of upwind wind speeds with nacelle anemometer wind speeds: (a) Scatter is the upwind tower 80-meter (m) wind speed versus nacelle wind speed. Red line is the fifth-order polynomial fit and empirical transfer function between the tower 80-m observations and the nacelle-mounted anemometer observations. Dashed line is 1:1. (b) Average deviation in fifth-order polynomial nacelle transfer function (NTF)-corrected nacelle-mounted anemometer wind speed from tower 80-m wind speed versus tower 80-m wind speed. The dashed line indicates a 0 m s^{-1} change. The figure includes data filtered for the tower 80-m wind speeds between 3.5 and 25.0 m s^{-1}, 87-m wind directions between 235° and 315°, and for normal turbine operation.

Based on the small coefficients of the third-, fourth-, and fifth-order of the fit in Fig. 2a, a fifth-order polynomial may be unnecessarily complex. Therefore, a second-order polynomial fit is also calculated to estimate an empirical transfer function. The r-squared value of the second-order polynomial fit with the data is also very high, 0.9909 (Fig. 3a). The RMSE of the second-order polynomial fit is 0.3680 m s^{-1}. After correcting the nacelle-measured wind speeds using this NTF, deviations between the corrected nacelle wind speed and the tower 80-m wind speeds, shown in Fig. 3b, vary from about -0.3 to 0.2 m s^{-1} at wind speed less than about 22 m s^{-1} but grow to about 0.8 m s^{-1} at higher wind speeds. Though there are fewer data points at these higher wind speed bins, this larger deviation of the second-order NTF-corrected wind speeds from the upwind wind speeds at higher wind speeds suggests that a fifth-order polynomial NTF is unnecessary until high wind speeds are considered.

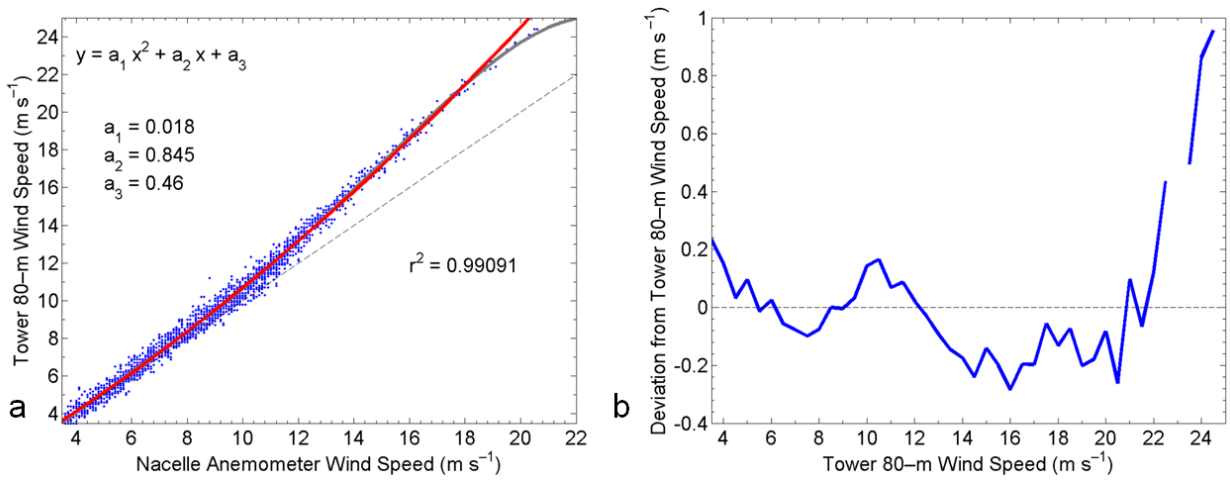

Figure 3. Comparison of upwind wind speeds with nacelle anemometer wind speeds. (a) Scatter is the upwind tower 80-m wind speed versus nacelle wind speed. Red line is the second-order polynomial fit and empirical transfer function between the tower 80-m observations and the nacelle-mounted anemometer observations; gray line is the fifth-order polynomial fit. Dashed line is 1:1. (b) Average deviation in the second-order polynomial NTF-corrected nacelle-mounted anemometer wind speed from tower 80-m wind speed versus tower 80-m wind speed is shown. Dashed line indicates a 0 m s^{-1} change. Includes data filtered for tower 80-m wind speeds between 3.5 and 25.0 m s^{-1}, 87-m wind directions between 235° and 315°, and for normal turbine operation.

Both transfer functions for this dataset (Fig. 2a, Fig. 3a) are close to linear at low wind speeds but non-linear just before rated speed (14 m s^{-1}), hence the higher-order polynomial fits. This behavior suggests that at wind speeds below about 9 m s^{-1}, the nacelle anemometer measurement closely corresponds to the upwind wind speed. Above this wind speed threshold, however, the nacelle anemometer underestimates the upwind wind speed by almost 2 m s^{-1} around rated speed to about 4 m s^{-1} at upwind wind speeds near 20 m s^{-1}; higher ambient wind speeds are associated with more significant slow-downs around the nacelle.

Comparison of the NTF developed from the upwind tower measurements and the NTF developed from the upwind lidar measurements (Fig. 4a) emphasizes that the lidar measurements exhibit greater variability ranging over all relevant wind speeds. The variability in the lidar

measurements caused by the inhomogeneity of the flow suggests that the tower measurements are more reliable for calculating power curves and transfer functions at this particular site, which is known to experience complex and inhomogeneous flow (Aitken et al., 2014b). Despite the larger variability in the lidar data set for both the transfer function (Fig. 4a) and deviations between the corrected nacelle wind speed and the upwind wind speeds (Fig. 4b), both transfer functions in Fig. 4a show linearity at lower wind speeds and non-linearity at higher wind speeds.

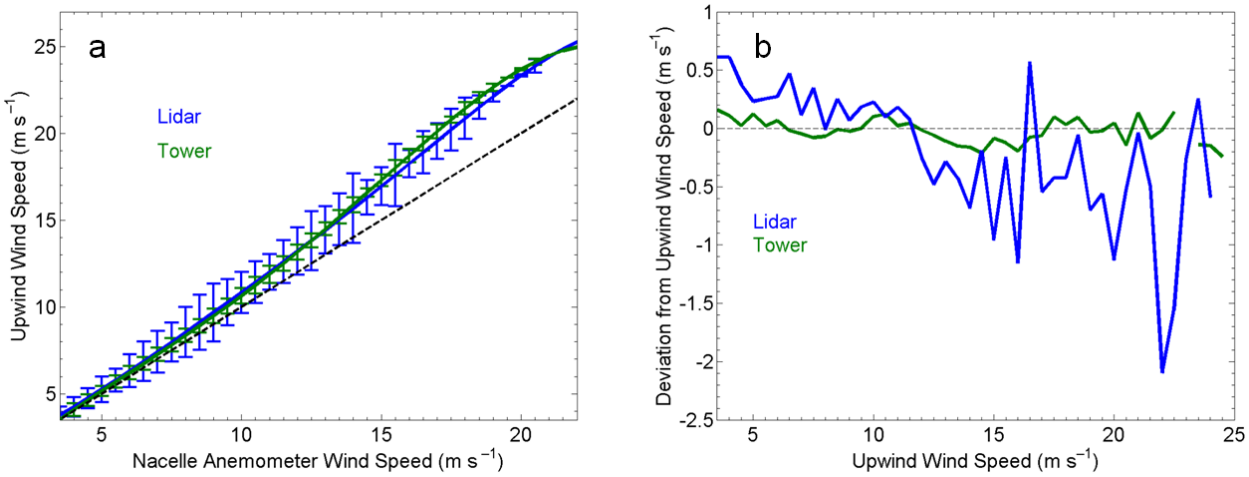

Figure 4. (a) NTFs calculated employing fifth-order polynomial fits using tower hub-height data (green) and lidar hub-height data (blue). Envelopes represent ± σ of the data within the same bins as the bins the NTFs are calculated with. Includes data filtered for tower 80-m wind speeds between 3.5 and 25.0 m s^{-1}, 87-m wind directions between 235° and 315°, and for normal turbine operation. Dashed line is 1:1; (b) shows the average deviation in NTF-corrected nacelle-mounted anemometer wind speed from tower 80-m wind speed (green) and lidar 80-m wind speed (blue) versus tower 80-m wind speed. Dashed line indicates a 0 m s^{-1} change.

To try to quantitatively explain this change in the transfer function from linear to non-linear and to connect with possible flow blockage behind the rotor and along the nacelle, the non-dimensional Froude number (Stull, 1988) for flow around the nacelle is calculated. Froude

numbers are investigated during stable conditions using measurements from the tower at the surface and around hub height and using a range of length scales from 1–10 m to represent the length and width of the nacelle. However, distinctions between these two wind speed regions could not be seen in these calculations as Froude numbers were found to be positive and increase with increasing wind speed.

Additionally, because the transfer functions become non-linear between cut-in wind speed and rated speed, the transfer function may be impacted by turbine operations in that region of the power curve possibly because of root vortices (Whale et al., 2000). Just below rated speed, the blades begin to pitch forward to maintain rated generator speed, thus allowing power production to remain near rated power (Fig. 5). This "feathering" of the blades changes the flow around the blades and therefore the wind that affects the nacelle-mounted anemometer measurement. Though this hypothesis cannot be further investigated within this campaign as higher resolution data from the SCADA system are unavailable, this does make a compelling argument for installing 3-D sonic anemometers on nacelles so vertical velocity can be measured to further understand the 3-D wind structures behind the rotor and along the nacelle, and how these flow structures change as inflow wind speed increases.

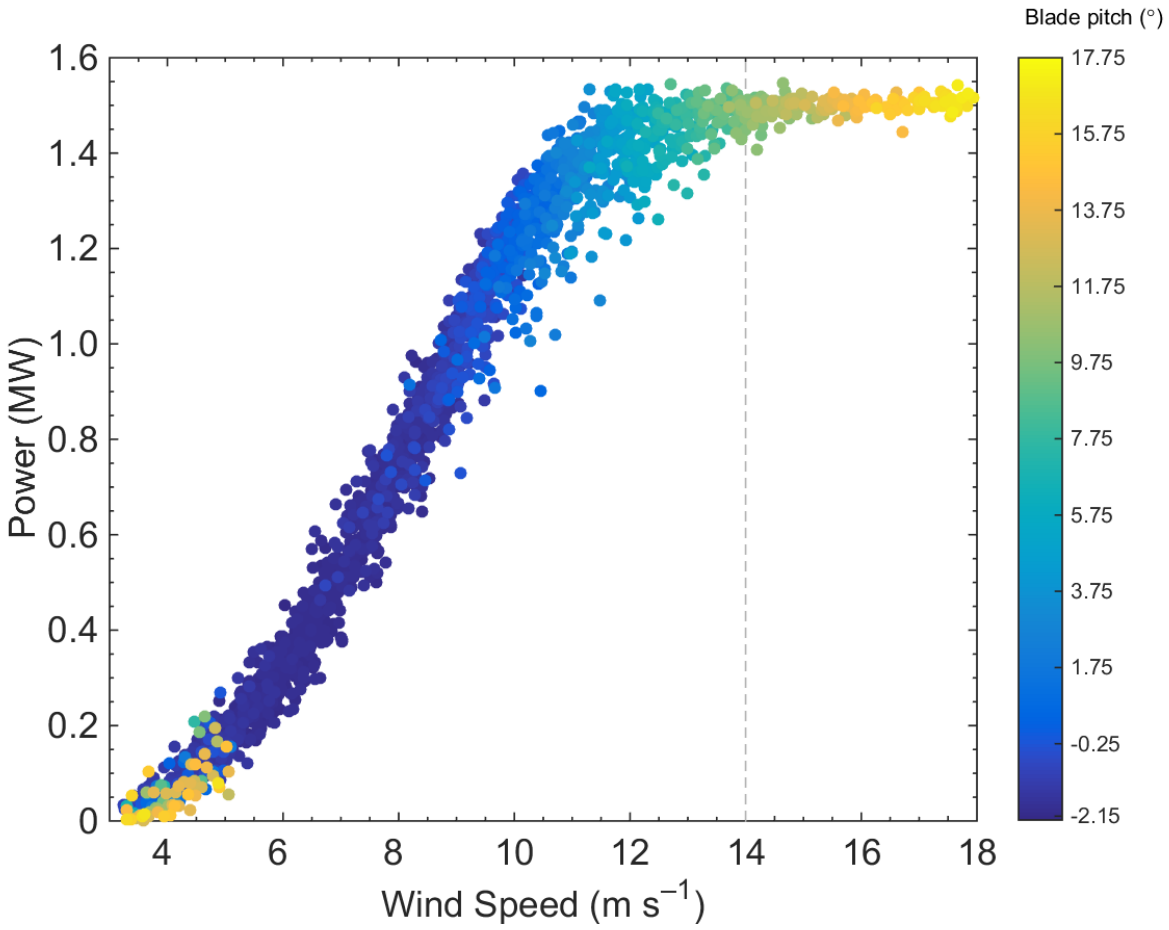

Figure 5. Scatter power curve using 80-m tower winds after filtering for wind speeds between 3.5 and 25 m s^{-1}, wind directions between 235°and 315°, and for normal turbine operation. Colors of the scatter points correspond to blade pitch angles. The grey dashed line marks rated speed.

3.2 Annual energy production and NTFs

It is important to understand the characteristics of the NTF and how it changes with wind speed, as this under-estimation of the ambient wind speed, especially at wind speeds in which the growth in power production with wind speed is the most significant, could result in a significant overestimation of AEP in power performance verification.

With no NTF correction applied (aside from the transfer function that is built into the SCADA system by the manufacturer), the AEP calculated with nacelle winds (AEP_nacelle) overestimates the AEP calculated with 80-m tower winds (AEP_upwind) by 5.96 % (Table 2).

This overestimation of AEP is expected as the nacelle anemometer consistently underestimates the upwind wind speed, which leads to the misrepresentation of higher power output at lower wind speeds and therefore a higher AEP.

Table 2. Top row: Annual energy production (AEP) in megawatt-hours/year calculated using upwind tower measurements (AEP_upwind), nacelle winds (AEP_nacelle), corrected nacelle winds using the NTF calculated with a fifth-order polynomial (AEP_NTF5th), and corrected nacelle winds using the NTF calculated with a second-order polynomial (AEP_NTF2nd). Bottom row: AEP in percentage calculated as the difference from AEP_upwind.

	AEP_upwind	**AEP_nacelle**	**AEP_NTF5th**	**AEP_NTF2nd**
AEP (MWh/y)	7,479.3	7,924.7	7.479.1	7,465.8
% of tower winds	100.00	105.96	100.00	99.82

The use of the general NTF to correct the nacelle anemometer measurements reduces the AEP error significantly (Table 2). With the application of the fifth-order polynomial NTF (AEP_NTF5th), AEP_NTF5th underestimates AEP_upwind by only 0.003 %, whereas with the application of the second-order polynomial NTF (AEP_NTF2nd), AEP_NTF2nd underestimates AEP_upwind by 0.18 %. Therefore, using either the fifth-order polynomial or the second-order polynomial for the NTF results in an AEP similar to that of an AEP calculated with upwind hub-height winds; though both lead to a slight underestimation.

3.3 Atmospheric stability effects of NTFs

The value of atmospheric-stability segregation for NTFs seems to depend on how stability is defined. Some statistically significant distinctions in the NTFs for R_B-defined unstable and stable cases do emerge (Fig. 6a, Table 3), particularly for wind speeds between 7 and 11 m s^{-1}. Closed circles in Fig. Figure a-c represent statistically distinct wind speed bins between the stability classes and are determined by the Wilcoxon rank sum test with a 1 % significance level. Stable cases follow a linear relationship more closely for low and moderate

wind speeds (less than 11 m s^{-1}), whereas unstable cases show more deviation from the 1:1 line at wind speeds greater than 8 m s^{-1}. Conversely, no statistically significant distinctions emerge in the NTFs for *L*-defined stability classes for this site using our dataset (Fig. 6b, Table 3). Distinctions in the NTFs for α-defined cases (Fig. 6c, Table 4) emerge only around 13.5 m s^{-1}—much closer to rated speed—and stable cases underestimate the upwind wind speed more than unstable cases.

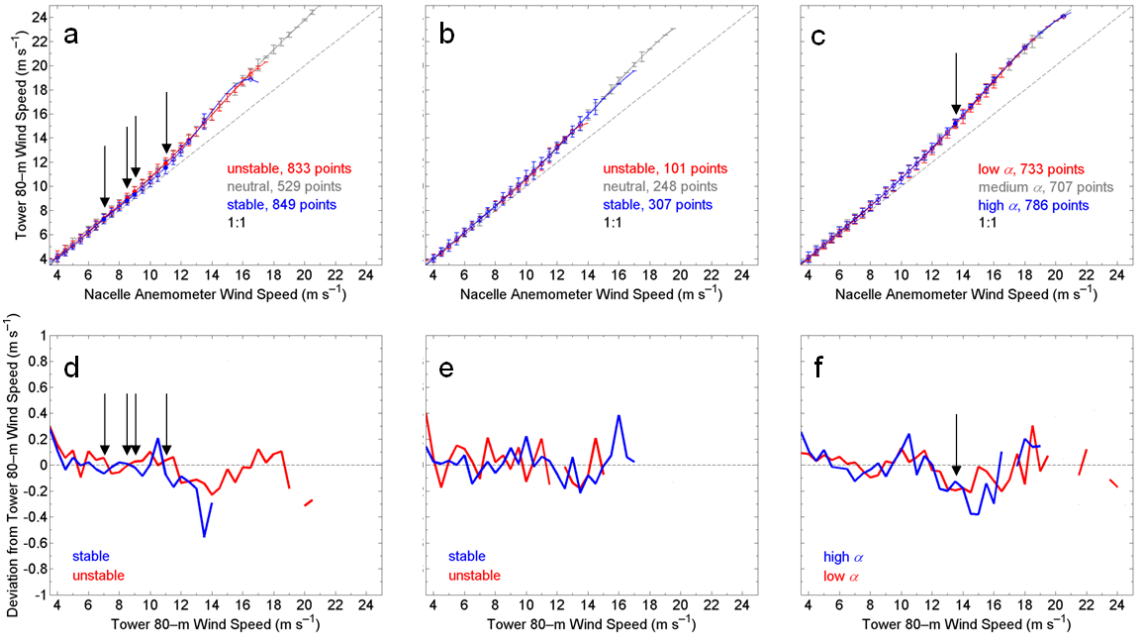

Figure 6. Tower 80-m NTFs calculated using fifth-order polynomial fits with stability regimes based on (a) R_B, (b) L, and (c) α. Error bars represent ± σ of the data within the same bins as the bins with which the NTFs are calculated. Statistically distinct differences within each wind speed bin between the stability classes are determined by the Wilcoxon rank sum test with a 1 % significance level and denoted by closed circles. Black arrows point towards statistically distinct bins. The figures include data filtered for tower 80-m wind speeds between 3.5 and 25.0 m s^{-1}, 87-m wind directions between 235° and 315°, and for normal turbine operation. Average deviation in NTF-corrected nacelle-mounted anemometer wind speed from tower 80-m wind speed is shown during stable conditions (blue) and during unstable conditions (red) versus tower 80-m wind speed with stability regimes based on (d) R_B, (e) L, and (f) α. Dashed line indicates a 0 m s^{-1} change.

Table 3. Coefficients for fifth-order polynomial NTFs for stability metrics.

	R_B			L		
Regime	**Convective**	**Neutral**	**Stable**	**Convective**	**Neutral**	**Stable**
a_1	-6.4141x10^{-5}	3.7809x10^{-5}	-3.0593x10^{-4}	-6.7085x10^{-4}	2.9071x10^{-6}	-3.8242x10^{-5}
a_2	0.0030	-0.0025	0.0142	0.0287	-4.4810x10^{-4}	0.0016
a_3	-0.0539	0.0621	-0.2473	-0.4721	0.0153	-0.0245
a_4	0.4628	-0.6843	2.0334	3.7194	-0.1881	0.1789
a_5	-0.8555	4.4391	-6.8356	-12.9316	2.0185	0.4534
a_6	2.9265	-5.9942	11.3853	19.7947	-1.9273	0.5361

Table 4. Coefficients for fifth-order polynomial NTFs for the shear exponent.

	α		
Regime	**Convective**	**Neutral**	**Stable**
a_1	-2.3643x10^{-5}	1.4220x10^{-5}	-5.9409x10^{-6}
a_2	0.0011	-0.0011	7.3499x10^{-5}
a_3	-0.0202	0.0301	0.0038
a_4	0.1781	-0.3451	-0.0689
a_5	0.2889	2.7912	1.4373
a_6	1.0387	-3.2175	-0.7869

This behavior shown by NTFs segregated by R_B suggests that below rated speed in convective conditions, the nacelle anemometer underestimates the ambient wind speed more than in stable conditions. We speculate that at wind speeds below rated, mixing in the atmosphere during more convective conditions, as well as the turbine interaction with these turbulent eddies, may result in additional motion that exaggerates blockage effects by the rotor and nacelle and causes underestimation by the nacelle-mounted anemometer.

We apply the NTFs to the nacelle anemometer measurements to evaluate the deviations from the upwind met tower data (Fig. 6d-f); however, the results show no consistency or systematic distinctions between stability metrics, stability classes, or wind speed.

3.4 Turbulence effects on NTFs

The hypothesis that convectively-driven mixing and turbulence causes underestimation by the nacelle-mounted anemometer is further supported in the NTFs segregated by TI (Fig. 7a, Table 5) and TKE classes (Fig. 7b, Table 5). Distinctions between unstable and stable cases in the transfer functions for wind speeds between 5.5 and 12 m s^{-1} are also apparent when the transfer functions are segregated by TI class (Fig. 7a) and for wind speeds around 12 m s^{-1} when the transfer functions are segregated by TKE class (Fig. 7b). Periods of relatively high TI and TKE result in greater underestimations of the wind speed by the nacelle anemometer from just above cut-in wind speed to about 12 m s^{-1}.

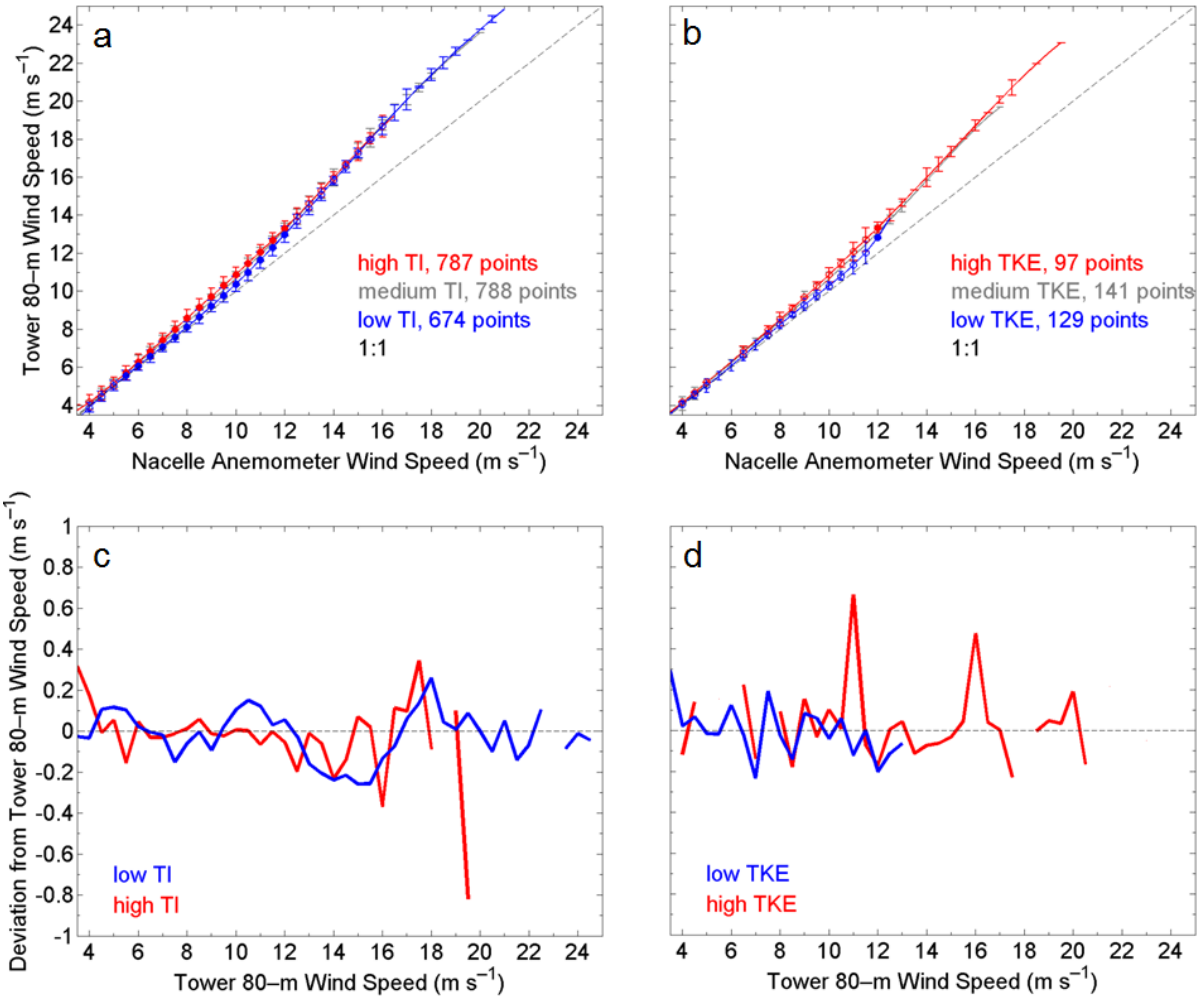

Figure 7. Tower 80-m NTFs calculated using fifth-order polynomial fits with turbulence regimes based on (a) turbulence intensity (TI) and (b) turbulence kinetic energy (TKE). Error bars represent ± σ of the data within the same bins as the bins with which the NTFs are calculated. Statistically distinct differences within each wind speed bin between the stability classes are denoted by closed circles. Figures include data filtered for tower 80-m wind speeds between 3.5 and 25.0 m s^{-1}, 87-m wind directions between 235° and 315°, and for normal turbine operation. Average deviation in NTF-corrected nacelle-mounted anemometer wind speed from tower 80-m wind speed is shown during stable conditions (blue) and during unstable conditions (red) versus tower 80-m wind speed with turbulence regimes based on (c) TI and (d) TKE. Dashed line indicates a 0 m s^{-1} change.

Corrections to the nacelle wind speeds using NTFs based on atmospheric turbulence show lower deviations from the ambient wind speed below rated speed and larger deviations from the ambient wind speed after rated speed for high TI cases. However, similar to the results

in Fig. 6d–f, Fig. 7c–d also show inconsistencies between deviations from the upwind speed for the different turbulence metrics and regimes.

Table 5. Coefficients for fifth-order polynomial NTFs for turbulence metrics.

	TI			**TKE**		
Regime	**High**	**Med**	**Low**	**High**	**Med**	**Low**
a_1	-9.0463x10^{-5}	1.5534x10^{-5}	2.3161x10^{-5}	-1.3295x10^{-5}	-6.7464x10^{-5}	4.5266x10^{-4}
a_2	0.0045	-0.0012	-0.0017	6.0813x10^{-4}	0.0031	-0.0156
a_3	-0.0842	0.0305	0.0428	-0.0103	-0.0539	0.2048
a_4	0.7602	-0.3409	-0.4763	0.0949	0.4418	-1.2609
a_5	-2.1704	2.7552	3.3911	0.6268	-0.6458	4.6488
a_6	5.0077	-3.2307	-4.4045	0.6460	2.3183	-3.9372

4 Conclusions

Over two months of data from both upwind instruments and nacelle-based instruments are used to quantify general nacelle transfer functions (NTFs) as well as NTFs that vary with atmospheric stability and turbulence parameters. We show that correcting nacelle winds using these NTFs results in more accurate annual energy production (AEP) estimates that are similar to estimates obtained using upwind meteorological (met) tower-based wind speeds. Further, multiple factors have been investigated for their influence on NTFs, including both parameters known to influence wind power production and parameters never before investigated in the context of transfer functions.

We find that fitting the data to a fifth-order polynomial to estimate the NTF results in a slightly higher r-squared value and smaller root-mean-square error (RMSE) than fitting to a second-order polynomial. The small differences in the uncertainties between the two methods

seem insignificant, as the r-squared value of 0.9909 using the second-order polynomial is comparable to the 0.9912 value using the fifth-order fit. However, though the r-squared value of the second-order fit is high, after correcting the nacelle winds with the second-order NTF, larger deviations from the upwind tower winds occur than if a fifth-order NTF is used, especially at higher wind speeds.

At wind speeds below 9 m s^{-1}, the nacelle anemometer measurement closely corresponds to the upwind wind speed measurement. Above this wind speed threshold, however, the nacelle anemometer underestimates the upwind wind speed, which could result in a significant underestimation of power production and could be perceived as turbine over-performance (or mask turbine under-performance) if not corrected for by a NTF. Additionally, the non-linear nature of the transfer functions above 9 m s^{-1} or so suggests that the transfer function may be impacted by turbine operations near rated speed and how they affect the flow behind the rotor disk and along the nacelle.

The use of NTFs in AEP calculations results in a less than 1 % difference from the AEP calculated with the upwind met tower wind speed. AEP calculations reveal that an AEP calculated using a fifth-order polynomial correction to the nacelle winds results in a 0.003 % underestimation of the AEP calculated with the upwind wind speed, whereas an AEP calculated using a second-order polynomial correction results in a 0.18 % underestimation of the AEP calculated with the upwind wind speed. Both are sizeable improvements over using the uncorrected nacelle wind speed, which leads to a 5.96 % overestimation when compared to the AEP calculated with the upwind wind speed.

Statistically significant distinctions emerge in the transfer functions for unstable and stable cases as defined by the Bulk Richardson number (R_B), particularly for wind speeds

between 9 and 11 m s^{-1}. At these wind speeds before rated, in unstable conditions, the nacelle anemometer underestimates the ambient wind speed more often than in stable conditions. Similar but more prominent behavior is found in transfer functions separated by turbulence intensity (TI) and turbulence kinetic energy (TKE) classifications: during periods with relatively high TI and TKE, the nacelle anemometer underestimates the ambient wind speed more than during periods of relatively low TI and TKE, between about 6 and 12 m s^{-1}. We speculate that turbine interaction with the mixing in the atmosphere during more convective and turbulent conditions may result in additional motion, thereby exaggerating the blockage by the nacelle and thus underestimation by the nacelle-mounted anemometer.

Distinctions in power curves (Sumner and Masson, 2006; Antoniou et al., 2009; Vanderwende and Lundquist, 2012; Dörenkämper et al., 2014; St. Martin et al., 2016) can lead to a correlation between these and distinctions in NTFs as well as the idea of validating power performance data with similar atmospheric and operational characteristics with their corresponding power curve in an effort to decrease the amount of uncertainty in power performance testing.

NTFs have recently been accepted for power curve validation under certain circumstances (IEC 61400-12-2, 2013). They can also enable the use of nacelle-mounted anemometers for AEP estimates, turbine performance analysis, and data assimilation for improved forecasting (Draxl, 2012; Delle Monache et al., 2013).

Further work could explore how turbine controls and characteristics such as thrust affect the transfer functions. Simulations of flow around the nacelle such as those of Keck (2012) could be expanded to account for variations in atmospheric stability and could be coupled with control software simulators. As Bibor and Masson (2007) suggest, a single transfer function should not

be used for every wind plant site and for every atmospheric and operating condition. Several atmospheric and operational conditions and how they affect the transfer functions should be investigated and perhaps combined to provide an algorithm for manufacturers and wind plant operators to use in power performance validation.

Acknowledgements

The authors express appreciation to the Center for Research and Education in Wind for supporting this work, to Thomas Fischetti and Peter Gregg at GE Renewable Energy for their assistance in turbine data collection and interpretation, and to the reviewers of a previous version of this work. This work was supported by the U.S. Department of Energy under Contract No. DE-AC36-08GO28308 with the National Renewable Energy Laboratory. Funding for the work was provided by the DOE Office of Energy Efficiency and Renewable Energy, Wind and Water Power Technologies Office.

CHAPTER V

SIMULATING WIND TURBINE WAKES IN WRF

Wind turbine wakes and waking from nearby farms complicate estimations of the wind resource. Wakes are typically characterized by decreased wind speed and increased turbulence behind the rotor disk. Wind speed deficits caused by wakes can lead to decreased power production and thus lost revenue. Additionally, enhanced turbulence will increase mechanical loads on a turbine, which will decrease the lifetime of the turbine. Understanding and simulating these wind turbine wakes is imperative to accurately estimating and forecasting wind power production.

We test the Weather Research and Forecasting (WRF) model's Wind Farm Parameterization (WFP) using power production data from over 300 operating utility-scale wind turbines from four neighboring wind farms in the western US and address some of the challenges of doing this in complex terrain.

For a case study including a strong down-ramp in wind speed and thus wind power production, we find WRF predicts the down-ramp too early. Though this error in timing undermines the subsequent evaluation of the WFP, some data suggest the WRF-WFP possibly overestimates wake effects. Further work could include investigation of how vertical resolution, power curve choice, and site-specific density corrections could improve simulations of power production in complex terrain.

The following is adapted and reformatted from:

St. Martin, C. M., and Lundquist, J. K.: Simulating wind turbine wakes from multiple interacting wind farms in the western US using the WRF Wind Farm Parameterization, in preparation for Monthly Weather Review.

The reader is advised to seek out the accepted or published version for the final results and conclusions from this study.

Abstract

Characterizing wind turbine wakes and their effects on downwind turbines is important for integrating renewably-generated electricity into power grids by correctly predicting available wind power. In this study, we advance validation efforts of the Weather Research and Forecasting model's Wind Farm Parameterization (WRF-WFP). We employ meteorological observations, wind turbine power production data, and wind turbine nacelle observations from multiple wind farms located in the western United States at elevations above one kilometer. Data from four neighboring wind farms, including 348 turbines spread along a longitudinal distance of about 63 km, are available. Wind data from a 60-m meteorological tower upwind of the wind farm are also available. We simulate a case where we anticipate the largest wake effects, with upwind wind speed ranges from 5–11 m s^{-1} and when most, if not all, of the turbines are operating. WRF simulations with and without the current version of the WFP are compared. We find possible over-exaggeration of waking effects at wind speeds above 8 m s^{-1} from northerly wind directions, as well as early prediction of a down-ramp by WRF for the case simulated in this complex terrain. Subsequent evaluation of the role of vertical resolution, boundary conditions, and density variability may modify this conclusion.

1 Introduction

Driven by the need for cost-effective, renewable energy sources, wind power development continues to increase across the world. The Global Wind Energy Council (GWEC) estimates a new record of globally installed wind capacity–more than 63 GW–came online in 2015 (GWEC, 2016). As a result of increasing wind power of the grid, accurately estimating wind power production, from project siting to power validation and forecasting, is crucial to reducing the cost of the grid integration of wind (Giebel, 2003; Marquis et al., 2011; Wilczak et al., 2015). Forecasting wind speed ramps are especially difficult to model (Marquis et al., 2011) and are important as both excesses and deficits in power generation makes wind generation unattractive as a base load generator for grid operators.

Wind turbine wakes not only result in power losses due to velocity deficits (Baker and Walker, 1984), but can also be characterized by increased turbulence within the wake (Elliott and Barnard, 1990). Decreased wind speed and increased turbulence in the wake of a turbine can influence both power production and mechanical loads on individual turbines and within wind farms. Understanding single wakes as well as aggregate wakes can make a significant difference in production estimates as wakes from neighboring farms can reduce the resource for any downwind farms. Efforts made to further understand wakes and how they affect production include observational studies, large eddy simulations (LES) of wakes, and mesoscale modeling of wakes.

Observational studies give us insight into how these wakes vary with wind speed and atmospheric conditions. Elliott and Barnard (1990) found a linear relationship between the velocity deficit and downwind distance with maximum deficits occurring during lower wind speeds and higher turbulence. Other studies found the velocity deficit is the largest between

turbine cut-in wind speed and rated wind speed because of the variation in the thrust coefficient (Helmis et al., 1995, Barthelmie et al., 2007). Baker and Walker (1984) used kite anemometer measurements during nighttime conditions, and similar to Magnusson and Smedman (1994), found that during more turbulent conditions wakes dissipate more quickly than during less turbulent conditions. Using lidar measurements, Aitken et al. (2014b) found distinct wakes for stable and unstable conditions as well as turbulent conditions, and developed methods to determine the velocity deficit, size of the wake, and location of the wake centerline.

As towers and remote sensing instruments can be costly and logistically difficult to deploy within every wind farm, numerical modeling is a valid alternative to simulate wind farm wakes. Several approaches exist to parameterize the effect of wind plants within numerical models. Computational fluid dynamics (CFD) or large eddy simulations (LES) parameterize turbine drag on local flows and are useful to study the interaction of an individual turbine with the atmosphere (Calaf et al., 2010; Lu and Porté-Agel, 2011; Sanderse et al., 2011; Wu and Porté-Agel, 2013; Aitken et al., 2014a; Mirocha et al., 2014; Vanderwende et al., 2016).

Mesoscale models can also be used to study wind turbine wakes, however, with horizontal resolution on the order of 10s of kilometers, these models cannot resolve scales smaller than the grid size, and the effect of wind turbines must be parameterized. Mesoscale models either represent the effect of wind turbines by explicitly solving elevated drag and turbulent mixing (Baidya Roy et al., 2004; Blahak et al., 2010; Baidya Roy, 2011; Fitch et al., 2012; Fitch et al., 2013; Fitch, 2015; Jiménez et al., 2015) or implicitly parameterize the effect of wind turbines by increasing the roughness length to represent the turbines (Keith et al., 2004; Frandsen et al., 2009). However, increasing the roughness length to parameterize the effect of

wind turbine wakes has been found to exaggerate the wind and turbulence in the wakes (Fitch 2015) as well as the sensible heat fluxes (Fitch et al., 2013).

Though mesoscale models parameterize the effect of individual turbines, mesoscale model resolution can allow investigation into the impact and interaction of multiple turbines and farms. One such mesoscale model is the Weather Research and Forecasting model (WRF).Within WRF, the Wind Farm Parameterization (WFP) parameterizes the downwind effects of a wind turbine by both introducing a momentum sink on the mean flow and by transferring kinetic energy into both electricity and turbulence kinetic energy (TKE) (Fitch et al., 2012). Turbine drag is represented using the thrust coefficient (Fitch et al., 2012). User input to run this WFP in WRF includes locations of each wind turbine as well as a power curve and thrust coefficient curve for each turbine make and model.

The work presented here evaluates the WFP in existing wind farms in a region of complex terrain. Only one other validation of this parameterization can be found in the literature, which is a simulation of an offshore wind farm that reproduced power deficits (Jiménez et al., 2015). In Sect. 2, we describe the wind speed and power data from 348 turbines in four neighboring wind farm, the setup of our simulation in WRF, as well as the case study chosen for this study. In Sect. 3, we discuss the results. In Sect. 4 we make conclusions and suggest future work.

2 Methods

To evaluate the utility of including the Fitch et al. (2012) wind farm parameterization in wind energy forecasting simulations with WRF, we compare simulations to measurements, namely, wind speed and power data from over 300 wind turbines from four neighboring wind farms.

2.1 Observational data

Meteorological data from a 60-m tower approximately 11 km northwest of the wind farms of interest and at an elevation of about 1,491 m above sea level (ASL) include 5-min averages of wind speed and direction at 10, 30 and 60 m, as well as temperature, pressure, and humidity measurements at 10 m. The prevailing wind directions shown in the met tower data from 1 January 2011 through 29 July 2013 are northwesterly and southeasterly (Fig. 1). After filtering out spikes above 40 m s^{-1} in the wind speed data, wind speed and direction data at 60 m are available 78.6 % of the time.

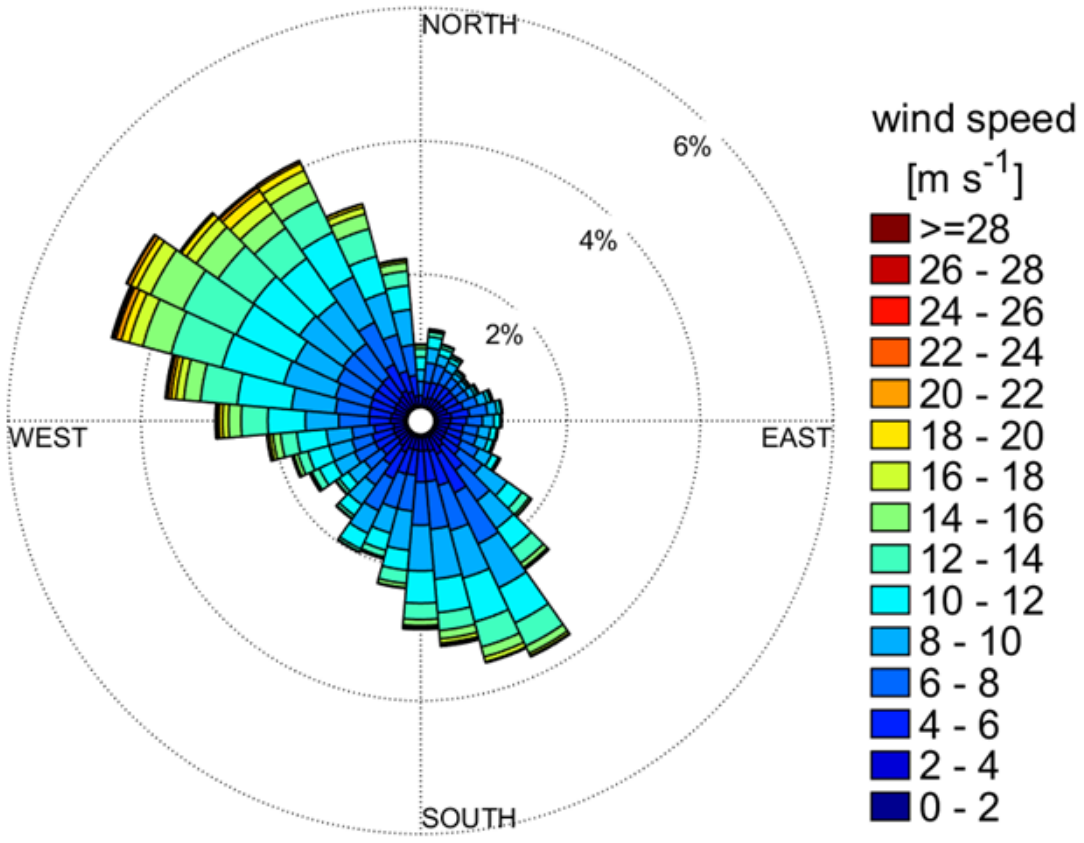

Figure 1. Wind rose using 60-m wind speeds and directions from the tower about 11 km upwind of the wind farms from 1 January 2011 through 29 July 2013.

Five-minute averaged hub-height wind speed and power data from 348 turbines from four wind farms in the western US are available from January 2010 through December 2013. Aside from a brief period in September of 2011, turbine data are generally available, with only a few turbines missing from most daily files. So as not to include curtailed turbines, we only include data from a wind turbine if the power data availability during the duration of the case study is at least 80%. The 348 turbines span about 63 km from west to east and about 11 km from south to north. The terrain surrounding these farms in the western US is complex with some vegetation and some smaller rocky ravines. The terrain elevation within the wind farms slopes upward towards the west and ranges from 1,279 m ASL to 1,475 m ASL. We have data from four wind farms, which include two different types of turbines all with hub heights close to 80 m: the GE1.5 sle with a 77 m rotor diameter (Turbine Type 1), and the Siemens 2.3 MW turbine likely with a 90 m rotor diameter (Turbine Type 2) (USGS).

The wind resource at a site is a driving factor for farm placement, however, there are other factors involved such as land permits, transmission costs, or mechanical loads concerns, which mean layouts can often be complex. In addition to complex farm layouts, other wind farms are often nearby, further adding to the complexity of the resource the turbines actually experience. Terrain and turbine layout, combined with the data from multiple neighboring wind farms, allow further testing of the WRF-WFP and perhaps more insight into how wakes interact across multiple wind farms in complex terrain (Fig. 2).

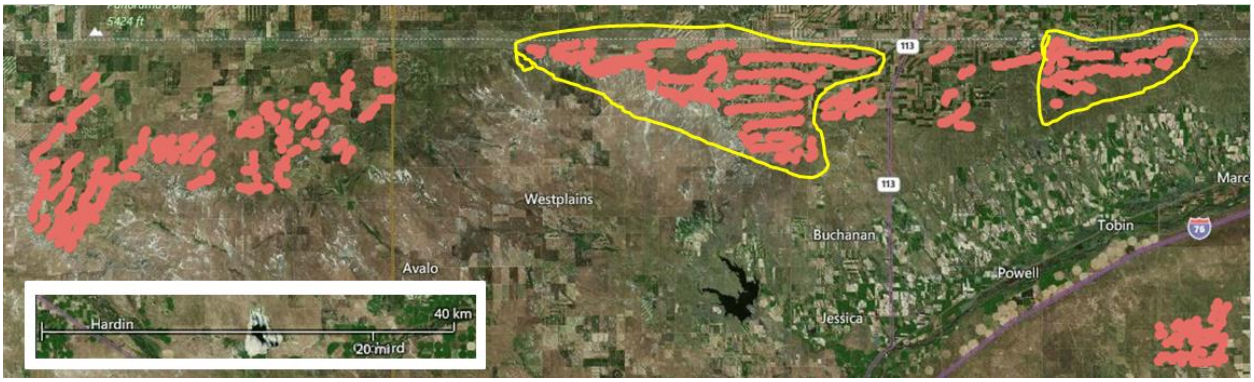

Figure 2. Map of the wind farms of interest as well as surrounding wind farms. The yellow outlines the wind farms simulated in this work. A distance legend is in the bottom left corner. Courtesy of USGS and Bing.

2.2 Case study

To test the performance of the WFP in simulating power produced and wake effects within these four neighboring wind farms, we focus on a case study when: (1) the 60-m tower measures wind speeds between cut-in and rated speed, (2) the 60-m tower measures wind directions which ensure these four wind farms are least affected by neighboring wind farms to the south and west, and (3) few turbine data are missing. We simulate a case study focusing on the nighttime stable hours during the early morning of 30 October 2011 into the daytime unstable hours of 30 October 2011. As temperature measurements are only available at one height on the met tower, atmospheric stability is determined by time of day. During these 12 hours, winds from the west ranged from about 5 to 11 m s^{-1} (Fig. 3a) and shear exponents calculated between 10 m – 60 m ranged from 0.02 to 0.44. The wind farms of interest may be waked by neighboring wind farms about 12 km to the west (Fig. 2) during the last few hours of the case study as wind directions range from west-south-westerly to northerly (Fig. 3d). A downramp in nacelle wind speeds leading to a drop in power generation occurs around 4am local time on Oct 30 (Fig. 3b-c).

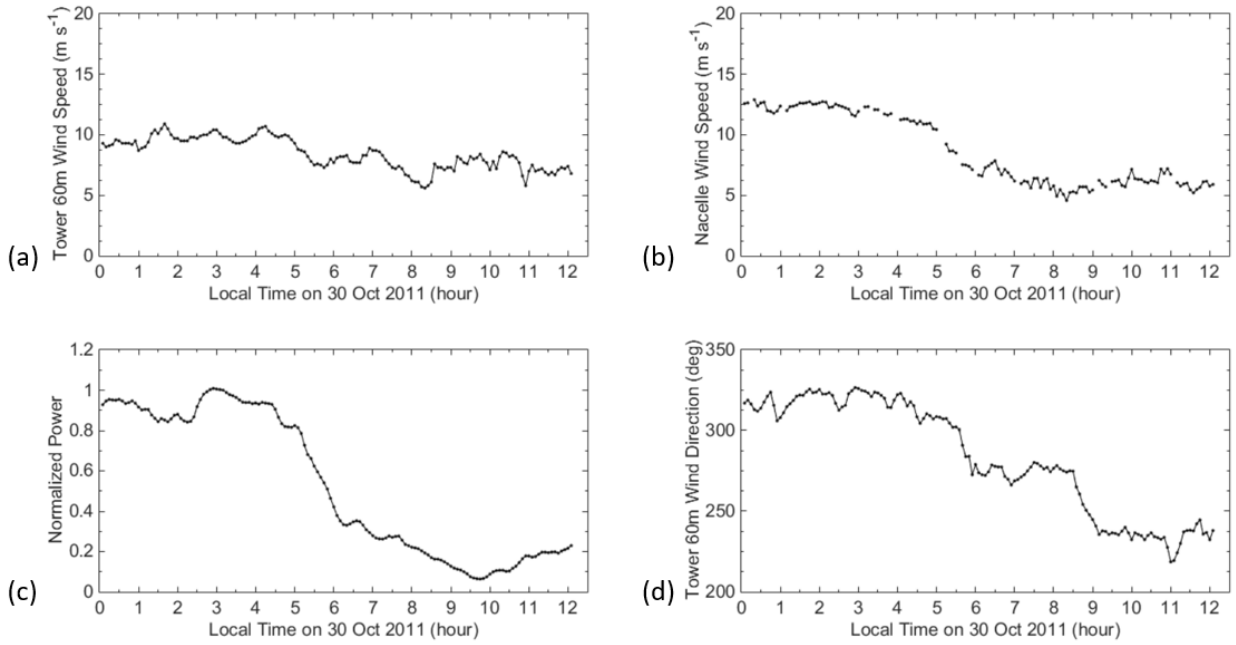

Figure 3. Time series from 00 LT on 30 October 2011 through 12 LT: (a) Wind speed time series from the 60-m met tower upwind of the wind farms. (b) Nacelle wind speed time series. (c) Normalized power observations from the wind farms. (d) Wind direction time series from the 60-m met tower upwind of the wind farms.

After filtering out turbines based on curtailment criteria listed in Sect. 2.1, 319 of the original 348 turbines remain. In addition, we discard times when the nacelle anemometers measure wind speeds outside of the mean wind speed over all turbines ± 3 σ so as not to include data when the anemometers could be malfunctioning. After filtering for the 319 turbines that were not curtailed during this case study as well as for when the nacelle anemometers were functioning correctly, 45,217 5-minute periods are left, or about 92 % of the original systems control and data acquisition (SCADA) data from this time period. Using these five-minute averaged power and nacelle wind speed measurements, observed power curves for this case study for the 319 turbines with data available and unaffected by curtailments (Fig. 4) show variability in power output at most wind speeds, and likely outside of their respective manufacturer power curves. Note that there are two wind farms with approximately 100 turbines

located in the middle of the farms of interest for this work (Fig. 2), which could create wakes for the eastern wind farms during cases with northwesterly flow.

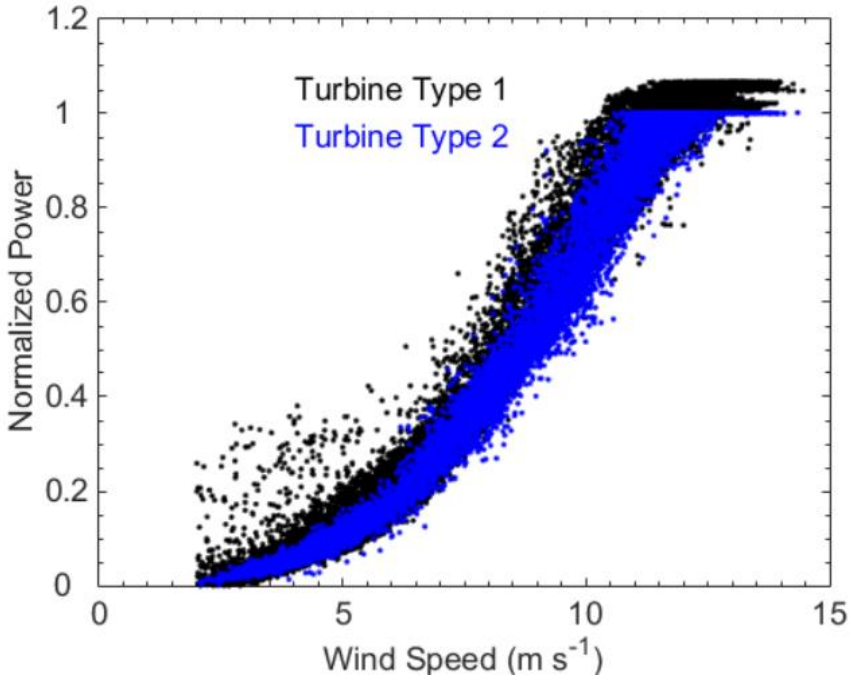

Figure 4. Power output normalized by rated power vs nacelle wind speeds for 319 turbines during the case study. Different color scatter points represent different turbine make/models.

The wind speed and power data from the 319 turbines that passed the curtailment criteria show the influence of wakes within these wind farms. To illustrate wake effects seen only from the observed wind speed and power data, averaged over the first six hours of the case study on 30 October 2011, for example, the largest power output is produced on the northern edge of the group of western farms and within the western group of turbines (Fig. 5a). These locations of higher power correlate with locations of wind speed near rated (Fig. 5b). Turbines on the southern edge of the farms observe lower wind speeds, possibly resulting from wake effects from the turbines to the north, which undermine power production.

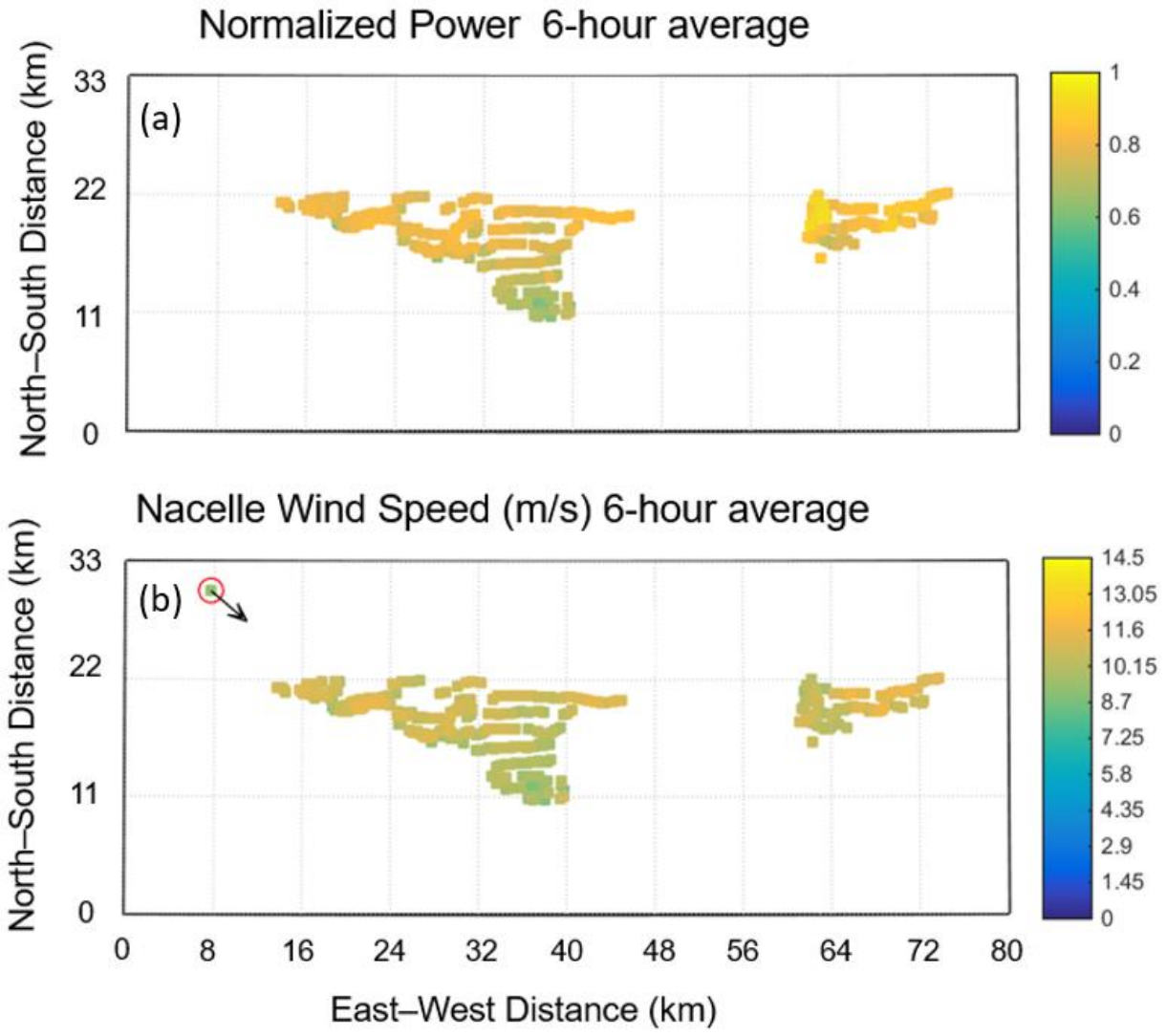

Figure 5. Six-hour average of winds and power production at from 00 LT to 6 LT on 30 Oct 2011. (a) Normalized power output from 319 turbines. (b) Nacelle wind speed from the turbines and 60-m wind speed and direction from upwind tower. The location of the tower is noted by the red circle.

2.3 Model setup

We use the WRF Model's version 3.8.1 to simulate wakes within the four neighboring wind farms in the western US during a 12-hour period spanning the stable early morning hours of 30 October 2011into the unstable daytime hours of 30 October 2011. The simulations begin on 29 October 2011 at 1800 UTC to allow 12 hours of spin-up time, and end on 30 October 2011

at 1800 UTC. Boundary conditions are provided by the ERA-interim dataset. The outer domain has a horizontal resolution of 8.910-km and the innermost nested domain has a 990-m resolution (Table 1). The innermost domain is centered on the location of the wind farm (Fig. 6). The integration time step is 15 s. The vertical resolution is approximately 22 m below 300 m and stretches above 300 m to include 69 layers in total. Four layers intersect the rotor diameter of the turbines. Terrain elevation within the innermost domain varies from about 400 m to about 4,130 m as seen in Fig. 7, although elevation within the wind farm itself varies from about 1,279 m to 1,475 m.

Table 1. Number of grid cells for each domain and horizontal resolution.

Domain	Number of grid cells in X	Number of grid cells in Y	Horizontal resolution (m)
1 (outer)	410	400	8,910
2	391	331	2,970
3 (inner)	802	592	990

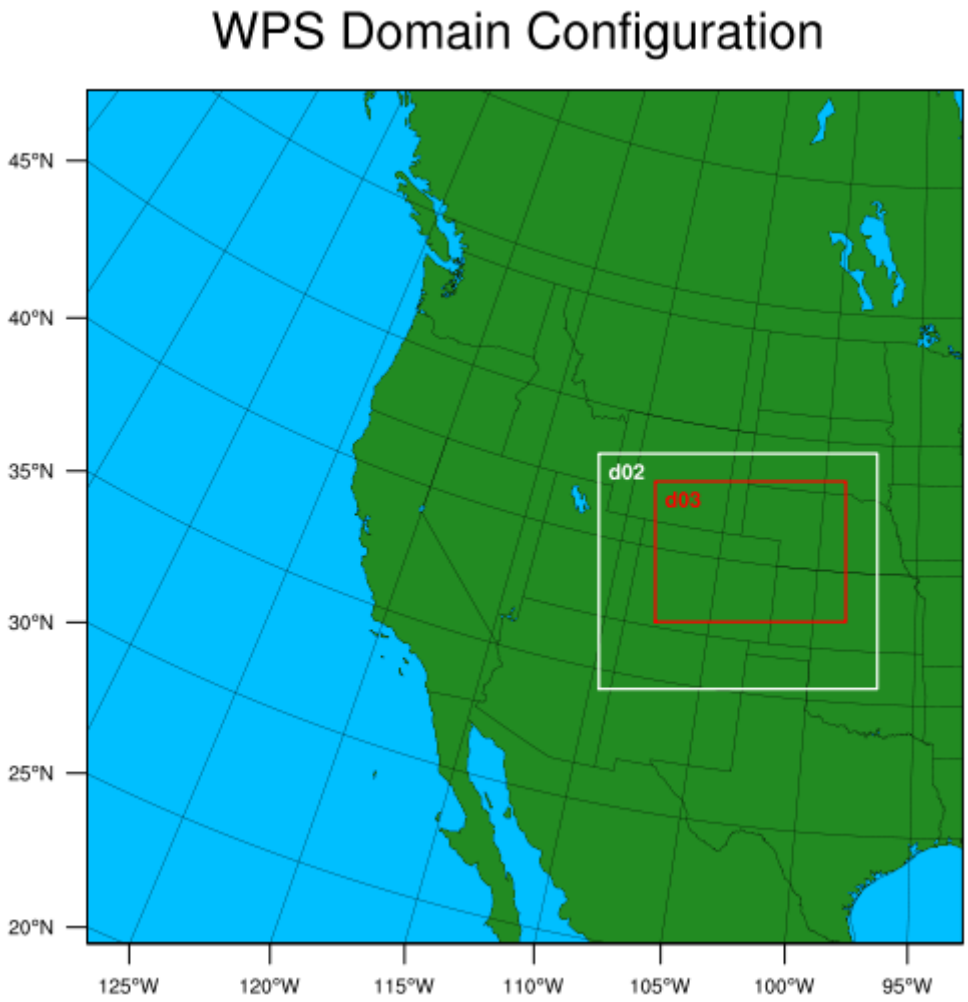

Figure 6. Outer domain and two nested inner domains of WRF runs.

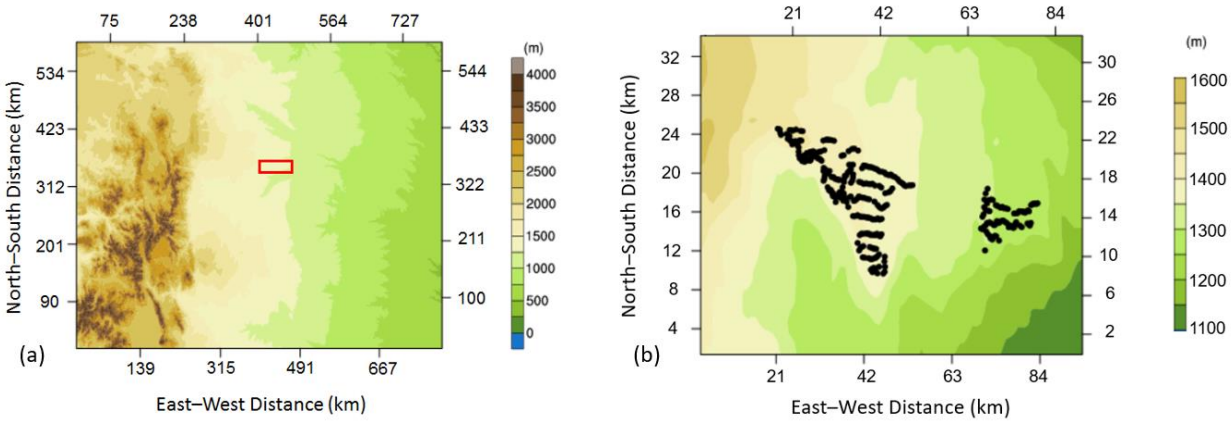

Figure 7. (a) Inner nested domain with terrain elevation. The red box denotes the location and extent of the wind farms. (b) Zoomed in on (a)'s red box to depict terrain elevation nearby; the turbines appear as black dots. Note that the aspect ratio in (b) is not 1:1.

The MYNN level 2.5 planetary boundary layer (PBL) scheme must currently be used to implement the WFP (Nakanishi and Niino, 2006). The microphysics scheme chosen is the aerosol-aware Thompson scheme (Thompson and Eidhammer, 2014), while the longwave and shortwave radiation schemes used the RRTMG scheme (Iacono et al., 2008). The simulations also used the unified Noah land-surface model (Elk et al., 2003) and for cumulus parameterization used the Kain-Fritsch scheme (Kain, 2004).

As described in Sect. 2.1, we only include a wind turbine if the observed power data availability during the 12-hour duration of the case study is at least 80%, so as not to compare curtailed turbines to our WRF-WFP simulations. Filtering out turbines for curtailments leaves 319 turbines to be simulated with the WRF-WFP. We use a power and thrust curve from a GE 1.5 sle in the WFP, and compare that normalized power curve to normalized power production from the real turbines. The number of wind turbines per grid cell varies from 1 to 5, with some of the more highly populated grid cells on the western side of the farms (Fig. 8).

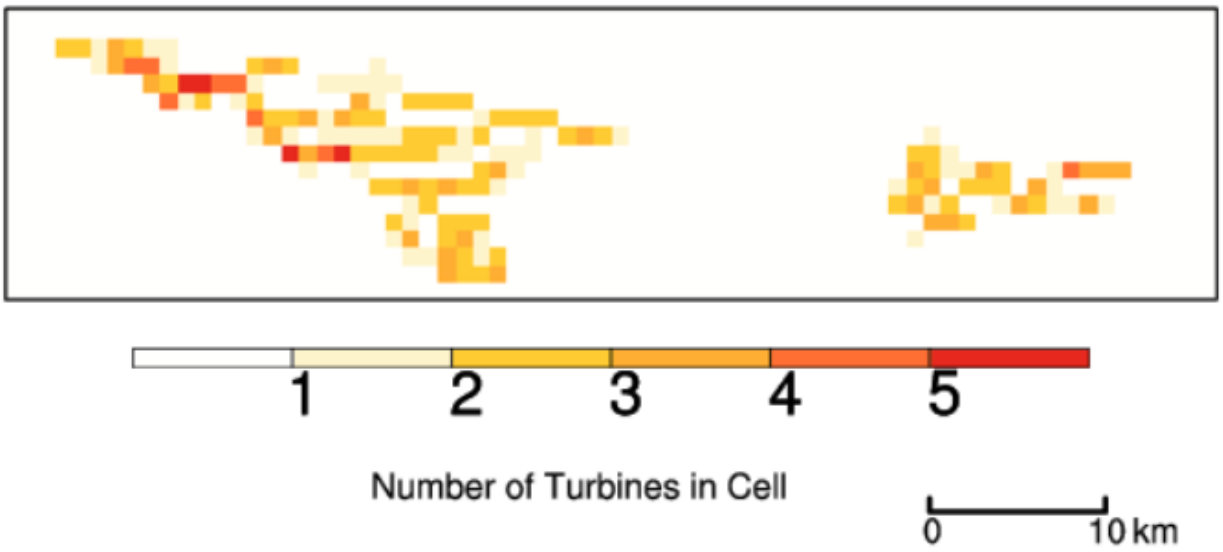

Figure 8. Number of turbines per 990-m x 990-m grid cell.

To compare the power output across the observations and simulations, we use the power data from the SCADA of the turbines as well as wind and power output from the WRF simulations. Observed power output is aggregated and normalized by rated power. The WRF-WFP power output is also summed and normalized by rated power of the simulated turbine (GE.15 sle). We also take the hub-height horizontal winds, calculated from the WRF output with the WFP turned off, and convert to power based on the same power curve used to run WRF with the WFP turned on.

3 Results

Maps of hub-height winds from the WRF output with (Fig. 9a) and without the WFP (Fig. 9b) highlight differences between the outputs. Wind speed differences are calculated as WRF-WFP winds minus WRF-noWFP winds (Fig. 9c); thus, we expect negative differences downwind of the wind farms to highlight wind speed deficits simulated by the WRF-WFP. Rather than a clear downwind wake signature, however, both accelerations and decelerations occur downwind of the wind farm, contrary to what has been observed in flat terrain (Fitch et al. 2013a) or offshore (Jimenez et al. 2015). These widespread accelerations and decelerations may be explained by recent work (Rai et al., 2017), in which oscillatory behavior was observed in the simulated wind speed for all horizontal resolutions less than 1.2 km when using the MYNN boundary layer scheme in WRF.

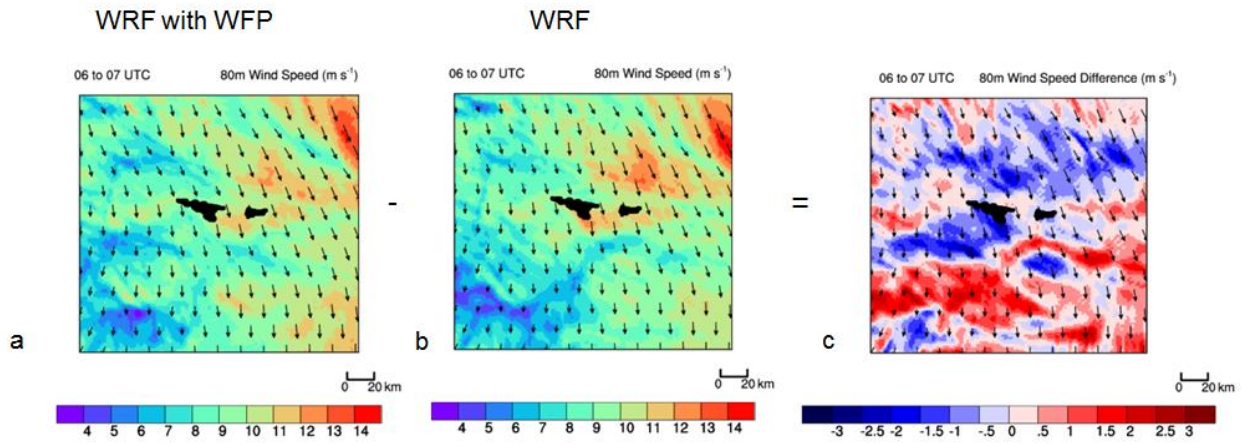

Figure 9. For the hour of 06 UTC to 07 UTC on 30 October 2011: (a) hub-height wind speed from WRF with the WFP; (b) hub-height wind speeds from WRF without the WFP; (c) differences in hub-height wind speeds. The black arrows represent hub-height wind direction from WRF with no WFP (a,c), WRF with the WFP (b).

Throughout all 12 hours of the simulation, there are both reductions in wind speed, as well as increases in wind speed downwind of the wind farms (Fig. 10). This inconsistency is not due simply to spatial scale, as seen in the focused map of hub-height wind speed differences (Fig. 11). Even with this focus on a more refined region immediately in the vicinity of the wind farm, inconsistent wakes and accelerations occur downwind of the wind farms. Wind speeds at the surface exhibit similar behavior while differences are smaller in magnitude (Fig. 12). While observations have indicated some warming at the surface at night due to wind farm effects (Zhou et al., 2012; Rajewski et al., 2013), no distinct pattern emerges in surface temperature differences in these simulations (Fig. 13).

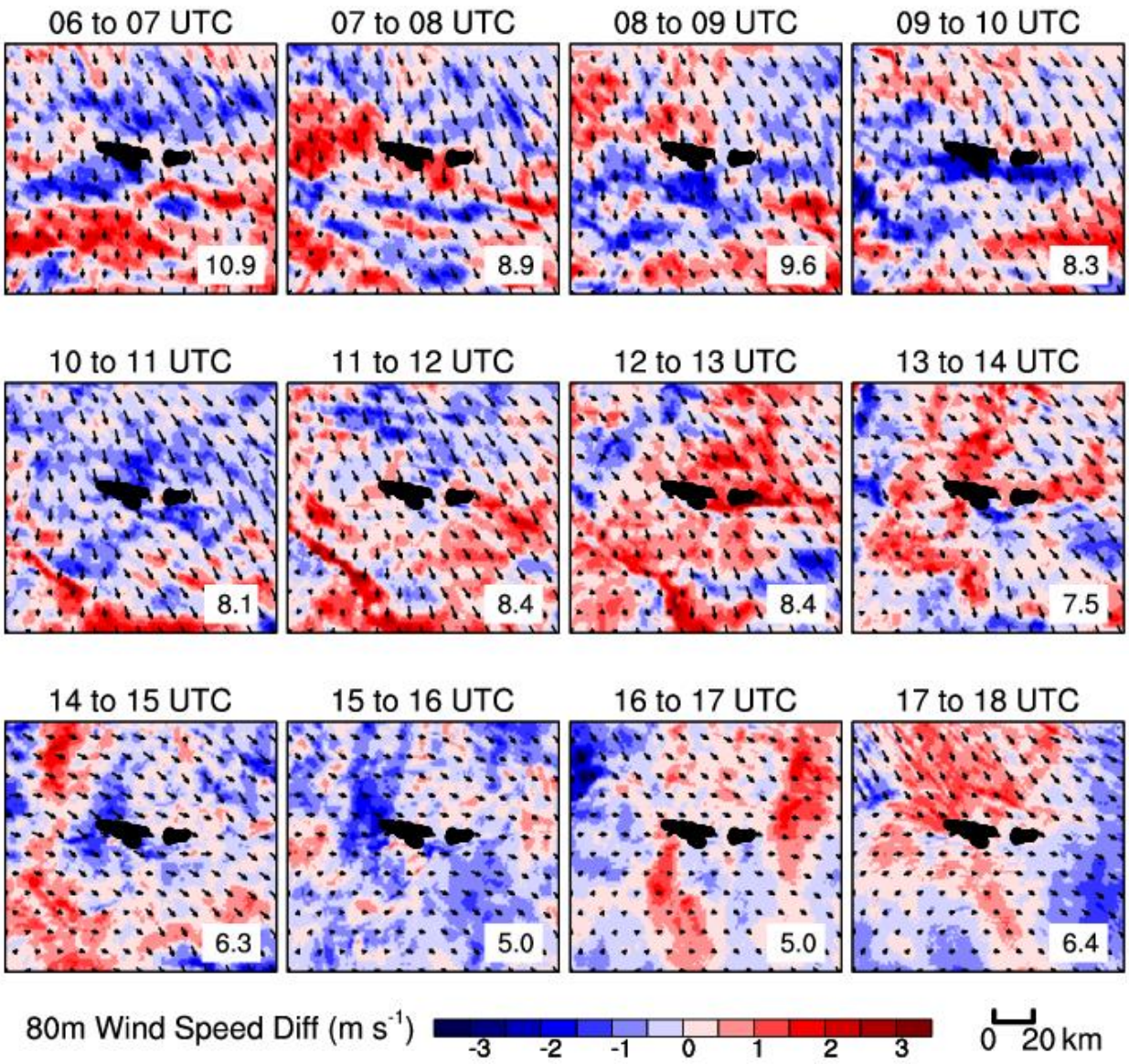

Figure 10. Differences in hub-height wind speed between WRF with no WFP and WRF with the WFP. The black dots represent the locations of the individual turbines. The white boxes on the bottom right corners of each plot contains a hub-height wind speed upwind of the wind farm. The black arrows represent hub-height wind direction from WRF with no WFP.

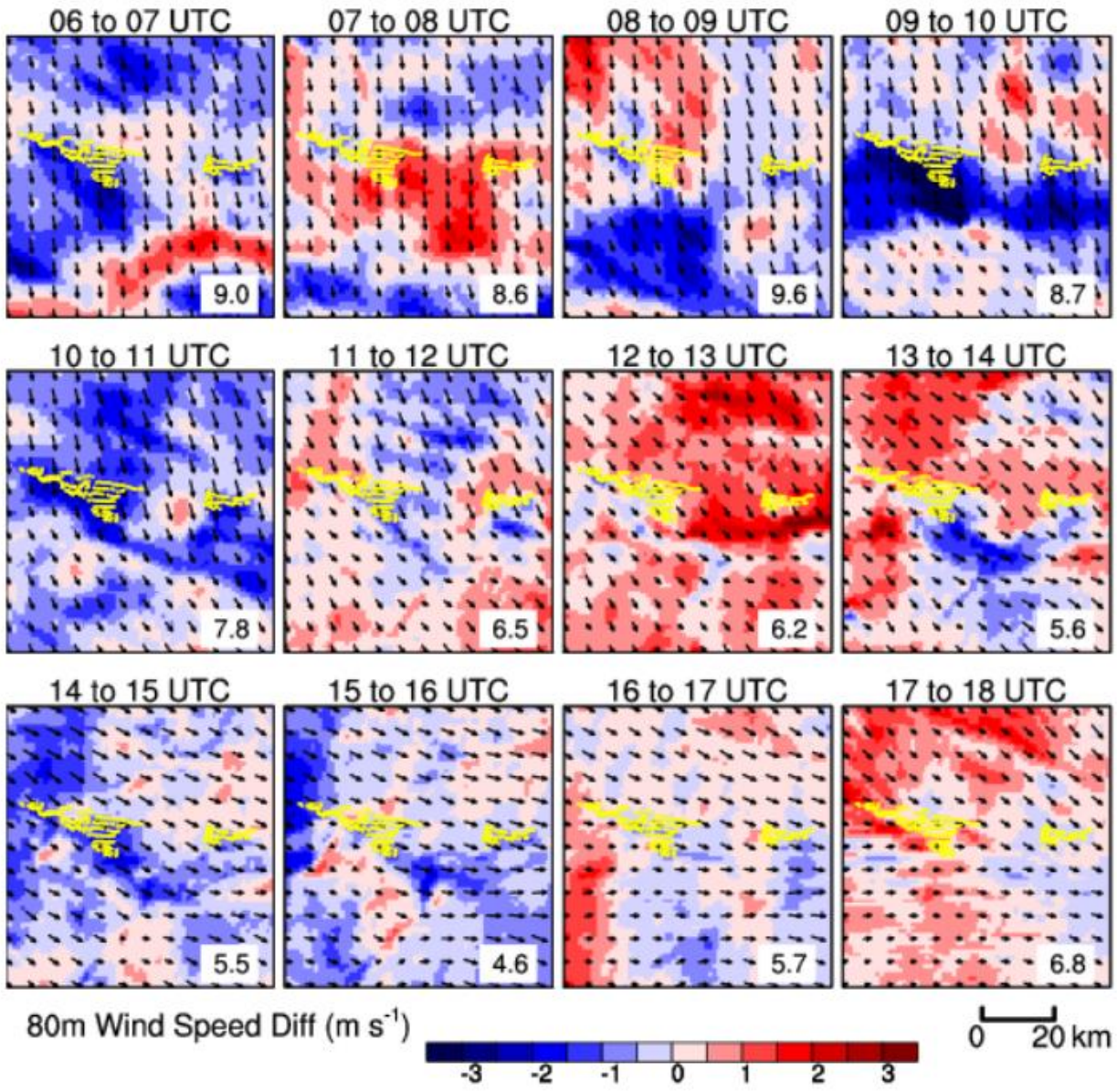

Figure 11. Differences in hub-height wind speed between WRF with no WFP and WRF with the WFP. The yellow dots represent the locations of the individual turbines. The white boxes on the bottom right corners of each plot contains a hub-height wind speed upwind of the wind farm. The black arrows represent hub-height wind direction from WRF with no WFP.

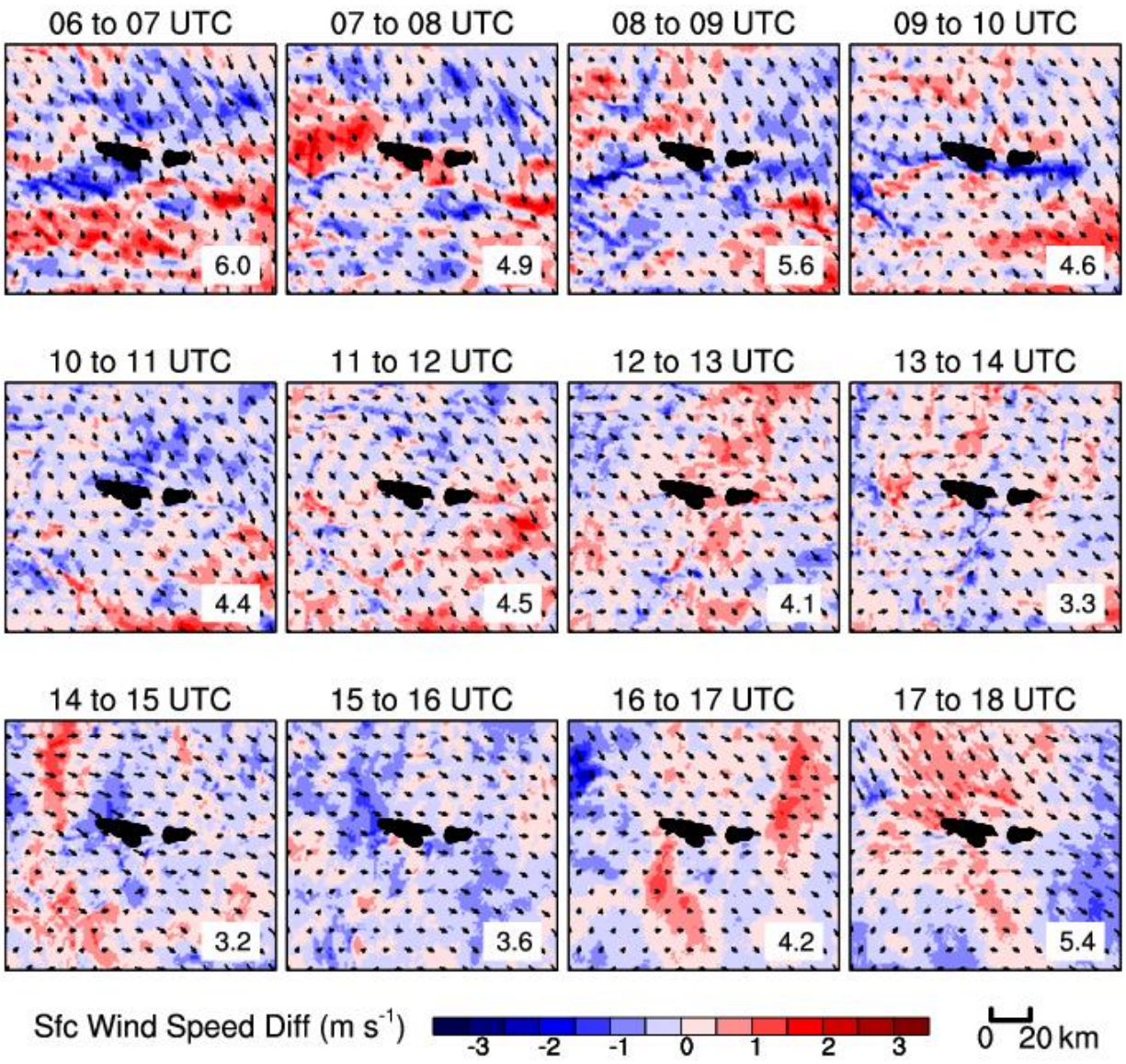

Figure 12. Differences in surface wind speed between WRF with no WFP and WRF with the WFP. The black dots represent the locations of the individual turbines. The white boxes on the bottom right corners of each plot contains a surface wind speed upwind of the wind farm. The black arrows represent wind direction at the surface from WRF with no WFP.

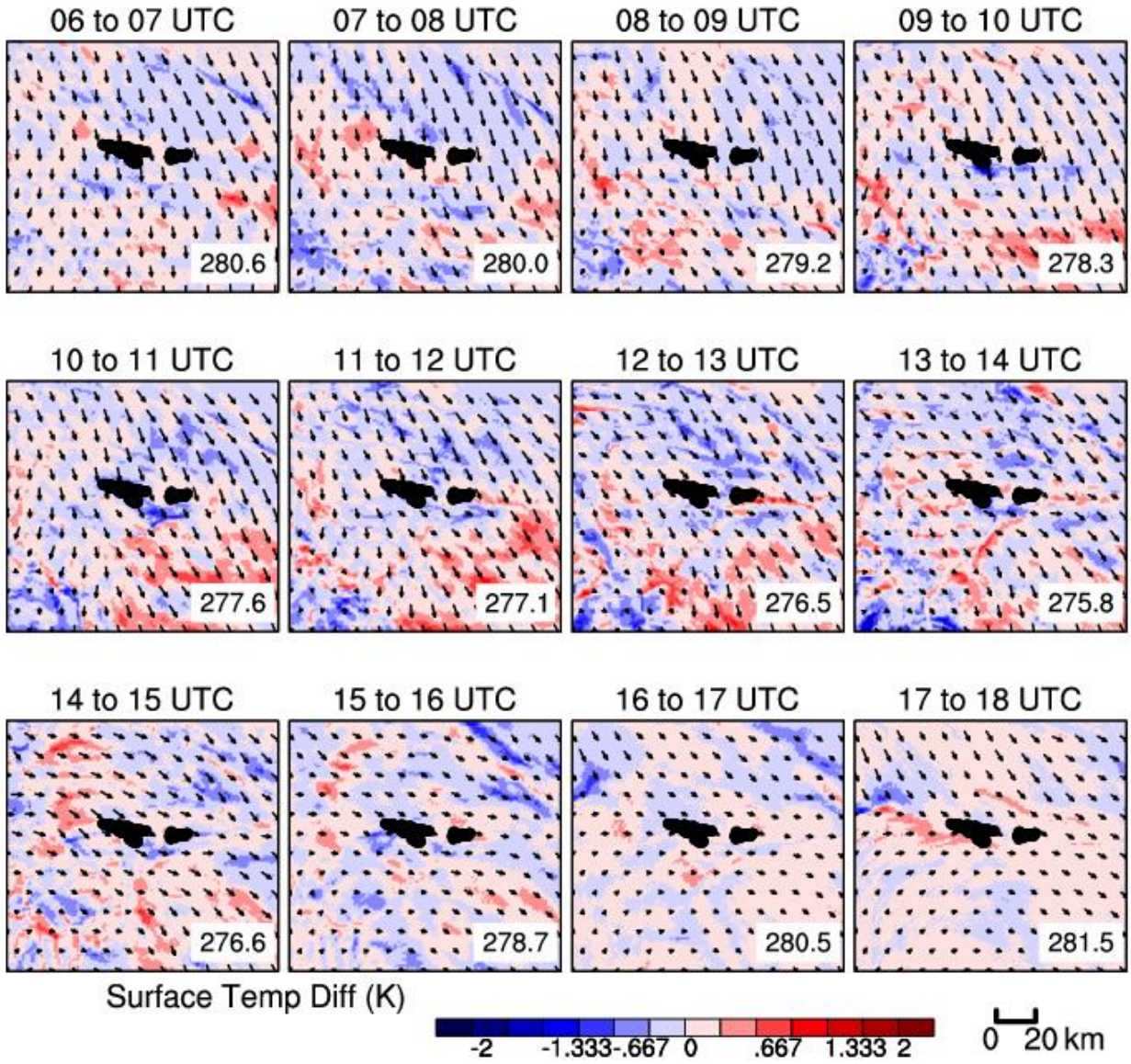

Figure 13. Differences in surface temperature between WRF with no WFP and WRF with the WFP. The black dots represent the locations of the individual turbines. The white boxes on the bottom right corners of each plot contains a surface temperature upwind of the wind farm. The black arrows represent wind direction at the surface from WRF with no WFP.

Power time series from the observations (Fig. 3c) as well as from both the output from WRF with the WFP and without the WFP reveal a significant drop in power output in the early morning hours of Oct 30, which WRF captures, but WRF predicts the drop in wind speed too early (Fig. 14). The WFP simulation performs worse than the simulation without the WFP: the

RMSE of the normalized power output without (with) the WFP is 0.1039 (0.1925) with a Pearson correlation coefficient of 0.9683 (0.9010).

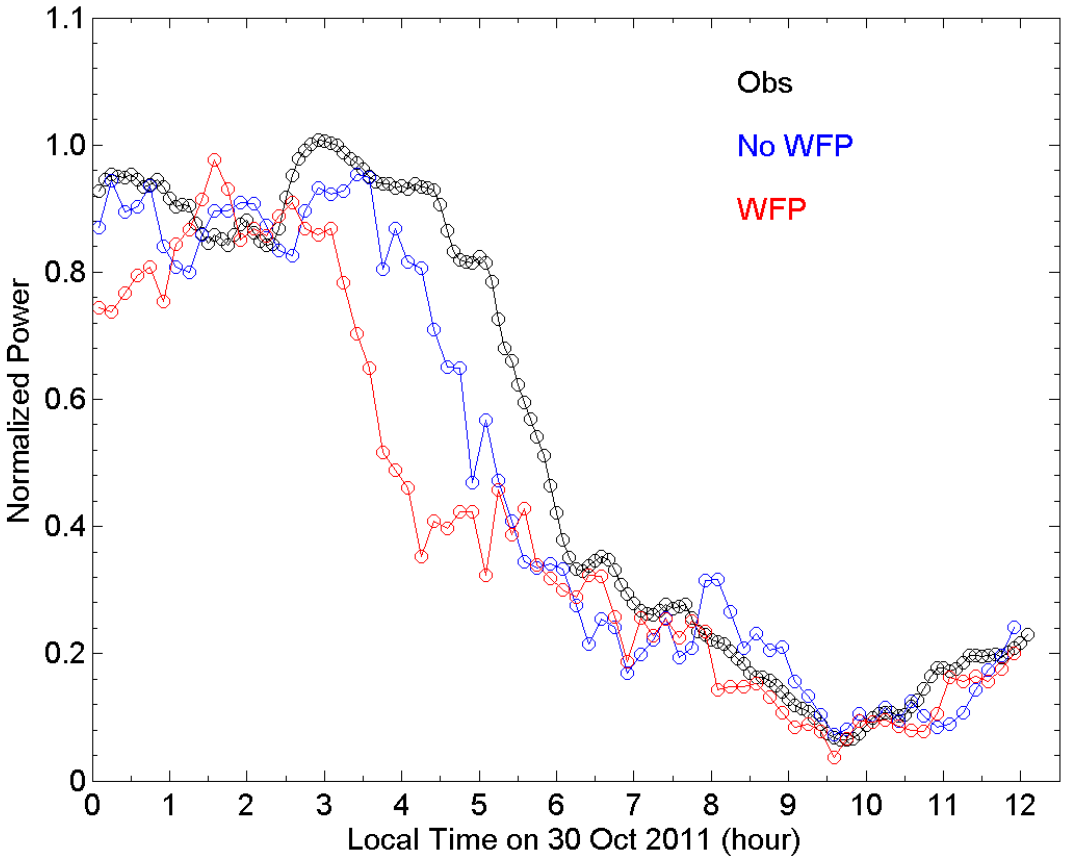

Figure 14. Time series of normalized total power output over all turbines. The black line represents the power time series from the SCADA from the wind turbines. The blue line represents the power time series from WRF with the WFP turned off, which is hub-height wind speeds projected on a GE 1.5sle power curve. The red line represents the power time series from WRF with the WFP tuned on, which is an output of the simulation.

The differences between the power time series from the observations and from the WRF simulations indicate that both simulations predict a down-ramp sooner than observed, possibly caused by some instability, seen north of the wind farms in the first few panels of Fig. 11. This offset in timing can be addressed by shifting the observations forward in time. Even with this shift, the simulations without the WFP perform better. The optimal shift for the WRF-no WFP

simulation is 30 minutes, resulting in a Pearson correlation coefficient of 0.9793 and RMSE of 0.0748, as seen in Fig.15. Even with this shift, the output from the WRF-WFP still predicts the down-ramp too early. Shifting the observations forward 1 hour and 25 mins (Fig. 16) results in a maximum Pearson correlation coefficient of 0.9637 between the observations and the WRF-WFP. The RMSE of WRF with no WFP with this time shift of 85-mins is 0.1211 and the RMSE of WRF with the WFP turned on with this time shift is 0.0971.

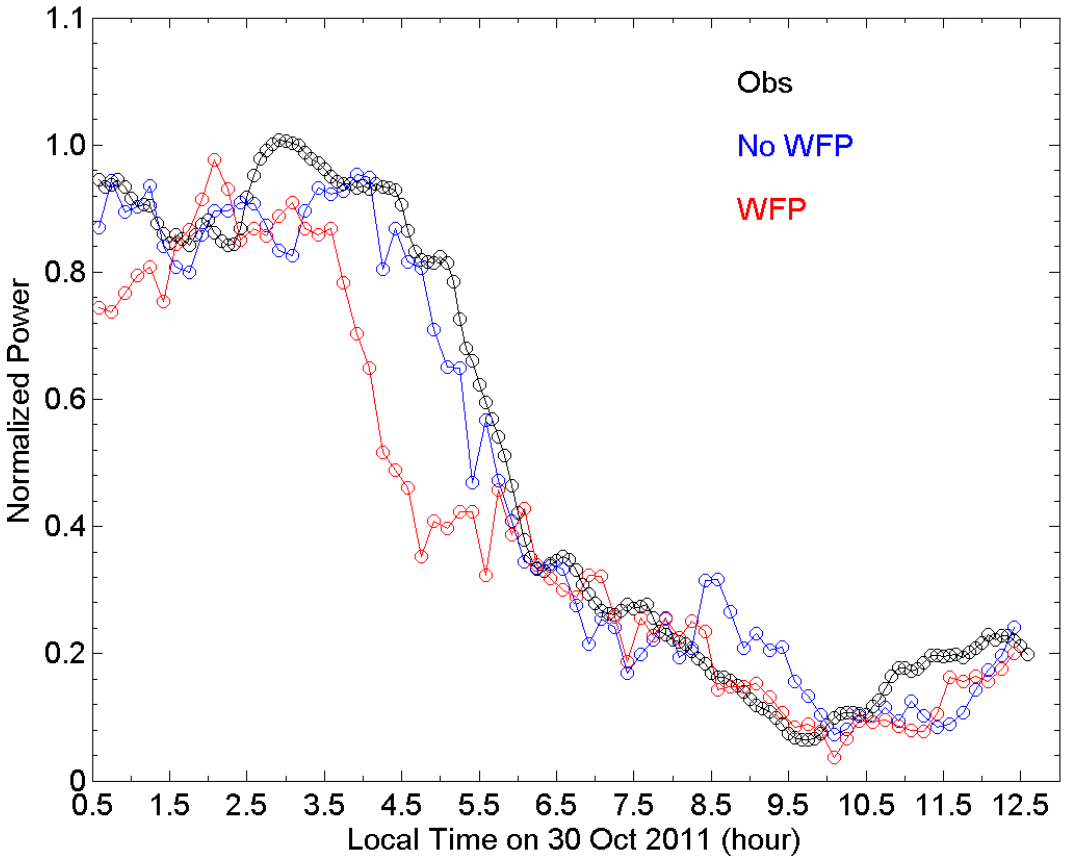

Figure 15. Time series of normalized total power output over all turbines with the observations shifted forward 30-mins to better match the WRF results. The black line represents the power time series from the SCADA from the wind turbines. The blue line represents the power time series from WRF with the WFP turned off, which is hub-height wind speeds projected on a GE 1.5sle power curve. The red line represents the power time series from WRF with the WFP tuned on, which is an output of the simulation.

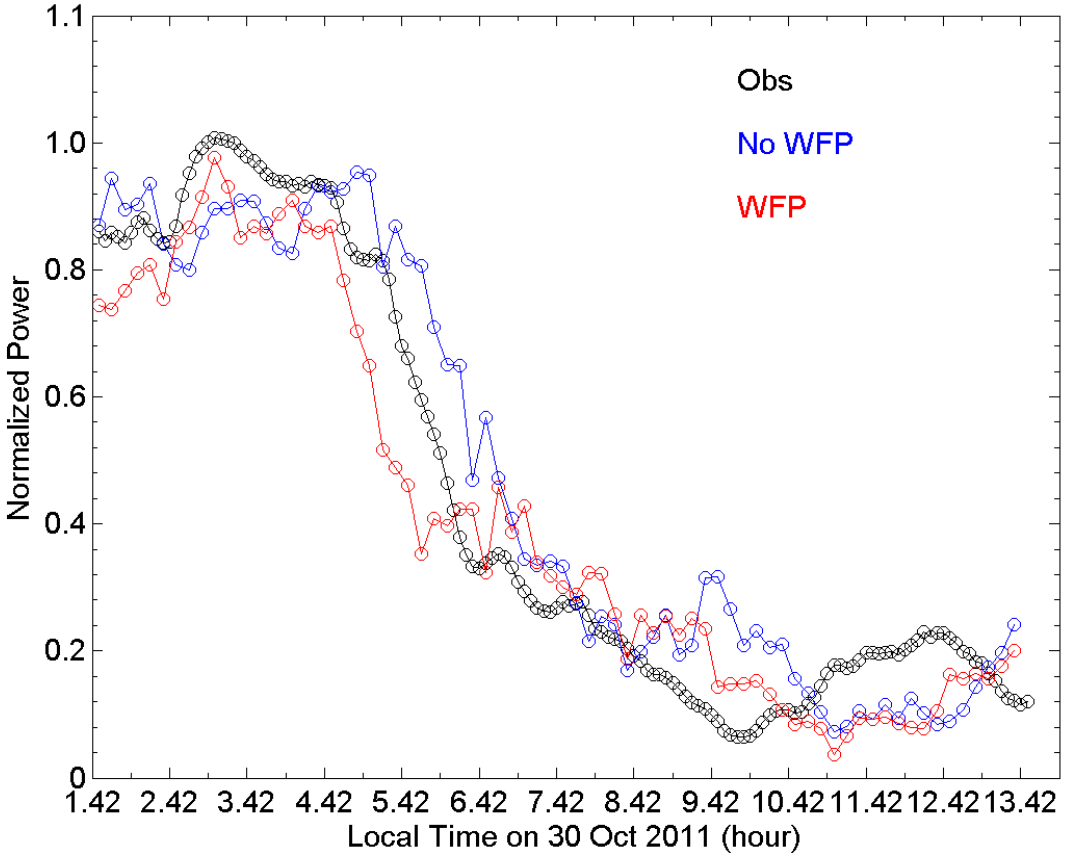

Figure 16. Time series of normalized total power output over all turbines with the observations shifted forward 85-mins to better match with the WRF-WFP results. The black line represents the power time series from the SCADA from the wind turbines. The blue line represents the power time series from WRF with the WFP turned off, which is hub-height wind speeds projected on a GE 1.5sle power curve. The red line represents the power time series from WRF with the WFP tuned on, which is an output of the simulation.

The WRF-WFP simulations result in larger differences in normalized power output from observed normalized power at higher wind speeds and more northerly directions, suggesting the WRF-WFP may be overestimating or exaggerating waking effects. At wind speeds less than 8 m s^{-1}, errors in normalized power predicted by WRF and WRF-WFP compared to actual normalized power production vary from about -0.2 to 0.1. However, at wind speeds above about 8 m s^{-1}, errors increase for the WRF simulations to about -0.4 and for the WRF-WFP simulations

to about -0.6 (Fig. 9a). In contrast, differences in normalized power predicted by WRF-WFP versus power produced range from about -0.6 to 0.1 when winds are from the north, while differences in from WRF only range from about -0.3 to 0.1 at most wind directions (Fig. 9b). Turbine layout does not explain the larger deviations when winds are form the north because turbines are closer together in the E-W direction, not in the N-S direction.

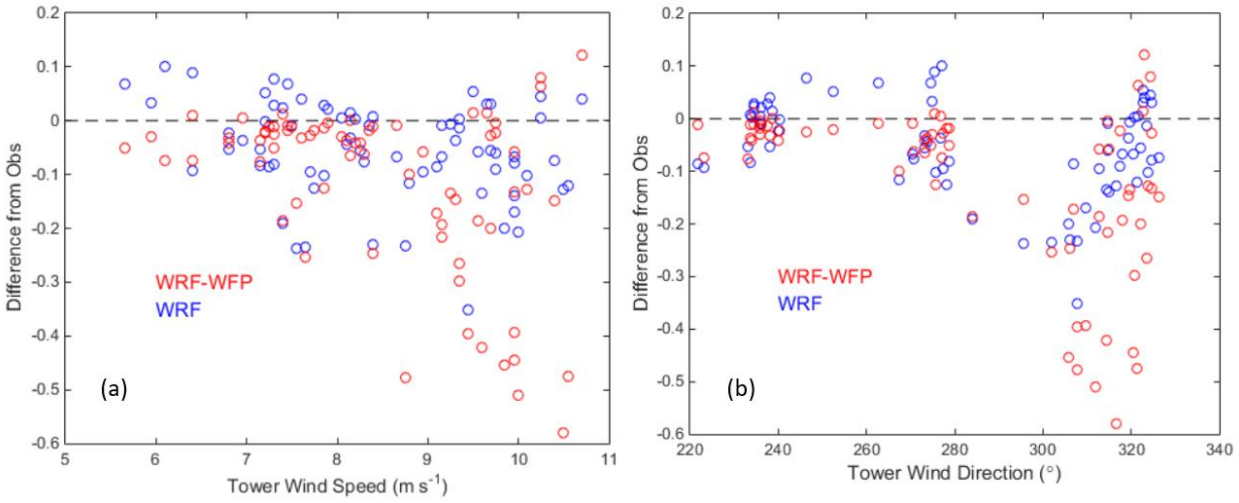

Figure 17. (a) Difference in normalized power vs upwind tower wind speed for 12-hour study, with one data point for each 5-min interval. Blue circles denote WRF and red circles denote WRF-WFP. (b) Difference in normalized power vs upwind tower wind direction for 12-hour study.

Comparisons between WRF-predicted power and observed normalized power reveal the effects of the early prediction of the down-ramp by WRF. Deviations in normalized WRF-simulated power from normalized observed power are larger; from about 0.4 to about 0.8 (Fig. 18).

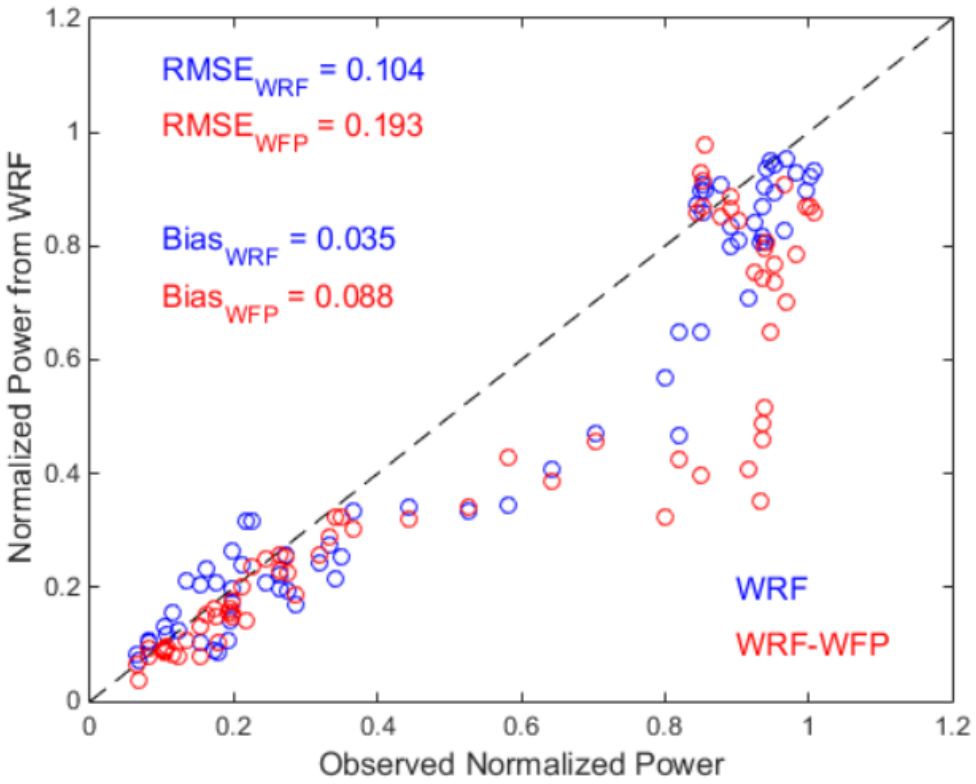

Figure 18. Normalized power as predicted by WRF vs observed normalized power. Blue circles represent results from WRF and red circles represent results of WRF-WFP.

4 Conclusions

We use power data from the systems control and data acquisition (SCADA) system on 319 turbines from four neighboring wind farms to assess the ability of the Weather Research and Forecasting Model's Wind Farm Parameterization (WRF-WFP) to forecast wind power production in complex terrain for a down-ramp case spanning the first 12 hours of 30 October 2011. We conduct simulations with and without the WFP.

A strong down-ramp occurs during this time period, the timing of which both WRF and WRF-WFP predict too early. Errors in predicted power production show possible exaggerations of waking effects by the WRF-WFP at wind speeds above 8 m s^{-1} and northerly wind directions at this site. Differences between WRF with and without the WFP in hub-height wind speed,

surface winds, and surface temperature emerge throughout the inner domain, and vary downwind of the wind farms. These comparisons between observations, WRF runs, and WRF-WFP runs, reveal that there may be some instability upwind of the farms introduced early in the study period resulting in differences throughout the domain between WRF with the WFP and WRF without the WFP. Differences throughout the domain between WRF and WRF-WFP results could also be the result of the 990-m horizontal resolution of these simulations, as Rai et al. (2017) found oscillations in wind speed for horizontal resolutions less than 1.2 km when using the MYNN boundary layer scheme. Power output from the WRF-WFP is ahead of the observations by about 85 minutes, while power output calculated from hub-heights winds from WRF without the WFP is only ahead of the observations by about 30 minutes. The early prediction of the down-ramp by WRF results in differences in predicted power versus observed power.

Further investigation into why the WFP is not working optimally could include several tests to see if additional changes may bring the WFP results closer to the observations. As the down-ramp observed in this case study likely propagated error in the simulations, a longer case study without a down-ramp could be simulated to mitigate the added challenge of simulating a down-ramp in complex terrain. The horizontal resolution of the innermost domain should be greater than 1.2 km to avoid numerical artifacts as seen in Rai et al., (2017). Another change could be using a second power and thrust curve in the WFP for the 66 Siemens 2.3 turbines in the farm. Currently, a power and thrust curve for GE 1.5sle is used for all the turbines, but perhaps the difference in the Siemens 2.3 thrust curve would change the results. Other datasets for boundary conditions, such as the GFS dataset, could also change the results. And finally,

adjusting the power curve used in the WFP for a more location-specific density may result in the WFP producing more accurate power predictions.

Acknowledgements

We would like to acknowledge high-performance computing support from Yellowstone (ark:/85065/d7wd3xhc) provided by NCAR's Computational and Information Systems Laboratory, sponsored by the National Science Foundation. This work was partially supported by the National Science Foundation grant BCS-1413980 (Coupled Human Natural Systems). We express appreciation to the National Center for Atmospheric Research (NCAR) who provided access to these data in support of subcontract Z10-86199, as well as the data contributions of the utility company.

CHAPTER VI

CONCLUSION

Technical

A deeper knowledge of the interaction between wind energy and the atmospheric boundary layer could improve upon the efficiency of processes involved in the manufacturing of turbines, siting and development of wind plants, and operation of wind plants. As a part of my PhD research, I explored several of these possible improvements, including (a) mitigating wind power variability on the grid by aggregating wind farm power production, (b) improving power production validation by demonstrating the value of calculating different power curves for different atmospheric and turbulence regimes, (c) quantifying the skill of nacelle-mounted anemometers for power production validation using empirically-derived nacelle transfer functions (NTFs) and further improving these NTFs by calculating different NTFs for different atmospheric stability and turbulence regimes, and (d) further validating the Weather Research and Forecasting Model's Wind Farm Parameterization (WRF-WFP) by evaluating model runs with power data from wind farms in complex terrain in the western US.

After introducing wind energy as a part of the clean energy portfolio needed for mitigating climate change, in the second chapter of this dissertation, I investigated "how far is far enough" for aggregating wind power plants to reduce the variability in power production. Using wind speed data from over 100 sites in Canada and 14 sites in the US Pacific Northwest as well as power generation data from 29 wind farms in southeastern Australia, we studied the dependence of correlation length between site pairs on timescales. After high-pass filtering the

data on 0.25–2000-hour timescales and calculating correlations between site pairs for each high-pass filter cut-off, we found that correlations fall to zero with increasing station separation distance. However, the characteristic correlation length varied with the high-pass filter: the higher the cut-off frequency, the smaller the distance between stations was required to become statistically uncorrelated. Since the site separation needed for statistical independence fell for shorter time scales, higher-rate fluctuations can be effectively smoothed by aggregating wind plants over smaller areas than otherwise estimated. We found similar behavior in all three datasets, which included years of both wind speed and power data, which suggests our results can be particularly useful for grid management.

In the third chapter, I investigated the effects of atmospheric stability and turbulence on wind turbine power curves and annual energy production (AEP) estimates. The dataset consisted of 2.5 months of upwind measurements from a 135-m meteorological tower as well as nacelle-based measurements from the supervisory control and data acquisition (SCADA) system on a GE 1.5MW turbine (GE 1.5/77 sle). We found that different power curves were produced for different stability and turbulence regimes: at lower wind speeds, low stability and high turbulence resulted in more power produced than high stability and lower turbulence. However, near rated wind speed, high stability and low turbulence resulted in more power produced than low stability and high turbulence.

In addition, after separating data depending on turbulence or stability regime, AEP results revealed different AEPs for different turbulence and stability regimes. AEP calculated with no atmospheric or turbulence filter was higher than any AEP calculated with these filters. The AEP calculated using a TI filter showed that the AEP calculated with the medium TI regime was greater than the AEP calculated with the low or high TI regimes, and the AEP calculated with the

R_B filter showed that the low regime AEP was much larger than the AEP in the high and medium regimes. Though small, these differences in AEP suggest that different power curves should be calculated for different atmospheric conditions, as even small deviations in AEP result in large deviations in cost of energy.

In the fourth chapter, I explored the use of nacelle anemometer measurements for power performance validation through the application of nacelle transfer functions (NTFs). Using the same met tower and turbine data as described in the third chapter, we calculated empirical NTFs with both fifth- and second-order polynomial fits. We found that the coefficient of determination of the fifth-order fit was only slightly higher than that of the second-order fit, though after correcting the nacelle winds using the fits, the deviations in the corrected wind speed from the upwind tower hub-height wind speeds increased at higher wind speeds. The higher coefficient of determination using the fifth-order polynomial fit suggested that the higher order NTF results in a better accurate representation of the upwind wind speed. The use of NTFs in AEP calculations resulted in a less than 1 % difference from the AEP calculated with the upwind met tower wind speed, suggesting that operators can use the nacelle anemometer as a reliable means of power production verification at this site.

In addition, we explored the utility of transfer functions segregated by turbulence intensity (TI) and turbulence kinetic energy (TKE) classifications. During periods with relatively high TI and TKE, the nacelle anemometer underestimated the ambient wind speed more than during periods of relatively low TI and TKE at wind speeds between cut-in and rated, suggesting different turbulence regimes warrant the application of different NTFs.

Finally, in the fifth chapter, I used wind speed and power data from 348 wind turbines at four neighboring wind farms to help validate the Weather Research and Forecasting Model's

mesoscale Wind Farm Parameterization (WRF-WFP), which represents aggregate effects of wind turbine wakes. Our case study focused on the early to midday hours of 30 October 2011, based on upwind 60-m tower wind speed and direction measurements which indicated wind speeds between cut-in and rated peed of a turbine representative of the farms, as well as wind directions unaffected from other neighboring wind farms. In addition to varying differences between WRF and WRF-WFP simulations throughout the domain possibly attributed to horizontal resolution, we observed a strong down-ramp in the early morning hours of 30 October 2011, which both WRF and WRF-WFP predict too soon. Further investigation into why the WFP is not working optimally may bring the WFP results closer to the observations.

In addition to the projects presented here, I have gained considerable experience with lidar data, field deployments, and field site forecasting. I evaluated lidar wind profiles in the complex terrain of Uttarakhand, India to validate WRF model output for wind resource assessment as part of an NREL technical report (Lundquist et al., 2013, http://www.nrel.gov/docs/fy14osti/61103.pdf), and took part in a number of field campaigns. During the fall of 2012, I forecasted wind speed and direction as well as the probability of strong turbulence at the National Renewable Energy Laboratory's National Wind Technology Center (DOE NREL-NWTC) for the Turbine Outflow Dissipation Study (TODS). In the summer of 2013, I joined the Crop Wind energy EXperiment (CWEX) to deploy lidars and a radiometer as part of the CU field team in Iowa. In the spring of 2015, I deployed lidars, surface flux stations, and radiosondes at the NOAA Boulder Atmospheric Observatory as part of the DOE eXperimental measurement campaign: Planetary boundary layer Instrumentation Assessment (XPIA). Finally, during the fall and winter of 2015–2016, I deployed and provided support for

lidars and radiometers along the Columbia River Gorge in Oregon and Washington as part of the DOE Wind Forecast Improvement Project Part 2 (WFIP2).

In conclusion, knowledge of atmospheric science can surmount challenges to the wind industry that prevent the industry from being as efficient and cost effective as possible. Future work could include analyzing data from turbine-tower pairs at several wind plant sites across both simple and complex terrain to see how turbulence- and stability-specific NTFs vary across different sites. Perhaps an operator doing power performance testing can take a set of NTFs from a site with similar characteristics, such as wind climates and turbine models, and use those NTFs at their site without the need to deploy a tower. Further, as most turbines in a plant are waked by at least one other turbine in some wind direction sector, calculating NTFs for a turbine waked by one or more turbines in different atmospheric conditions could help validate and forecast power production for non-leading edge turbines without the additional cost of a post-construction tower. Other work at the intersection of wind energy and atmospheric science could include investigating the use of nacelle-mounted lidars for the purpose of real-time turbine operation. If placed on the nacelle with the laser window facing the turbine rotor, lidars could measure out to distances of 200 m in front of the turbine rotor, possibly allowing control algorithms time to adjust based on the atmospheric conditions observed. If a nacelle-mounted lidar observed increased turbulence and decreased wind speed, indicative of wakes, a turbine controller could reduce loads by yawing out of the wake or feathering the blades. Finally, developing a universal, yet adjustable quality-control algorithm for cleaning wind data sets would be incredibly useful as virtually everyone uses their own algorithm, leading to either the inclusion of bad data or the discarding of good data and thus affecting the results. To increase the quality of the data used for analyses in all projects, besides regular instrument maintenance,

perhaps we should have an International Electrotechnical Comission (IEC) or International Energy Agency (IEA) working group, consisting of scientists and engineers from around the world in both academia and industry, collaborate to build guidelines for an all-inclusive quality control algorithm based on their collective experience.

A Personal Perspective

Throughout my academic experience and during two summers interning in the wind industry, I have observed a communication disconnect between industry and academia. This gap in communication can arise from time pressures and different intrinsic motivations, such as finishing a project for a customer, meeting a quota by the end of the fiscal quarter, or winning grants and publishing papers in an increasingly competitive academic environment.

To address this communication gap to the benefit of both academia and industry, both groups need to make an effort to attend conferences in order to share ideas and experiences as well as to make connections, seek out and pursue academic-industry collaborations, publish in open-access journals, and share, read, and discuss relevant peer-reviewed work. Academics with recent published work or work that might seem of interest to industry should reach out directly to possible industry collaborators. For proprietary reasons, industry is not likely to reach out to academia with a problem they would like to solve, but if informal or personal connections grow between the two groups, academics might have a better idea of who might be interested in their work and to what application it can ultimately be applied. Open dialog between industry and academic science and engineering should be prioritized by both groups; collaboration on mutually-beneficial projects can result in outcomes leading to a decreased cost of energy and increased profits. Increasing the number of industry internships available to graduate students,

such as I experienced, could also provide industry with the benefit of students' experience and knowledge of work in the scientific and engineering communities, and academia could benefit from students' experience and connections in industry, leading to research projects more applicable to real-world problems. Ultimately, we can only realize the full potential of the ideas and concepts academia discovers and builds on if those ideas are applied in industry.

REFERENCES

Achberger, C., Chen, D., and Alexandersson, H.: The surface winds of Sweden during 1999-2000, International Journal of Climatology, 26, 159-178, 2006.

Adams, T., and Cadieux, F.: Wind power in Ontario: quantifying the benefits of geographic diversity, Presented at the 2nd Climate Change Technology Conference, Hamilton, Ontario 1-15, 2009.

Aitken, M.L., Kosović, B., Mirocha, J.D., and Lundquist, J.K.: Large eddy simulation of wind turbine wake dynamics in the stable boundary layer using the Weather Research and Forecasting Model, Journal of Renewable and Sustainable Energy, 6, 033137, doi: 10.1063/1.4885111, 2014a.

Aitken, M.L., Lundquist, J.K., Pichugina, Y.L., and Banta, R.M.: Quantifying wind turbine wake characteristics from scanning remote sensor data, J. Atmos. Ocean. Tech., 31, 765–787, doi:10.1175/JTECH-D-13-00104.1, 2014b.

Aitken, M.L., Rhodes, M.E., and Lundquist, J.K.: Performance of a wind-profiling lidar in the region of wind turbine rotor disks, J. Atmos. Ocean. Tech., 29, 347–355, doi:10.1175/JTECH-D-11-00033.1, 2012.

Antoniou, I., and Pedersen, T.F.: Nacelle Anemometry on a 1MW Wind Turbine, Risø National Laboratory, Roskilde, Denmark, 37 pp., 1997.

Antoniou, I., Pedersen, S.M., and Enevoldsen, P.B.: Wind shear and uncertainties in power curve measurement and wind resources, Wind Engineering, 33, 449–468, doi:10.1260/030952409790291208, 2009.

Archer, C. L., and Jacobson, M. Z.: Spatial and temporal distributions of U.S. winds and wind power at 80 m derived from measurements, Journal of Geophysical Research, 108, 4289, 2003.

Archer, C. L., and Jacobson, M. Z.: Supplying Baseload Power and Reducing Transmission Requirements by Interconnecting Wind Farms, Journal of Applied Meteorology and Climatology, 46, 1701-1717, 2007.

Australian Energy Market Operator, South Australian Wind Study Report 2013, iv, B-2, 2013.

AWEA, Wind energy facts at a glance, http://www.awea.org/Resources/Content.aspx?ItemNumber=5059, last accessed: 22 November 2016.

AWEA, Wind energy secures significant CO2 emission reductions for the U.S., 2014. http://www.awea.org/MediaCenter/pressrelease.aspx?ItemNumber=6320. Last access: 21 November 2016.

Baidya Roy, S., Pacala, S.W., and Walko, R.L.: Can large wind farms affect local meteorology?, Journal of Geophysical Research, 109, D19101, doi: 10.1029/2004JD004763, 2004.

Baidya Roy, S.: Simulating impacts of wind farms on local hydrometeorology, J. Wind Eng. Aerodyn., 99, 491-498, doi: 10.1016/j.jweia.2010.12.013, 2011.

Baïle, R., and Muzy, J. F.: Spatial Intermittency of Surface Layer Wind Fluctuations at Mesoscale Range. Physical Review Letters, 105, 1-4, 2010.

Baïle, R., Muzy, J. F., and Poggi, P.: Short-term forecasting of surface layer wind speed using a continuous random cascade model, Wind Energy, 14, 719-734, 2011.

Banta, R.M., Oliver, L.D., Gudiksen, P.H., and Lange, R.: Implications of small-scale flow features to modeling dispersion over complex terrain, J. Appl. Meteorol. , 35, 330–342, 1996.

Baker, R.W. and Walker, S.N.: Wake measurements behind a large horizontal axis wind turbine generator, Solar Energy, 33, 5-12, doi: 10.1016/0038-092X(84)90110-5, 1984.

Barthelmie, R.J., Frandsen, S.T., Nielsen, N.M., Pryor, S.C., Rethore, P.-E., and Jørgensen, HE.: Modelling and measurements of power losses and turbulence intensity in wind turbine wakes at Mid- delgrunden offshore wind farm, Wind Energy, 10, 217–228, 2007.

Batchelor, G. K.: The Theory of Homogenous Turbulence, Batchelor G K and Goldstein S., Cambridge University Press, Cambridge, 47-48, 1959.

Beyer, H. G., Luther, J., and Steinberger-Willms, R.: Fluctuations in the combined power output from geographically distributed grid coupled wind energy conversion systems - an analysis in the frequency domain, Wind Engineering, 14 179-192, 1990.

Beyer, H. G., Luther, J., and Steinberger-Willms, R.: Power fluctuations in spatially dispersed wind turbine systems, Solar Energy, 50, 297-305, 1993.

Bibor, E., and Masson, C.: Power Performance via Nacelle Anemometry on Complex Terrain, Wind Energy, Springer Berlin Heidelberg, 43-47, 2007.

Bingöl, F., Mann, J., and Foussekis, D.: Conically scanning LIDAR error in complex terrain, Meteorologische Zeitschrift, 18, 189–195, doi:10.1127/0941-2948/2009/0368, 2009.

Blahak, U., Goretzki, B., and Meis, J.: A Simple Parameterization of Drag Forces Induced by Large Wind Farms for Numerical Weather Prediction Models, EWEC Conference, 20-23 April 2010, Warsaw, 186-189,
http://proceedings.ewea.org/ewec2010/allfiles2/757_EWEC2010presentation.pdf, last accessed 1 December 2016.

Bonneville Power Administration: Meteorological Information from BPA Weather Sites. Can be found online at: http://transmission.bpa.gov/business/operations/wind/MetData.aspx.

Bretherton, C. S., Widmann, M., Dymnikov, V. P., Wallace, J. M., and Bladé, I.: The effective number of spatial degrees of freedom of a time-varying field, Journal of Climate, 12, 1990-2009, 1999.

Buell, C. E.: Correlation functions for wind and geopotential on isobaric surfaces, Journal of Applied Meteorology, 11, 51-59, 1972.

Calaf, M., Meneveau, C.,and Meyer, J.: Large eddy simulation study of fully developed wind-turbine array boundary layers, Physics of Fluids, 22, 015110, doi: 10.1063/1.3291077, 2010.

Carlin, J., and Haslett, J.: The Probability Distribution of Wind Power From a Dispersed Array of Wind Turbine Generators, Journal of Applied Meteorology, 21, 303-313, 1982.

Choukulkar, A., Pichugina, Y., Clack, C.T.M., Calhoun, R., Banta, R., Brewer, A. and Hardesty, M.: A new formulation for rotor equivalent wind speed for wind resource assessment and wind power forecasting, Wind Energy, 19,1439-1452, doi: 10.1002/we.1929, 2016.

Cleveland, W. S.: Robust Locally Weighted Regression and Smoothing Scatterplots, Journal of the American Statistical Association, 74, 829-836, 1979.

Clifton, A. Remote sensing of complex flows by Doppler wind lidar: issues and preliminary recommendations, NREL, Golden, Colo., 1–42, 2015.

Clifton, A., and Lundquist, J.K.: Data clustering reveals climate impacts on local phenomena, J. Appl. Meteorol. Clim., 51, 1547–1557, doi:10.1175/JAMC-D-11-0227.1, 2012.

Clifton, A., Kilcher, L., Lundquist, J. K., Fleming, P.: Using machine learning to predict wind turbine power output, Environ. Res. Lett., 8, 024009, doi:10.1088/1748-9326/8/2/024009, 2013a.

Clifton, A., Schreck, S., Scott, G., and Lundquist, J. K.,: Turbine inflow characterization at the National Wind Technology Center, J. Sol. Energ.-T. ASME, 135, 031017, doi:10.1115/1.4024068,2013b.

Cosseron, A., Gunturu, U. B., and Schlosser, C. A.: Characterization of the Wind Power Resource in Europe and its Intermittency, Energy Procedia, 40, 58-66, 2013.

Courtney, M., Wagner, R., and Lindelöw, P.: Testing and comparison of LIDARs for profile and turbulence measurements in wind energy, IOP Conference Series Earth and Environmental Science, 1, 1–14, doi:10.1088/1755-1307/1/1/012021, 2008.

Curtright, A. E., and Apt, J.: The Character of Power Output from Utility-Scale Photovoltaic Systems, Prog. Photovolt: Res. Appl., 16, 241-247, 2008.

Dahlberg, J.A., Frandsen,S., Madsen, H.A., Antoniou, I., Pedersen, T.F., Hunter, R., Klug, H., and Albers, A.: Is the nacelle mounted anemometer an acceptable option in performance testing, Proceeding of the European Wind Energy Conference, Nice, 624-637, 1999.

Davenport, A. G.: The spectrum of horizontal gustiness near the ground in high winds, Quarterly Journal of the Royal Meteorological Society, 87, 194-211, 1961.

Delle Monache, L., Eckel, F.A., Rife, D.L., Nagarajan, B., and Searight, K.: Probabilistic Weather Prediction with an Analog Ensemble, Monthly Weather Review, 141, 3498-3516, doi: 10.1175/MWR-D-12-00281.1, 2013.

Dörenkämper, M., Tambke, J., Steinfield, G., Heinemann, D., and Kühn, M.: Atmospheric impacts on power curves of multi-megawatt offshore wind turbines, Journal of Physics: Conference Series, 555, 1–11, doi: 10.1088/1742-6596/555/1/012029, 2014.

Draxl, C.: On the Predictability of Hub Height Winds, DTU Wind Energy PhD-Report, 104 pp., 2012.

Elk, M.B., Mitchell, K.E., Lin, Y., Rogers, E., Grunmann, P., Koren, V., Gayno, G., and Tarpley, J.D.: Implementation of Noah land surface model advances in the National Centers for Environmental Prediction operational mesoscale Eta model, Journal of Geophysical Research, 108, D22, doi: 10.1029/2002JD003296, 2003.

Elliott, D.L. and Barnard, J.C.: Observations of wind turbine wakes and surface roughness effects on wind flow variability, Solar Energy, 45, 265-283, doi: 10.1016/0038-092X(90)90012-2, 1990.

Elliott, D.L., and Cadogan, J.B.: Effects of wind shear and turbulence on wind turbine power curves, Proc. European Community Wind Energy Conference and Exhibition, Madrid, Spain, 1990.

Ernst, B., Wan, Y. H., and Kirby, B.: Short-Term Power Fluctuation of Wind Turbines: Analyzing Data From the German 25-MW Measurement Program from the Ancillary Services Viewpoint. National Renewable Energy Laboratory, NREL/CP-500-26722, 1-10, 1999.

Fertig, E., Apt, J., Jaramillo, P., and Katzenstein, W.: The effect of long-distance interconnection on wind power variability, Environ. Res. Lett., 7, 1-6, 2012.

Fisher, S. M., Schoof, J. T., Lant, C. L., and Therrell, M. D.: The effects of geographical distribution on the reliability of wind energy, Applied Geography, 40, 83-89, 2013.

Fitch, A.C.: Climate impacts of large-scale wind farms as parameterized in a global climate model, Journal of Climate, 28, 6160-6180, doi: 10.1175/JCLI-D-14-00245.1, 2015.

Fitch, A.C., Lundquist, J.K., and Olson, J.B.: Parameterization of Wind Farms in Climate Models, Journal of Climate, 26, 6439-6458, doi: 10.1175/JCLI-D-12-00376.1, 2013.

Fitch, A.C., Olson, J.B., Lundquist, J.K., Dudhia, J., Gupta, A.K., Michalakes, J., and Barstad, I.: Local and Mesoscale Impacts of Wind Farms as Parameterized in a Mesoscale NWP Model, Monthly Weather Review, 140, 3017-3038, doi: 10.1175/MWR-D-11-00352.1, 2012.

Fleming, P.A., Ning, A., Gebraad, P.M.O., and Dykes, K.: Wind plant system engineering through optimization of layout and yaw control, Wind Energy, 19, 329-344, doi: 10.1002/we.1836, 2016.

Frandsen, S.T., Jørgensen, H.E., Barthelmie, R., et al.: The making of a second-generation wind farm 977 efficiency model complex, Wind Energy, 12, 445–458, doi: 10.1002/we.351, 2009.

Frandsen, S., Sørensen, J.N., Mikkelsen, R., Pederesen, T.F., Antoniou, I., and Hansen, K.: The generics of wind turbine nacelle anemometry, Proceedings of European Wind Energy Conference, Marseille, France, 2009.

Gartner: Hype Cycle for emerging energy technologies, 2014, https://www.gartner.com/doc/2811929/hype-cycle-emerging-energy-technologies, last access: 22 November 2016.

GE Energy: 1.5 MW wind turbine, 2009, http://geosci.uchicago.edu/~moyer/GEOS24705/Readings/GEA14954C15-MW-Broch.pdf, last access: 21 January 2013.

Gibescu, M., Ummels, B. C., and Kling, W. L.: Statistical Wind Speed Interpolation for Simulating Aggregated Wind Energy Production under System Studies, Presented at the 9th International Conference on Probabilistic Methods Applied to Power Systems KTH, Stockholm, Sweden, 1-7, 2006.

Giebel, G.: On the benefits of distributed generation of wind energy in Europe, PhD. thesis, Carl von Ossietzky Universität Oldenburg, 1-104, 2000.

Geibel, G.: The State-Of-The-Art in Short-Term Prediction of Wind Power A Literature Review, Project ANEMOS, http://ecolo.org/documents/documents_in_english/wind-predict-ANEMOS.pdf, last accessed 30 Dec 2016, 2003.

GWEC: Global Wind Report: Annual Market Update 2015, 1-76, 2016.

Gottschall, J., and Peinke, J.: How to improve the estimation of power curves for wind turbines, Environ. Res. Lett., 3, 1–7, doi: 10.1088/1748-9326/3/1/015005, 2008.Gunst, R. F.: Estimating spatial correlations from spatial-temporal meteorological data, Journal of Climate, 8, 2454-2470, 1995.

Hasche, B.: General statistics of geographically dispersed wind power, Wind Energy, 13, 773-784, 2010.

Haslett, J., and Raftery, A. E.: Space-time modelling with long-memory dependence: assessing Ireland's wind power resource, Applied Statistics, 38, 1-50, 1989.

Helmis, C.G., Papadopoulos, K.H., Asimakopoulos, D.N., Papageorgas, P.G., and Soilemes, A.T.: An experimental study of the near-wake structure of wind turbine operating over complex terrain, Solar Energy, 54, 413-428, doi: 10.1016/0038-092X(95)00009-G, 1995.

Hill, D. C., McMillan, D., Bell, K. R. W., and Infield, D.: Application of auto-regressive models to U.K. wind speed data for power system impact studies, IEEE Transactions on Sustainable Energy, 3, 134-141, 2012.

Hinkelman, L. M.: Differences between along-wind and cross-wind solar irradiance variability on small spatial scales, Solar Energy, 88, 192-203, 2013.

Hoff, T. E., and Perez, R.: Quantifying PV power Output Variability, Solar Energy, 84, 1782-1793, 2010.

Holttinen, H.: Hourly wind power variation in the Nordic countries, Wind Energy, 8, 173-195, 2005.

Huang, J., Lu, X., and McElroy, M. B.: Meteorologically defined limits to reduction in the variability of outputs from a coupled wind farm system in the Central U.S., Renewable Energy, 62, 331-340, 2014.

Hunter, R., Pedersen, T.F., Dunbabin, P., Antoniou, I., Frandsen, S., Klug, H., Albers, A., and Lee, W.K.: European wind turbine testing procedure developments: Task 1: measurement method to verify wind turbine performance characteristics, Risø National Laboratory, Roskilde, Denmark,1–120, 2001.

Iacono, M.J., Delamere, J.S., Mlawer, E.J., Shephard, M.W., Clough, S.A., and Collins, W.D.: Radiative forcing by long-lived greenhouse gases: Calculations with the AER radiative transfer models, Journal of Geophysical Research, 113, D13103, doi: 10.1029/2008JD009944, 2008.

IEA: Technology roadmap: Wind Energy 2013 edition, 2013, https://www.iea.org/publications/freepublications/publication/Wind_2013_Roadmap.pdf, last accessed: 22 November 2016.

IEC 61400-12-1 Ed 2.0: Wind turbines – Part 12-1: power performance measurements of electricity producing wind turbines, IEC, Geneva, Switzerland, 2015.

IEC 61400-12-2 Ed. 1.0: Wind turbines – Part 12-2: power performance of electricity producing wind turbines based on nacelle anemometry, IEC, Geneva, Switzerland, 2013.

International Energy Agency: IEA Statistics with data up to July 2016: Monthly Electricity Statistics,15 October 2016, http://www.iea.org/media/statistics/surveys/electricity/mes.pdf, last accessed: 3 Nov 2016.

IPCC: Climate Change 2014 Mitigation of climate change: working group III contribution to the fifth assessment report of the intergovernmental panel on climate change, pp. 1335, 2014, https://www.ipcc.ch/pdf/assessment-report/ar5/wg3/ipcc_wg3_ar5_full.pdf, last accessed 21 November 2016.

Jiménez, P.A., Navarro, J., Palomares, A.M., and Dudhia, J.: Mesoscale modeling of offshore wind turbine wakes at the wind farm resolving scale: a composite-cased analysis with the Weather Research and Forecasting model over Horns Rev, Wind Energy, 18, 559-566, doi: 10.1002/we.1708, 2015.

Julian, P. R., and Thiebaux, H. J.: On some properties of correlation functions used in optimum interpolation schemes, Monthly Weather Review, 103, 605-616, 1975.

Justus, C. G., and Mikhail, A. S.: Energy statistics for large wind turbine arrays, Georgia Institute of Technology, 1978.

Kahn, E.: The Reliability of Distributed Wind Generators, Electric Power Systems Research, 2, 1-14, 1979.

Kain, J.S.: The Kain-Fritsch Convective Parameterization: An Update, Journal of Applied Meteorology, 43, 170-181, doi: 10.1175/1520-0450(2004)043<0170:TKCPAU>2.0.CO;2 , 2004.

Kaiser, K., Hohlen, H., and Langreder, W.: Turbulence correction for power curves, Wind Energy Proc. European Wind Energy Conference and Exhibition, Madrid, 159–162, 2003.

Katzenstein, W., Fertig, E., and Apt, J.: The variability of interconnected wind plants, Energy Policy, 38, 4400-4410, 2010.

Keck, R.E.: A numerical investigation of nacelle anemometry for a HAWT using actuator disc and line models in CFX, Renewable Energy, 48, 72-84, doi: 10.1016/j.renene.2012.04.004, 2012.

Keith, D.W., DeCarolis, J.F., Denkenberger, D.C., Lenschow, D.H., Malyshev, S.L., Pacala, S., and Rasch, P.J.: The influence of large-scale wind power on global climate, PNAS, 101, 16115-16120, doi: 10.1073/pnas.0406930101, 2004.

Kelley, N.D.: Turbulence-turbine interaction: the basis for the development of the TurbSim Stochastic Simulator, NREL, Golden, Colo., 2011. http://www.nrel.gov/docs/fy12osti/52353.pdf, last access: 8 May 2016.

Kelley, N. D., Jonkman, B. J., and Scott, G.N.: The Great Plains Turbulence Environment: Its Origins, Impact and Simulation, Presented at the AWEA 2006 WindPower Conference, NREL, Golden, Colo., 2006. http://www.nrel.gov/docs/fy07osti/40176.pdf, last access, 27 November 2016.

Kempton, W., Pimenta, F. M., Veron, D. E., and Colle, B. A.: Electric power from offshore wind via synoptic-scale interconnection, Proceedings of the National Academy of Sciences of the United States of America, 107, 7240-7245, 2010.

Kirby, B.: Frequency Regulation Basics and Trends, Oak Ridge National Laboratory, TM-2004/291, 2005.

Kiss, P., and Jánosi, I. M.: Limitations of wind power availability over Europe: a conceptual study, Nonlinear Processes in Geophysics, 15, 803-813, 2008.

Landberg, L.: Availability and variability of the European wind resource, International Journal of Solar Energy, 18, 313-320, 1997.

Landberg, L.: Short-term prediction of the power production from wind farms, Journal of Wind Engineering, 80, 207-220, 1999.

Lave, M., and Kleissl, J.: Cloud speed impact on solar variability scaling – Application to the wavelet variability model, Solar Energy, 91, 11-21, 2013.

Lazard: Lazard's levelized cost of energy analysis–version 9.0, November 2015, https://www.lazard.com/media/2390/lazards-levelized-cost-of-energy-analysis-90.pdf, last accessed: 22 November 2016.

Link, H.F., and Santos, R: International Energy Agency Wind Turbine Round-Robin Test Task: Final Report, NREL, Golden, CO, 31 pp, 2004, last access: 24 May 2016, http://www.nrel.gov/docs/fy04osti/36238.pdf.

Louie, H.: Correlation and statistical characteristics of aggregate wind power in large transcontinental systems, Wind Energy, 17, 793-810, 2014.

Lu, H., Porté-Agel, F.: Large-eddy simulation of a very large wind farm in a stable atmospheric boundary layer, Physics of Fluids, 23, 065101, doi: 10.1063/1.3589857, 2011.

Lundquist, J.K., Churchfield, M.J., Lee, S., and Clifton, A.: Quantifying error of lidar and sodar Doppler beam swinging measurements of wind turbine wakes using computational fluid dynamics, Atmospheric Measurement Techniques, 8, 907–920, doi: 10.5194/amt-8-907-2015, 2015.

Lundquist, J. K., Purkayastha, A., St. Martin, C., and Newsom, R.: Estimating the Wind Resource in Uttarakhand: Comparison of Dynamic Downscaling with Doppler Lidar Wind Measurements, NREL Technical Report NREL/TP-5000-61103, 1-38, http://www.nrel.gov/docs/fy14osti/61103.pdf, 2013.

Magnusson, M. and Smedman, A.S.: Influence of atmospheric stability on wind turbine wakes. Wind Eng., 18, 139–151, 1994.

Marcos, J., Marroyo, L., Lorenzo, E., Alvira, D., and Izco, E.: From irradiance to output power fluctuations: the pv plant as a low pass filter, Prog. Photovolt: Res. Appl., 19, 505-510, 2011.

Marcos, J., Marroyo, L., Lorenzo, E., García, M.: Smoothing of PV power fluctuations by geographical Dispersion, Progress in Photovoltaics: Research and Applications, 20, 226-237, 2012.

Marquis, M., Wilczak, J., Ahlstrom, M., Sharp, J., Stern, A., Smith, J.C., and Calvert, S.: Forecasting the wind to reach significant penetration levels of wind energy, Bulletin of the American Meteorological Society, September 2011, 1159-1171, doi: 10.1175/2011BAMS3033.1, 2011.

Matheron, G.: Principles of Geostatistics, Economic Geology, 58, 1246-1266, 1963.

McNerney, G., and Richardson, R.: The Statistical Smoothing of Power Delivered to Utilities by Multiple Wind Turbines, IEEE Transactions on Energy Conversion, 7, 644-647, 1992.

Mendoza, I., Hur, J., Thao, S., Curtis, A.: Power performance test report for the U.S. Department of Energy 1.5-megawatt wind turbine, NREL, Golden, Colo., 1–55, 2015, last access: 8 May 2016, http://www.nrel.gov/docs/fy15osti/63684.pdf.

Milligan, M., and Factor, T.: Optimizing the Geographic Distribution of Wind Plants in Iowa for Maximum Economic Benefit and Reliability, Wind Engineering, 24, 271-290, 2000.

Mills, A. D., and Wiser, R. H.: Implications of Geographic Diversity for Short-Term Variability and Predictability of Solar Power, 2011 IEEE Power and Energy Society General Meeting, 2011.

Mirocha, J.D., Kosović, B., Aitken, M.L., and Lundquist, J.K.: Implementation of a generalized actuator disk wind turbine model into the weather research and forecasting model for large-eddy

simulation applications, Journal of Renewable and Sustainable Energy, 6, 013104, doi: 10.1063/1.4861061, 2014.

Molly, J. P.: Balancing power supply from wind energy converting systems, Wind Engineering, 1, 57-66, 1977.

Motta, M., Barthelmie, R.J., and Vølund, P.: The influence of non-logarithmic wind speed profiles on potential power output at Danish offshore sites, Wind Energy, 8, 219–236, 2005.

Muñoz-Esparza, D., Cañadillas, B., Neumann, T., and vanBeech, J.: Turbulent fluxes, stability and shear in the offshore environment: mesoscale modelling and field observations at FINO1, Journal of Renewable and Sustainable Energy, 4, 1–16, doi: 10.1063/1.4769201, 2012.

Nakanishi, M., and Niino, H.: An Improved Mellor-Yamada Level-3 Model: Its Numerical Stability and Application to a Regional Prediction of Advection Fog, Boundary-Layer Meteorology, 119, 397-407, doi: 10.1007/s10546-005-9030-8, 2006.

Nanahara, T., Asari, M., Sato, T., Yamaguchi, K., Shibata, M., and Maejima, T.: Smoothing Effects of Distributed Wind Turbines, Part 1, Coherence and Smoothing Effects at a Wind Farm, Wind Energy, 761-74, 2004.

National Hydropower Association: FAQ, http://www.hydro.org/policy/faq/, last accessed: 27 November 2016.

NWTC 135-m Tower Data: https://nwtc.nrel.gov/MetData, last accessed: 18 May 2016.

Palutikof, J. P., Cook, H. F., and Davies, T. D.: Effects of geographical dispersion on wind turbine performance in England: A simulation, Atmospheric Environment, 24A, 213-227, 1990.

Poulos, G.S., Bossert, J.E., Pielke, R.A., and McKee, T.B.: The interaction of katabatic flow and mountain waves I: observations and idealized simulations, J. Atmos. Sci., 57, 1919–1936, 2000.

Poulos, G.S., Bossert, J.E., Pielke, R.A., and McKee, T.B.: The interaction of katabatic flow and mountain waves II: case study analysis and conceptual model, J. Atmos. Sci., 64, 1857–1879, 2007.

Rai, R.J., Berg, L.K., Kosovic, B., Mirocha, J.D., Pekour, M.S., and Shaw, W.J.: Comparison of Measured and Numerically Simulated Turbulence Statistics in a Convective Boundary Layer Over Complex Terrain, Boundary-Layer Meteorol, 163, 69-89, 2017.

Rajewski, D.A., Takle, E.S., Lundquist, J.K., Oncley, S., Prueger, J.H., Horst, T.W., Rhodes, M.E., Pfeiffer, R., Hatfield, J.L., Spoth, K.K., and Doorenbos, R.K.: Crop Wind Energy Experiment (CWES) Observations of Surface-Layer, Boundary Layer, and Mesoscale Interactions with a Wind Farm, Bulletin of the American Meteorological Society, May 2013, 655-672, doi: 10.1175/BAMS-D-11-00240.1, 2013.

Ramanathan, Y., Kulkarni, P. and Sikka, D. R.: On a study of winter season wind structure at 500 mb in the Indian region for use in objective analysis of the wind field, Journal of Applied Meteorology, 12, 977-983, 1973.

Rareshide, E., Tindal, A., Johnson, C., Graves, A.M., Simpson, E., Bleeg, J., Harris, T., and Schoborg, D.: Effects of complex wind regimes on turbine performance, AWEA Windpower 2009 meeting, Chicago, Ill., 2009.

Rhodes, M.E., and Lundquist, J.K.: The effect of wind-turbine wakes on summertime US Midwest atmospheric wind profiles as observed with ground-based Doppler LIDAR, Boundary-Layer Meteorol. 149, 85–103, doi:10.1007/s10546-013-9834-x, 2013.

Rinker, J.M., Gavin, H.P., Clifton, A., Veers, P.S., and Kilcher, L.F.: Temporal coherence: a model for non-stationarity in natural and simulated wind records, Boundary-Layer Meteorol., 159, 373–389, doi: 10.1007/s10546-015-0121-x, 2016.

Robeson, S. M., and Shein, K. A.: Spatial coherence and decay of wind speed and power in the North-Central United States, Physical Geography, 18, 479-495, 1997.

Šaltytė Benth, J., and Šaltytė, L.: Spatial-temporal model for wind speed in Lithuania, Journal of Applied Statistics, 38, 1151-1168, 2011.

Sanderse, B., van der Pijl, S.P., and Koren, B.: Review of computational fluid dynamics for wind turbine wake aerodynamics, Wind Energy, 14, 799-819, doi: 10.1002/we.458, 2011.

Şen, Z.: Cumulative Semivariogram Models of Regionalized Variables, Mathematical Geology, 21, 891-903, 1989.

Şen, Z., and Şahin, A. D.: Regional assessment of wind power in western Turkey by the cumulative semivariogram method, Renewable Energy, 12, 169-177, 1997.

Simonsen, T. K., and Stevens, B. G.: Regional wind energy analysis for the central United States. Presented at Global Wind Power, 1-15, 2004.

Sinden, G.: Characteristics of the UK wind resource: Long-term patterns and relationship to electricity Demand, Energy Policy, 25, 112-127, 2007.

Smaïli, A., and Masson, C.: On the rotor effects upon nacelle anemometry for wind turbines, Wind Energy, 28, 695-714, doi: 10.1260/0309524043729958, 2004.

Smith, B., Link, H., Randall, G., and McCoy, T.: Applicability of Nacelle Anemometer Measurements for Use in Turbine Power Performance Tests, AWEA Windpower, Portland, OR, 2002.

Sørensen, P., Cutululis, N. A., Vigueras-Rodríguez, A., Madsen, H., Pinson, P., Jensen, L. E., Hjerrild, J., and Donovan, M.: Modelling of power fluctuations from large offshore wind farms, Wind Energy, 11, 29-43, 2008.

St. George, S. and Wolfe, S. Z.: El Nino stills winter winds across the southern Canadian Prairies, Geophysical Research Letters, 36, 1-5, 2009.

St. Martin, C. M., Lundquist, J. K., Clifton, A., Poulos, G. S., and Schreck, S. J.: Wind turbine power production and annual energy production depend on atmospheric stability and turbulence, Wind Energ. Sci., 1, 221-236, doi:10.5194/wes-1-221-2016, 2016.

Stull, R.B.: An Introduction to Boundary Layer Meteorology, Kluwer Academic Publishers, Netherlands, 1988.

Sumner, J., and Masson, C.: Influence of atmospheric stability on wind turbine power performance curves, J. Sol. Energ.-T ASME, 128, 531–538, doi:10.1115/1.2347714, 2006.

Tarroja, B., Mueller, F., Eichman, J. D., Brouwer, J., and Samuelsen, S.: Spatial and temporal analysis of electric wind generation intermittency and dynamics, Renewable Energy, 36, 3424-3432, 2011.

Thomas, P. H.: Electric Power From the Wind, Federal Power Commission, 1-74, 1945.

Thompson, G., and Eidhammer, T.: A Study of Aerosol Impacts on Clouds and Precipitation Development in a Large Winter Cyclone, Journal of the Atmospheric Sciences, 71, 3636-3658, doi: 10.1175/JAS-D-13-0305.1, 2014.

United Nations: Paris Agreement, 1-17, 2015.

U.S. Energy Information Administration: Annual Energy Outlook 2016 Early Release: Annotated Summary of Two Cases, http://www.eia.gov/forecasts/aeo/er/pdf/0383er(2016).pdf, last accessed: 3 Nov 2016.

U.S. Energy Information Administration: Frequently asked questions: How much electricity does an American home use?, 2016, https://www.eia.gov/tools/faqs/faq.cfm?id=97&t=3, las accessed: 22 November 2016.

U.S. Energy Information Administration: Today in Energy, Total U.S. energy production increases for sixth consecutive year, https://www.eia.gov/todayinenergy/detail.php?id=25852, last accessed: 3 Nov 2016.

U.S. Energy Information Administration: U.S. Crude oil and natural gas proved reserves 2014, 2015, http://www.eia.gov/naturalgas/crudeoilreserves/pdf/usreserves.pdf, last accessed: 21 November 2016.

U.S. Energy Information Administration: Wind generation share exceeded 10% in 11 states in 2015, https://www.eia.gov/todayinenergy/detail.php?id=28512, last accessed: 22 November 2016.

U.S. Geological Society Energy Resources Program, https://eerscmap.usgs.gov/windfarm/, last accessed 30 Dec 2016.

U.S. Nuclear Regulatory Commission: Location of Projected New Nuclear Power Reactors, 2016, http://www.nrc.gov/reactors/new-reactors/col/new-reactor-map.html, last accessed 27 November 2016.

van den Berg, G.P.: Wind turbine power and sound in relation to atmospheric stability, Wind Energy, 11, 151–169, 2008.

Vanderwende, B.J., Kosović, B., Lundquist, J.K., and Mirocha, J.D.: Simulating effects of a wind-turbine array using LES and RANS, J. Adv. Model. Earth Syst., 8, 1376-1390, doi: 10.1002/2016MS000652, 2016.

Vanderwende, B., and Lundquist, J.K.: The modification of wind turbine performance by statistically distinct atmospheric regimes, Environ. Res. Lett., 7, 1–7, doi:10.1088/1748-9326/7/3/034035, 2012.

von Kármán, T.: Progress in the Statistical Theory of Turbulence, Proceedings of the National Academy of Sciences, 34, 530-539, 1948.

von Meier, M.: Electric Power Systems: A Conceptual Introduction (Hoboken: Wiley), 2006.

Wagenaar, J.W., and Eecen, P.J.: Dependence of power performance on atmospheric conditions and possible corrections, European Wind Energy Association (EWEA) 2011 conference, Brussels, Belgium, 2011. http://www.ecn.nl/docs/library/report/2011/m11033.pdf, last access: 9 May 2016.

Wagner, R., Antoniou, I., Pedersen, S., Courtney, M., and Jorgensen, H.: The influence of the wind speed profile on wind turbine performance measurements, Wind Energy, 12, 348–362, doi:10.1002/we.297, 2009.

Wan, H., Wang, X. L., and Swail, V. R.: Homogenization and Trend Analysis of Canadian Near-Surface Wind Speeds, Journal of Climate, 23, 1209-1225, 2010.

Whale, J., Andersen, C.G., Bareiss, R., and Wagner, S.: An experimental and numerical study of the vortex structure in the wake of a wind turbine, J. Wind Eng. Ind. Aerodyn., 84, 1-21, doi: 10.1016/S0167-6105(98)00201-3, 2000.

Wharton, S., and Lundquist, J.K.: Atmospheric stability affects wind turbine power collection, Environ. Res. Lett., 7, 1–9, doi:10.1088/1748-9326/7/1/014005, 2012a.

Wharton, S. and Lundquist, J.K.: Assessing atmospheric stability and its impacts on rotor-disk wind characteristics at an onshore wind farm, Wind Energy, 15, 525–546, doi:10.1002/we.483, 2012b.

Wiemken, E., Beyer, H. G., Heydenreich, W., and Kiefer, K.: Power characteristics of PV ensembles: experiences from the combined power production of 100 grid connected PV systems distributed over the area of Germany, Solar Energy, 70, 513-518, 2001.

Wilczak, J., Finley, C., Freedman, J., Cline, J., et al.: The wind forecast improvement project (WFIP) A public-private partnership addressing wind energy forecast needs, Bulletin of the American Meteorological Society, October 2015, 1699-1718, doi: 10.1175/BAMS-D-14-00107.1, 2015.

Wu, Y-T. and Porté-Agel, F.: Simulation of Turbulent Flow Inside and Above Wind Farms: Model Validation and Layout Effects, Boundary-Layer Meteorol, 146, 181-205, doi: 10.1007/s10546-012-9757-y, 2013.

Zahle, F., and Sørensen, N.N.: Characterization of the unsteady flow in the nacelle region of a modern wind turbine, Wind Energy, 13, 271-283, doi: 10.1002/we.418, 2011.

Zhou, L., Tian, Y., Baidya Roy, S., Thorncroft, C., Bosart, L.F., and Hu, Y.: Impacts of wind farms on land surface temperature, Nature Climate Change, 2, 539-543, doi: 10.1038/NCLIMATE1505, 2012.

APPENDIX A

Supplementary Data for:

St. Martin, C. M., Lundquist, J. K., and Handschy, M. A.: Variability of interconnected wind plants: correlation length and its dependence on variability time scale. *Environ. Res. Lett.*, 10, 044004, doi:10.1088/1748-9326/10/4/044004, 2015.

S1 Additional information about datasets used

Maps illustrating station and wind farm locations are shown in Figure S 1 for Australia (AUS), Canada (CAN) and Bonneville Power Authority (BPA). Names and locations of the Australian wind farms and BPA stations we use in this analysis are in Table S 1 and Table S 2, respectively. Data availability for AUS is greater than 98% for 25 of the 29 wind farms, for CAN is greater than 95% for 91 of the 117 sites, and for BPA is greater than 98% for 13 of the 14 sites used. A subset of 39 Canadian stations with 0.1% or less missing data is used for some of the analysis here: separation distances from these stations vary from a minimum of 64 km to a maximum of 5203 km.

S2 Diurnal and seasonal cycles in data

Figure S 2 shows the periodogram and correlogram for the wind speed time-series data from a typical CAN station. For frequencies higher than about once per 90 days, the power spectrum of the raw data (gray) resembles a von Kármán (von Kármán, 1948) or Kaimal (Kaimal et al., 1972) spectrum, but with prominent peaks corresponding to a diurnal cycle and its harmonics. The autocorrelation calculated from the raw data similarly has maxima at multiples of 24-hour lag. At the lowest frequencies, the power spectral density increases with decreasing frequency; the autocorrelation function correspondingly does not approach zero for lags well in excess of several days. Inter-station correlation versus separation distance calculated from these

raw data show a "ripple" and a non-zero floor (Figure S 3a): the correlation reaches a minimum near 1500 km, then increases again to 2800 km, then decreases again, but not to zero. Removing the diurnal cycle and low-frequency variation from the time-series data according to the procedure described below removes the ripple in the correlation vs. distance behavior and results in the correlation falling to zero at large distances (Figure S 3b).

S2.1 Filtering

In light of the above, we suppose the wind speed (or generation) time-series $v_i(t)$ at the i^{th} station can be represented by a stochastic process $v_i^S(t)$ with additive, seasonally-varying diurnal cycle $S_i(t)$: $v_i(t) = v_i^S(t) + S_i(t)$. Following a method similar to that of Baïle et al. (2011), we make a local estimate of the diurnal cycle in order to accommodate its seasonally-varying nature. For each day of each station's time-series record we utilize a data segment comprising that day and the 45 days on either side. We represent the diurnal cycle by the first four components of a Fourier series, determining the coefficients in equation (S 1) by least-squares fitting to the data segment, apodized by a Welch (Welch, 1967) window with weights sets to zero at the locations of any missing data.

$$S(t_i) = a_0 + \sum_{k=1}^{4} \left[a_k \sin\left(\frac{2k\pi t_i}{24}\right) + b_k \cos\left(\frac{2k\pi t_i}{24}\right) \right] \quad \text{(S1)}$$

After fitting separately for each day of the record (save the first and last 45 days which we discard), we subtract the appropriate cycle from the 24 hourly values of each days' wind speed or power generation values. While not part of the diurnal cycle, we also subtract the seasonally-varying "bias" term a_0, thereby also removing all trends slower than seasonal.

To elaborate the dependence of spatial correlation scale on temporal fluctuation frequency, we calculate the correlation coefficient between time-series data for the various

stations or wind farms after the time-series data have been temporally high-pass filtered with various filter cut-offs. Accordingly, the CAN (AUS, BPA) data are smoothed (low-pass filtered) using a moving boxcar window with 17 (22) different averaging window widths ranging from three hours (15 minutes) to 2049 hours (1707 hours). Subtracting the smoothed series from the original yields a high-pass filtered series. Without further high-pass filtering, the pre-processed data already had seasonal trends lower than τ = 2160 h removed as described above; we utilize these data as well. An application of this approach to a 30-day time-series from one CAN station appears in Figure S 4. This de-trending of the time-series is applied to focus on the dependence of correlation length on timescale.

S3 Correlation vs distance

For each averaging window width (or equivalently, each high-pass filter cut-off), we calculate the (Pearson) correlation coefficient ρ_{ij} for the de-trended and high-pass-filtered wind speed time-series for each pair of stations i and j. We ignore any time steps with missing values and create scatterplots of correlation $\rho(r_{ij})$ vs. station separation r_{ij}.

S3.1.1 AUS correlations

Correlations in normalized, de-trended power generation between Australian wind farms drop with farm separation distance as shown in Figure S 5, dropping faster at smaller high-pass filter window widths. At larger window widths, there is larger scatter in the correlations and more prominent anti-correlations at the larger farm separation distances.

S3.1.2 BPA correlations

Wind speed correlations between the 91 station pairs in BPA also decrease with increasing distance as shown in Figure S 6. The smaller geographic extent of the BPA regions

makes it difficult to compare the BPA to CAN spatial correlation analysis results. The largest station separation distance in BPA is about 350 km compared to 5300 km in CAN, but BPA offers finer time resolution (5-min vs hourly).

S3.2 Investigating large scatter in CAN correlations

Large scatter in correlations at shorter station separation distances can be seen in Figure 1 and Figure S7. To further investigate the observed correlations that drop below zero in CAN as well as the large scatter in correlations at smaller station separation distances, we compare correlations for separate regions (east and west regions as well as north and south regions) as well as by azimuthal bearing.

S3.2.1 Azimuthal bearing

To investigate the hypothesis that the longitudinal vs. transverse bearing of a station-pair relative to the direction of prevailing winds could affect the correlation length scale, we plot correlation vs distance with points colored according to a scale given:

$$\sigma = \sin(2\vartheta + \delta) \tag{S2}$$

where ϑ is the bearing from North of the station separation. We compare plots with different δ's, finding the δ value that accounted for the most scatter (δ = 110°).

S3.2.2 Impact of climate oscillations

Most of the analysis uses all available data from 1962–2006. To test the hypothesis that climate oscillations, such as the El Niño Southern Oscillation (ENSO), affect the correlations, we isolate periods of strong ENSO using the Multivariate ENSO Index (MEI). The MEI is based on observed values of sea level pressure, zonal and meridional components of the wind, sea surface

temperature, surface air temperature, and total cloudiness and the seasonal variations in these observed values (Wolter and Timlin, 1993). Strong ENSO events are determined by ranking bimonthly normalized MEI values (Wolter and Timlin, 2011). Lengths of ENSO events are determined by the number of consecutive bimonthly normalized MEI values that are positive (El Niño) or negative (La Niña). We isolate the 19-month El Niño event from April 1982 through October 1983, and the 19-month La Niña event from May 1988 through October 1989. As the plot in Figure 4(d) shows, the ENSO was found to have little to no effect on the correlations. We also isolated the 13-month El Niño event from April 1965 through April 1966 and the 13-month La Niña event from February 1964 through February 1965, the 13-month El Niño event from April 1972 through April 1973 and the 13-month La Niña event from September 1970 through September 1971, as well as the combination of these periods, and still did not find any significant difference in correlations between strong positive and strong negative ENSO periods. Calculated differences in the 1965-1966 El Niño and 1964-1965 La Niña correlations shown in Figure S7 show a mean of -0.0011 and a standard deviation of 0.044.

Supplementary Data References

Baïle, R., Muzy, J. F., and Poggi, P.: Short-term forecasting of surface layer wind speed using a continuous random cascade model, Wind Energy, 14, 719-734, 2011.

Kaimal, J. C., Wyngaard, J. C., Izumi, Y., and Coté, O. R.: Spectral characteristics of surface-layer turbulence, Quart. J. R. Met. Soc., 98, 563-589, 1972.

Press, W. H., Teukolsky, S. A., Vetterling, W. T., and Flannery, B. P.: Numerical Recipies: The Art of Scientific Computing, Cambridge University Press 3 ed., 660-662, 2007.

von Kármán, T.: Progress in the Statistical Theory of Turbulence, Proceedings of the National Academy of Sciences, 34, 530-539, 1948.

Welch, P. D.: The Use of Fast Fourier Transform for the Estimation of Power Spectra: A Method Based on Time Averaging Over Short, Modified Periodograms, IEEE Trans. Audio Electroacoustics, 15, 70-73, 1967.

Wolter, K., and Timlin, M. S.: Monitoring ENSO in COADS with a Seasonally Adjusted Principal Component Index, Proceedings of the 17th Climate Diagnostics Workshop, Norman, OK, NOAA/MNC/CAC, NSSL, Oklahoma Clim. Survey, CIMMS and the School of Meteor., Univ. of Oklahoma, 52-57, 1993.

Wolter, K., and Timlin, M. S.: El Niño/Southern Oscillation behavior since 1871 as diagnosed in an extended multivariate ENSO index (MEI.ext), International Journal of Climatology, 31, 1074-1087, 2011.

Supplementary Data Tables

Table S1: List of the Australian wind farms used in this work.

Farm Name	Farm ID	Latitude	Longitude
Capital Wind Farm	CAPTL_WF	-35.164313	149.518197
Cullerin Range Wind Farm	CULLRGWF	-34.805595	149.399996
Gullen Range Wind Farm	GULLRWF1	-34.614692	149.460105
Gunning Wind Farm	GUNNING1	-34.693318	149.378398
Woodlawn Wind Farm	WOODLWN1	-35.07191	149.566194
The Bluff Wind Farm	BLUFF1	-33.379859	138.800762
Cathedral Rocks Wind Farm	CATHROCK	-34.848752	135.579549
Clements Gap Wind Farm	CLEMGPWF	-33.491782	138.115395
Hallett 1 Wind Farm	HALLWF1	-33.308711	138.728828
Hallett 2 Wind Farm	HALLWF2	-33.563158	138.863633
Lake Bonney Wind Farm	LKBONNY2&3	-37.758933	140.40062
Mt Millar Wind Farm	MTMILLAR	-33.700692	136.740144
North Brown Hill Wind Farm	NBHWF1	-33.238884	138.721145
Snowtown Wind Farm Stage 2 North	SNOWNTH1	-33.760186	138.140621
Snowtown South Wind Farm	SNOWSTH1	-33.856538	138.119708
Snowtown Wind Farm Units 1 and 47	SNOWSTWN1	-33.684932	138.177357
Starfish Hill Wind Farm	STARHLWF	-35.568967	138.142933
Waterloo Wind Farm	WATERLWF	-34.003079	138.914961
Wattle Point Wind Farm	WPWF	-35.123503	137.712455
Musselroe Wind Farm	MUSSELR1	-40.78006	148.002821
Woolnorth Studland Bay / Bluff Point Wind Farm	WOOLNTH1	-40.680464	144.699311
Challicum Hills Wind Farm	CHALLHWF	-37.389725	143.107857
Macarthur Wind Farm	MACARTH1	-38.040812	142.02954
Mt Mercer Wind Farm	MERCER01	-37.824887	143.874131
Mortons Lane Wind Farm	MLWF1	-37.837554	142.466641
Oaklands Hill Wind Farm	OAKLAND1	-37.681232	142.5530087
Portland Wind Farm	PORTWF	-38.349937	141.589335
Waubra Wind Farm	WAUBRAWF	-37.362083	143.601391
Yambuk Wind Farm	YAMBUKWF	-38.31476	142.024078

Table S2: List of the BPA stations used in this work.

BPA station	Latitude	Longitude	Height AGL (m)
Augspurger	45.736263	-121.680858	21.336
BiddleButte	45.580749	-122.207451	22.5552
ForestGrove	45.524249	-123.088548	9.144
HoodRiver	45.688002	-121.52391	9.144
HorseHeaven	45.933771	-119.634224	21.336
MarysPeak	44.504299	-123.552464	6.096
Megler	46.266005	-123.877276	53.34
MtHebo	45.213434	-123.755384	15.24
NaselleRidge	46.421801	-123.796896	30.48
Roosevelt	45.764636	-120.240082	21.336
Shanoko	45.02515	-120.835323	9.144
Sunnyside	46.485693	-119.992561	9.144
Tillamook	45.457724	-123.828638	9.144
Troutdale	45.558324	-122.401734	30.48

Supplementary Data Figures

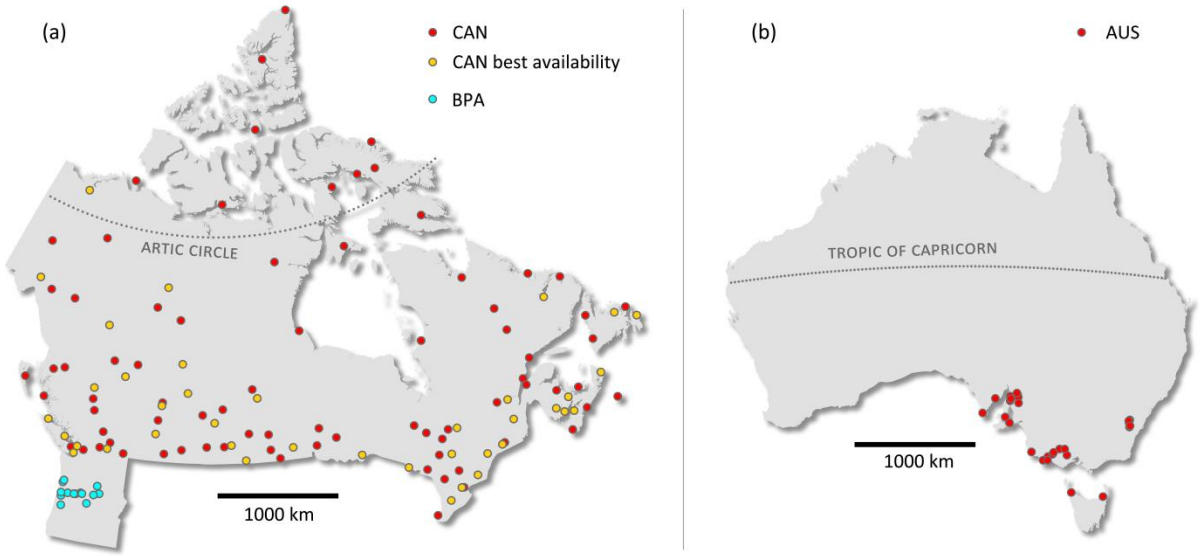

Figure S1: (a) CAN (red and yellow dots) and BPA (aqua) station locations. Yellow dots indicate the CAN stations with at least 99.9% data availability; (b) Australian wind farm locations (red dots).

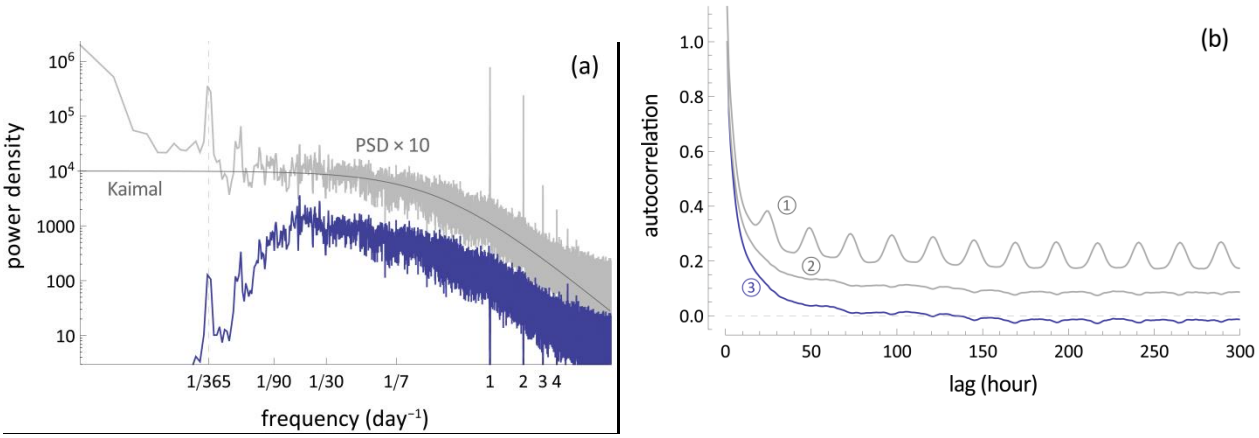

Figure S2: (a) Periodograms for a Canadian station calculated using the Welch method (Press et al. 2007) (471,168 hourly wind-speed data samples with 371 missing points replaced by overall mean, partitioned into seven Hamming-windowed 50% overlapping segments of length 117,792). Gray: raw data; blue; after 90-day high-pass filter and diurnal cycle removal. Kaimal PSD=10000[1+(2.8 d)f]$^{-1}$; (b) correlograms: (1) raw data displaced up by 0.13, (2) data with diurnal cycle removed (not displaced), (3) data with both diurnal cycle and seasonally-varying bias removed.

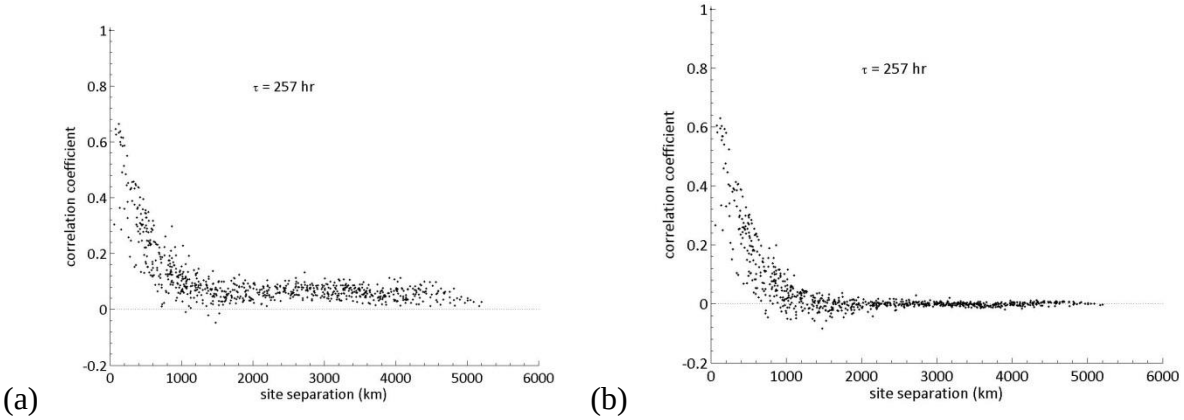

Figure S3: Correlations vs distance with data from 39 Canadian stations with little missing data: (a) high-pass filtered (τ = 257 h), but without removal of diurnal and bias; (b) both high-pass filtering (τ = 257 h), and diurnal cycle and seasonal bias removal.

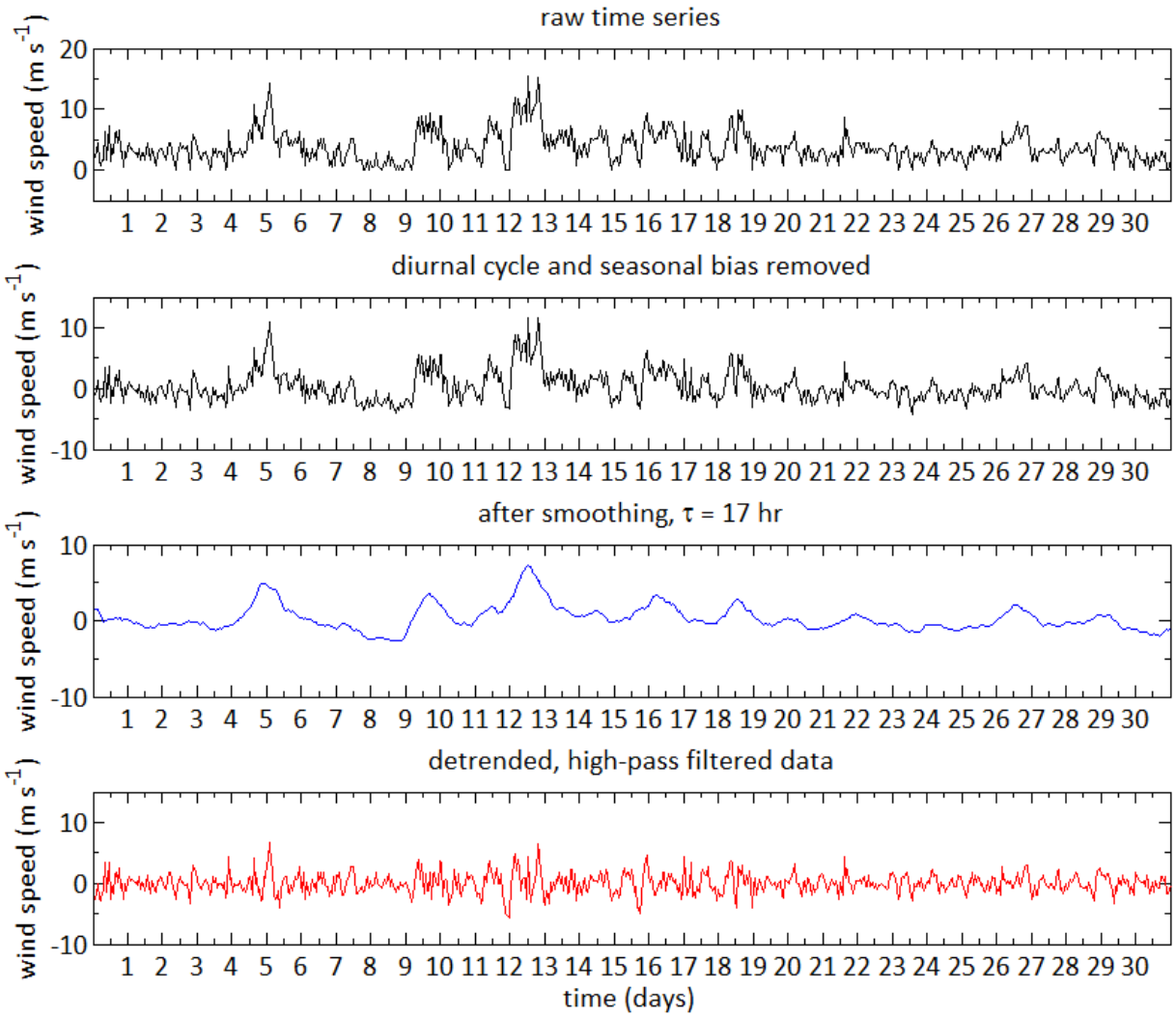

Figure S4: Wind speed time-series from one Canadian site for 4/15–5/20/1962. Top: raw time series. Top middle: with bias and Fourier terms removed. Bottom middle: after averaging with a 17-hour moving window. Bottom: after subtracting the 17-hr window smoothed values from the original data.

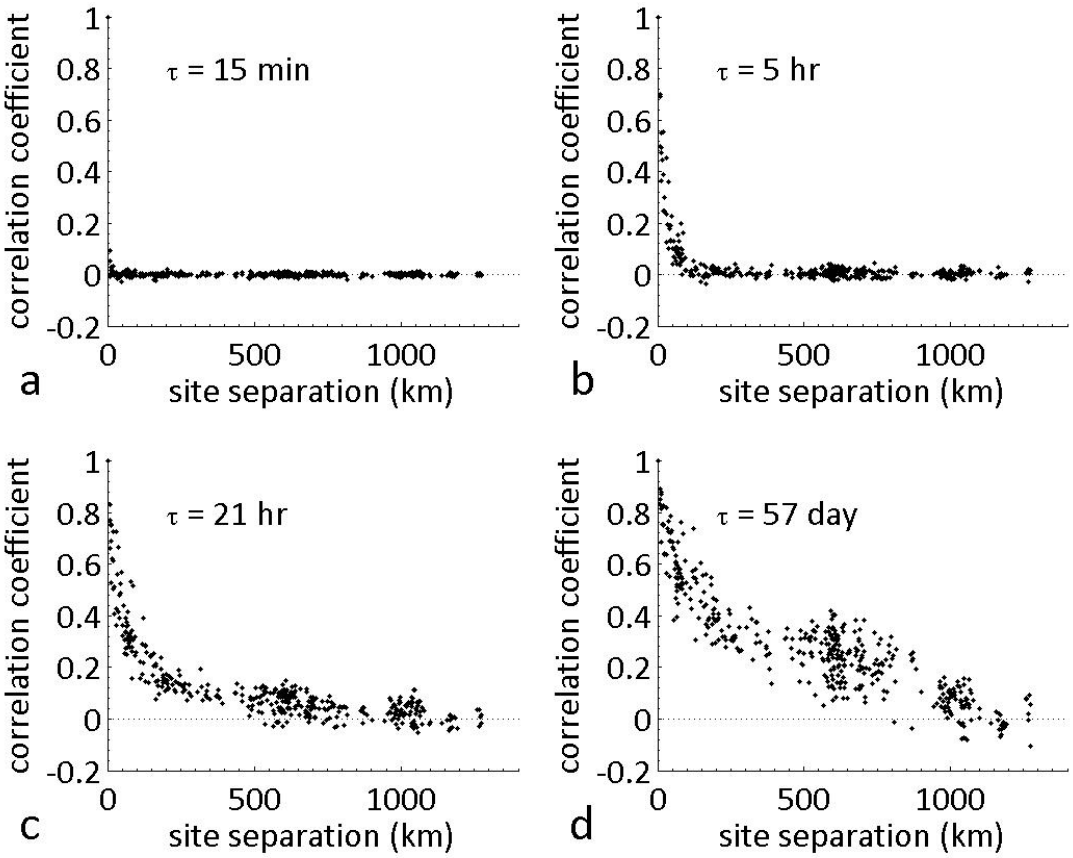

Figure S5: Correlation vs site separation for 29 Australian farms. Five-minute net generation data from 2013 through 2014: (a) high-pass window width τ = 15 minutes; (b) τ = 5 hours; (c) τ = 21 hours; (d) τ = 57 days.

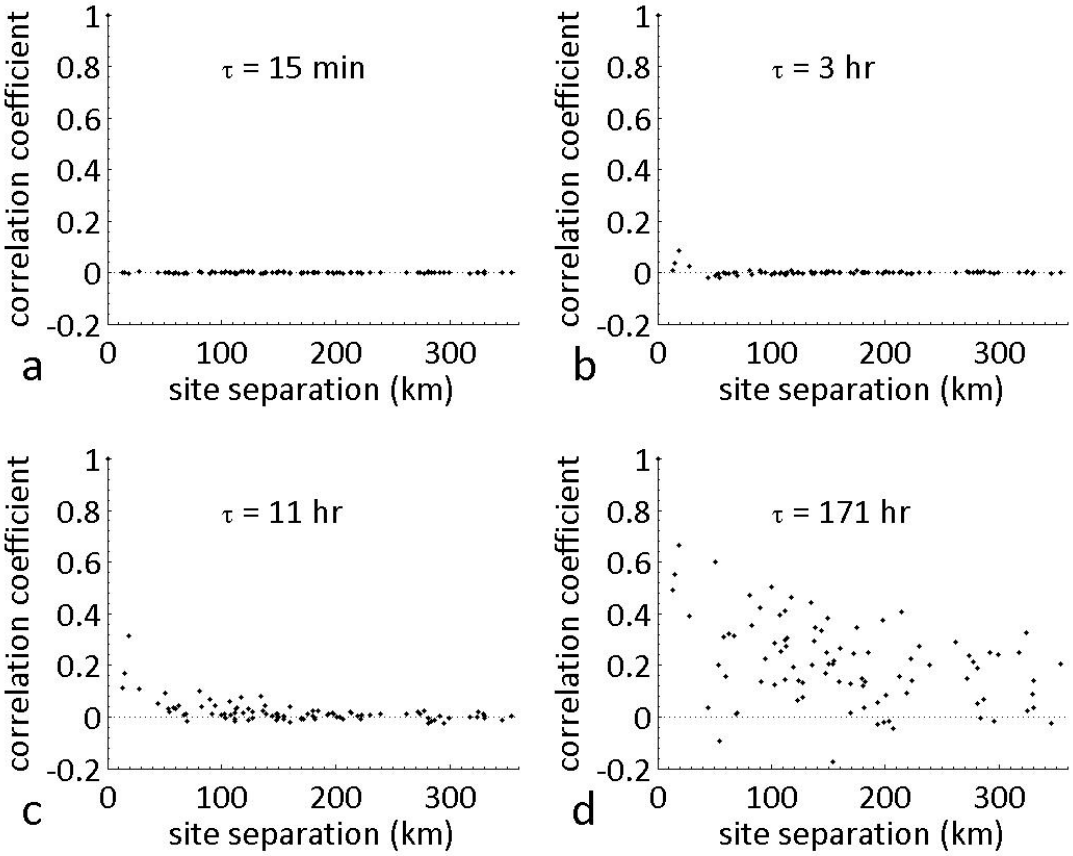

Figure S6: Correlation vs site separation for 14 BPA stations. Five-minute data 2012–2014: (a) High-pass window width τ = 15 minutes; (b) τ = 3 hours; (c) τ = 11 hours; (d) τ = 171 hours.

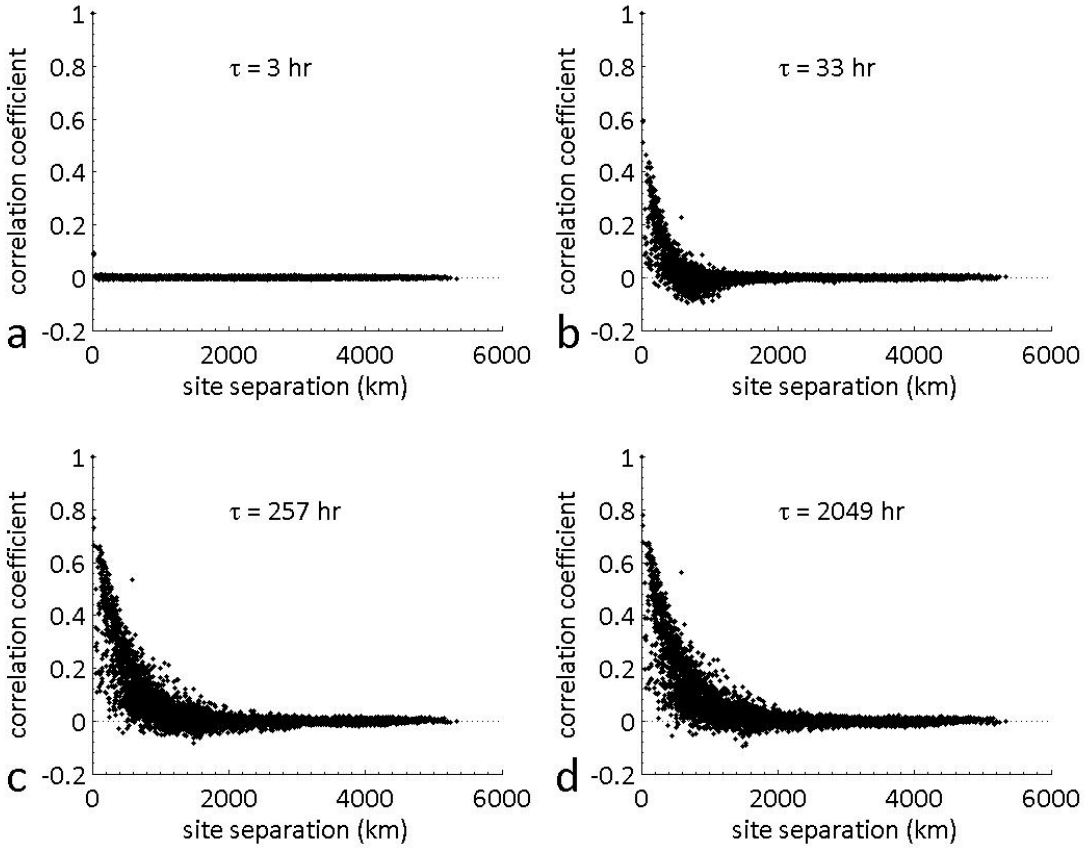

Figure S7: Correlation vs site separation for all 117 CAN stations, hourly surface data 1962–2006: (a) High-pass window width τ = 3 hours; (b) τ = 33 hours; c) τ = 257 hour; d) τ = 2049 hours.

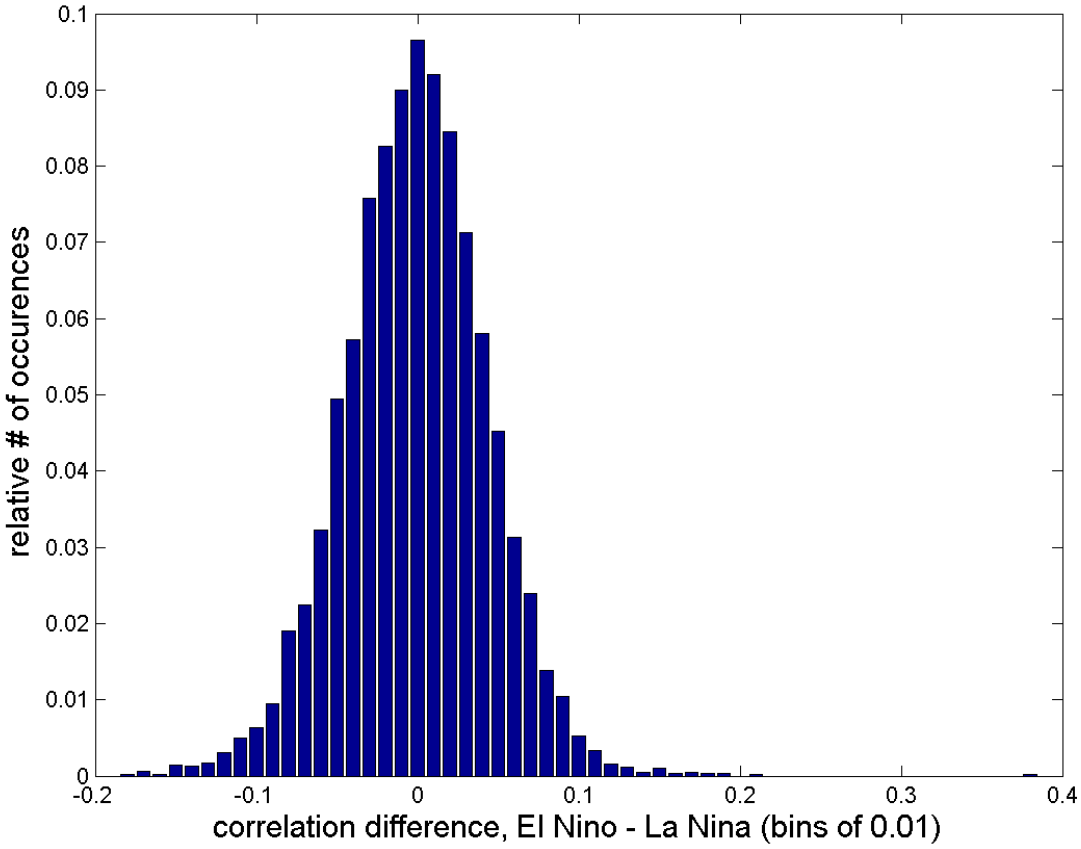

Figure S8: Histogram of correlation coefficient differences between the 1965-1966 El Niño and the 1964-1965 La Niña periods. The mean is -0.0011 and the standard deviation is 0.044.

APPENDIX B

Supplementary Data for:

St. Martin, C. M., Lundquist, J. K., Clifton, A., Poulos, G. S., and Schreck, S. J.: Wind turbine power production and annual energy production depend on atmospheric stability and turbulence, Wind Energ. Sci., 1, 221-236, doi:10.5194/wes-1-221-2016, 2016.

S1 Lidar variability

Lidar measurements of wind speed and direction exhibit larger variability than those from the met tower. This variability may be due to the lidar's operating assumption of homogeneity across the measurement volume: the WINDCUBE v1 measures volumetric-averaged wind speeds and directions over a 20 m thick layer with an effective diameter on the order of the height of the measurement (30° beam angle) and assumes homogeneous flow within that layer. This assumption may not be reliable at this site: observations from scanning lidar of flow at the U.S. Department of Energy (DOE) National Wind Technology Center (NWTC) at the National Renewable Energy Laboratory (NREL) indicate that flow can be very inhomogeneous (Smalikho et al., 2013; Aitken et al., 2014).

Despite this potential for variability at the NWTC, the lidar and tower measurements are generally well-correlated ($R = 0.96$ and bias of 0.37 m s^{-1}, with the lidar recording higher values than the anemometer for this time period; Fig. 8). Note that the bias is likely significantly influenced by the accuracies of the instrument compared (see Sect. 2.2.1 and Sect. 2.2.2). Previous work by Smith et al. (2006), Sathe et al. (2011) and Sanz Rodrigo et al. (2013) saw strong correlations between lidars and anemometers in flat terrain. Smith et al. (2006) found a correlation coefficient of 0.9843 between a ZephIR lidar and a cup anemometer at 80 m for 10-min wind speed averages for 1 day, Sathe et al. (2011) found correlation coefficients greater than

0.98 between WINDCUBE and ZephIR lidars and sonic anemometers at 100 m for 10-min wind speed averages for 4–5 months, and Sanz Rodrigo et al. (2013) found correlation coefficients greater than 0.99 between WINDCUBE and ZephIR lidars and cup anemometers at 89 m for 10-min wind speed averages for 10 days. Sanz Rodrigo et al. (2013) also performed lidar–tower comparisons in complex terrain in the Alaiz mountain range in Navarra, Spain, and found correlation coefficients greater than 0.98 between WINDCUBE and ZephIR lidars and cup anemometers at 78 m for 10-min wind speed averages for approximately 5 months. Our correlations between a lidar and an anemometer, based on 2.5 months of collecting wind speed and direction-filtered data in complex terrain in an atmosphere with relatively few aerosols for backscatter, resulted in a relatively high correlation coefficient of 0.96. Our correlation in an inhomogeneous flow is only slightly lower than other correlation coefficients previously found between lidars and towers in flat terrain.

S2 Rotor equivalent wind speed

Quantifying the wind profile across the entire swept rotor area (SRA) has been shown to improve correlations between wind inflow and power output (Wagner et al., 2009). Here, we calculate rotor equivalent wind speeds (REWS) following Wagner et al. (2009):

$$U_{eq} = \left(\sum_i {U_i}^3 \, \frac{A_i}{A_{tot}}\right)^{1/3} , \tag{S1}$$

where i represents the index of the level, *U* is the horizontal wind speed, A_i is the area of the turbine rotor disk of the level with the corresponding data point (the area of the sector defined by chord/arc relative to 360°, minus the area of the triangle), and A_{tot} is the SRA. When calculating the REWS from the lidar profiles, five levels (40, 60, 80,100, 120 m) are available; when calculating the REWS from the tower cup anemometer data, three levels (55, 80, 105 m) are

available, all of which use Thies anemometers. Cup anemometer data available at 38, 87, and 122 m are not used in these REWS calculations for consistency because these are different instruments than those at 55, 80, and 105 m, which were are to calculate the REWS.

Despite the variability in the shear exponent as calculated from the tower measurements (Sect. 3.7), the high correlations between the 80-m wind speeds and REWS shown in Fig. S1 suggest that power curves for 80 m will be very similar to power curves for REWS for this data set. The high turbulence at the NWTC may have prevented the occurrence of larger wind shear across the rotor disk. This might lead to significant differences in REWS from 80-m wind speeds, which may manifest in the power curves at other sites. Differences between the REWS and the wind speed at hub height at other sites may also affect annual energy production calculations as in Scheurich et al. (2016).

S3 Yaw error and veer

Additionally, we explore the effects of yaw error and wind veer and distributions of these variables as shown in Fig. S2. To calculate yaw error, we subtract the wind direction as measured by the met tower near hub-height from the nacelle position as given by the supervisory control and data acquisition (SCADA) system. The resulting yaw error, however, is centered around 90° instead of 0°, which means the orientation of the turbine position is around 90° off of North. To correct for this, we assume that the yaw error should be 0° at rated power, so we take the average yaw error when the turbine was producing rated power (94.22°) and subtract this from the yaw error to get the correct values of yaw error. After correcting for the turbine yaw orientation offset, we determined that it is not appropriate to split the yaw error distribution into regimes as 78% of the data lie within ± 5° yaw error and 96% of the data lie within ± 10° yaw error.

We found no impact of yaw error or wind veer on the power curves at this site. However, based on other locations (Vanderwende and Lundquist, 2012; Rhodes and Lundquist, 2013; Walton et al., 2014) where significant veer does occur, it may affect power production, but this site does not regularly experience that phenomena.

S4 Power curves for different TKE regimes

Likely due to a lack of sonic data at 74 m that passes our data quality control filters as discussed in Sect. 3.1 (60 %), few statistically-distinct bins emerge from the TKE power curves. Fig. S3 shows the nacelle and upwind tower power curves segregated by TKE regime. Only at about 12 m s^{-1} do statistically-significant differences in power curves emerge between the low and high TKE power curves: at 12 m s^{-1}, cases within the low TKE regime produce significantly more power than cases within the high TKE regime.

Supplementary Data References

Aitken, M.L., Lundquist, J.K., Pichugina, Y.L., and Banta, R.M.: Quantifying wind turbine wake characteristics from scanning remote sensor data, J. Atmos. Ocean. Tech. 31, 765–787, doi:10.1175/JTECH-D-13-00104.1, 2014.

Rhodes, M.E., and Lundquist, J.K.: The effect of wind turbine wakes on summertime US Midwest atmospheric wind profiles as observed with ground-based Doppler LIDAR, Boundary-Layer Meteorol., 149, 85–103, doi:10.1007/s10546-013-9834-x, 2013.

Sanz Rodrigo, J., Borbón Guillén, F., Gómez Arranz, P., Courtney, M.S., Wagner, R., and Dupont, E.: Multi-site testing and evaluation of remote sensing instruments for wind energy applications, Renewable Energy, 53, 200–210, 2013.

Sathe, A., Mann, J., Gottschall, J., and Courtney, M.S.: Can wind LIDARs measure turbulence?, J. Atmos. Ocean. Tech., 28, 857–868, doi:10.1175/JTECH-D-10-05004.1, 2011.

Scheurich F, Enevoldsen, P. B., Paulsen, H. N., Dickow, K. K., Fiedel, M., Loeven, A., and Antoniou, I.: Improving the accuracy of wind turbine power curve validation by the rotor equivalent wind speed concept, Journal of Physics: Conference Series, 753, 1-7, doi: 10.1088/1742-6596/753/7/072029,2016.

Smalikho, I.N., Banakh, V.A, Pichugina, Y.L., Brewer, W.A., Banta, R.M., Lundquist, J.K., and Kelley, N.D.: LIDAR investigation of atmosphere effect on a wind turbine wake, J. Atmos. Ocean. Tech., 30, 2554–2570, 2013.

Smith, D.A., Harris, M., Coffey, A., Mikkelsen, T., Jørgensen, H.E., and Mann, J.: Wind LIDAR evaluation at the Danish Wind Test Site in Høvsøre, Wind Energy, 9, 87–93, doi:10.1002/we.193, 2006.

Vanderwende, B., and Lundquist, J.K.: The modification of wind turbine performance by statistically distinct atmospheric regimes, Environ. Res. Lett., 7, 1–7, doi:10.1088/1748-9326/7/3/034035, 2012.

Wagner, R., Antoniou, I., Pedersen, S., Courtney, M., and Jorgensen, H.: The influence of the wind speed profile on wind turbine performance measurements, Wind Energy, 12, 348–362, doi:10.1002/we.297, 2009.

Walton, R.A., Takle, E.S., and Gallus Jr., W.A.: Characteristics of 50–200-m winds and temperatures derived from an Iowa tall-tower network, J. Appl. Meteor. Clim., 53, 2387–2393, doi:10.1175/JAMC-D-13-0340.1, 2014.

Supplementary Figures

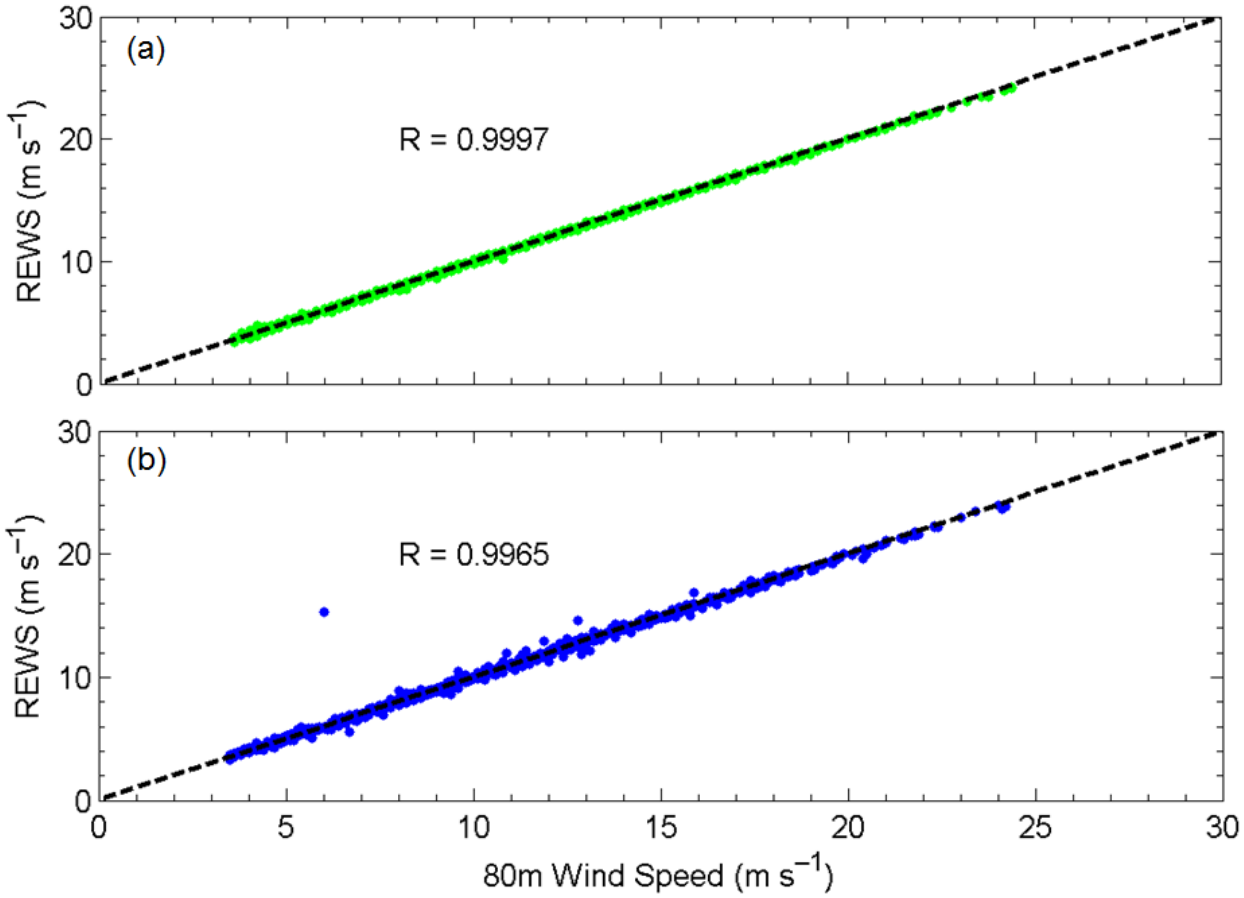

Figure S1. REWS as a function of 80-m wind speed from (a) the tower and from (b) lidar. Black dotted line represents a 1:1 relationship. Includes data filtered for tower 80-m wind speeds between 3.5 and 25.0 m s^{-1}, 87-m wind directions between 235° and 315°, and for normal turbine operation.

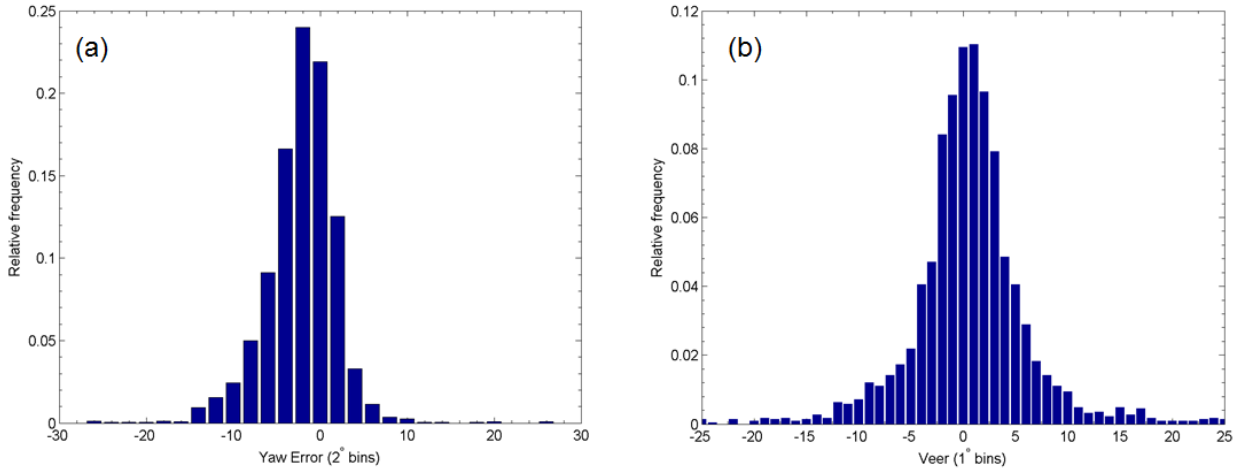

Figure S2. (a) Yaw error histogram and (b) wind veer histogram. Includes data filtered for tower 80-m wind speeds between 3.5 and 25.0 m s^{-1}, 87-m wind directions between 235° and 315°, and for normal turbine operation.

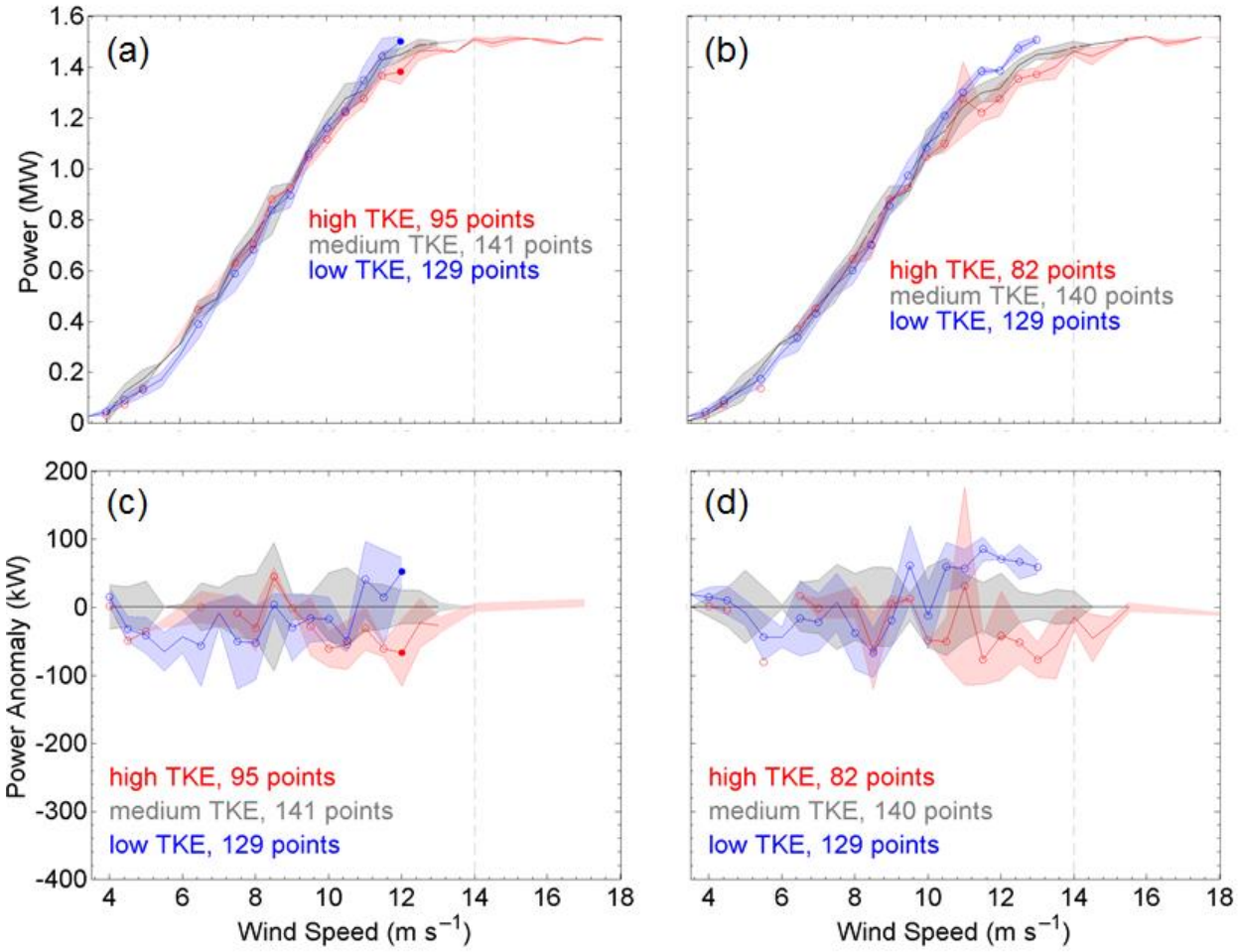

Figure S3. (a) Nacelle anemometer and (b) 80-m tower anemometer power curves with TKE regimes. (c) Naclle anemometer and (d) 80-m tower anemometer power curves shown as the anomaly from the neutral or medium power curve of the TI regimes. Median statistics are used to avoid outlier effects. Statistically distinct differences within each wind speed bin between the regimes are determined by the Wilcoxon rank sum test with a 1 % significance level and denoted by closed circles. Includes data filtered for tower 80-m wind speeds between 3.5 and 25.0 m s^{-1}, 87-m wind directions between 235° and 315°, and for normal turbine operation. Envelopes represent ± 1 MAD for each wind speed bin. The grey dashed line marks rated speed.